MULTI-SCALE MODELING OF DYNAMIC RECRYSTALLIZATION IN METALS UNDERGOING THERMO-MECHANICAL PROCESSING

by

Pooja Nitin Shah

A Thesis

Submitted to the Faculty of Purdue University

In Partial Fulfillment of the Requirements for the degree of

Master of Science in Mechanical Engineering

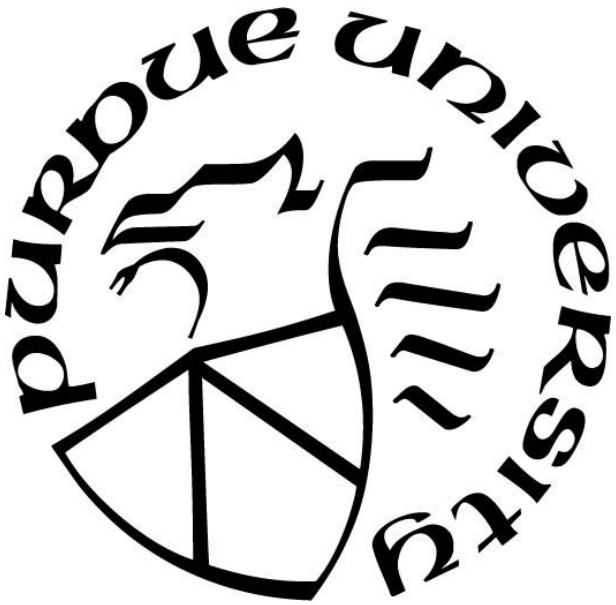

School of Mechanical Engineering

West Lafayette, Indiana

December 2017

THE PURDUE UNIVERSITY GRADUATE SCHOOL
STATEMENT OF COMMITTEE APPROVAL

Dr. Yung C. Shin, Chair
Department of Mechanical Engineering
Dr. Marcial Gonzalez
Department of Mechanical Engineering
Dr. David R. Johnson
Department of Materials Engineering

Approved by:
Dr. Jay P. Gore
Head of the Graduate Program

Dedicated to my family

ACKNOWLEDGMENTS

I express my sincere gratitude to my academic advisor Dr. Yung C. Shin for his unparalleled guidance and mentorship throughout the course of my study at Purdue. Dr. Shin has constantly inspired and motivated me to work to the best of my abilities. I am grateful to him for introducing me to the field of material process modeling and entrusting me with state of the art equipment and facilities.

I thank Dr. Yung C. Shin, Dr. Marcial Gonzalez and Dr. David R. Johnson for serving on my advisory committee and sparing invaluable time reviewing my work.

I also thank Dr. Tao Sun for his assistance and guidance on the experimental work performed in the Synchrotron facility at the Argonne National Laboratory.

I thank my lab mates, colleagues and friends who supported me and made my stay at Purdue memorable.

I am very grateful to my father, Nitin, mother, Nita and sister, Kshama for their unwavering support and love.

TABLE OF CONTENTS

LIST OF TABLES vii
LIST OF FIGURES viii
ABSTRACT xiii
1. INTRODUCTION 16
1.1 Rationale 16
1.2 Literature Review 20
1.2.1 Microstructure based deformation modeling 20
1.2.2 Dynamic recrystallization modeling 25
1.2.2.1 Grain refinement mechanism 26
1.2.2.2 Discontinuous dynamic recrystallization mechanism 29
1.2.3 Experimental measurement of dynamic microstructure evolution 32
1.2.4 Microstructure evolution in friction stir processing 33
1.3 Research Objectives 34
1.4 Thesis Outline 35
2. INTEGRATED DYNAMIC RECRYSTALLIZATIOn MODEL DEVELOPMENT 36
2.1 Initial Microstructure 38
2.2 Dislocation Density-Based Constitutive Model 39
2.3 Critical Dislocation Density 41
2.4 Recrystallization Kinetics 43
2.4.1 Grain refinement kinetics 43
2.4.1.1 Cellular automata formulation 44
2.4.2 Discontinuous dynamic recrystallization kinetics 44
2.4.2.1 Nucleation 45
2.4.2.2 Grain growth 45
2.4.2.3 Cellular automata formulation 46
2.5 Model Implementation 48
3. DYNAMIC RECRYSTALLIZATION STUDY OF PURE COPPER 50
3.1 Grain Evolution in the Quasi-Static Regime 50

3.1.1 Multi-pass compression test 50
3.1.2 Hot compression 55
3.1.2.1 Temperature dependent recrystallization 56
3.1.2.2 Initial microstructure dependent recrystallization 58
3.2 Grain Evolution in the High Strain Rate Regime 59
3.2.1 Experimental procedure 59
3.2.2 Experimental results 61
3.2.2.1 Dynamic grain refinement 61
3.2.2.2 Dynamic grain coarsening 63
3.2.3 Modeling results 64
3.3 Temporal Evolution of Dynamic Grain Refinement 66
3.3.1 Experimental setup 66
3.3.2 Experimental results 71
3.3.2.1 X-ray diffraction analysis 74
3.3.2.2 Grain size evolution 79
3.3.3 Modeling results 84
4. DYNAMIC RECRYSTALLIZATION IN Al 6061-T6 ALLOY DURING FRICTION STIR SPOT WELDING 88
4.1 Experimental Procedure 88
4.2 Results and Discussion 90
4.2.1 Macroscopic results 90
4.2.2 Microstructure evolution results 95
5. CONCLUSIONS AND RECOMMENDATIONS 101
5.1 Conclusions 101
5.2 Recommendations 103
LIST OF REFERENCES 105
VITA 120

LIST OF TABLES

Table 2-1: Dislocation-density model parameters of Copper [19]. 41
Table 2-2: Recrystallization parameters for copper [81, 87]. 46
Table 2-3: Material properties of OFHC Copper [105]. 49
Table 3-1: Dynamic response and microstructure evolution of copper with three initial grain sizes. 62
Table 3-2: Dynamic microstructural evolution results following the heat treatment tests. 64
Table 3-3: Comparison of the experimental and predicted dynamic grain refinement for copper loaded at 2700 s^{-1}..... 65
Table 3-4: Comparison of the experimental and predicted grain coarsening phenomenon of the dynamically loaded copper samples. 66
Table 4-1: Material properties of Al 6061-T6 [19]..... 92
Table 4-2: Recrystallization parameters for Al 6061-T6 [124]. 92
Table 4-3: Dislocation-density model parameters of Al 6061-T6 [19]. 92

LIST OF FIGURES

Figure 1-1: Schematic representation of flow curves during deformation with respect to varying temperatures and operating microstructural phenomena [55]..... 26
Figure 1-2: Schematic of grain refinement mechanism under severe plastic deformation [6]..... 29
Figure 1-3: Cellular automata based grain size evolution prediction of the discontinuous dynamic recrystallization mechanism in copper undergoing hot deformation [87]..... 32
Figure 2-1: Flowchart of the integrated multiscale probabilistic cellular automata based recrystallization model. 37
Figure 2-2: Evolution of the critical dislocation density parameter for pure copper at a constant deformation rate of 0.002 s^{-1} and misorientation angle of 45º for varying temperatures..... 43
Figure 2-3: Modified Von Neumann neighborhood rule representing a hexagonal scheme. 48
Figure 3-1: Comparison of the experimental [100] stress-cumulative strain curves and the predicted curve for copper undergoing multi-pass compression. 51
Figure 3-2: Initial microstructure shown with the orientation variable (Euler angle, Φ1) of the grains mapped onto the cellular automata-finite element mesh with an initial average grain size of 60 μm. 52
Figure 3-3: Comparison of the predicted dislocation density kinetics with the experimental reports [100] for copper undergoing multi-pass compression at room temperature in terms of the (a) dislocation cell size, d and (b) average sub-grain misorientation, θsub at intermediate strains. 53
Figure 3-4: Comparison of the grain boundary distortion and grain structure evolution developed in the FE-CA framework with the experimental reports [100] of copper under large strain deformation at room temperature. 55

Figure 3-5: Comparison of the experimental [107] and predicted final grain structure of copper samples undergoing hot compression at 0.002 s^{-1} and varying operating temperatures. 56
Figure 3-6: Evolution of the recrystallization kinetics for the 775 K case. SDV_N_REC is the recrystallization variable and SDV_PHI is the orientation variable. 57
Figure 3-7: (a) Initial microstructure of grain size 11 μm mapped onto the FE-CA mesh in terms of the orientation variable (b) Initial and final grain size distribution of copper workpiece undergoing hot compression at 0.002 s^{-1} and 775 K. 58
Figure 3-8: Testing section of Kolsky bar [92]. 60
Figure 3-9: (a) Measured raw strain signal (b) Calculated strain rate signal (Equation (17)) during the dynamic loading of copper at a constant rate of 2700 s^{-1}. 61
Figure 3-10: Stress-strain response of Copper deformed at a strain rate of 2700 s^{-1} with varying initial grain sizes of 30 μm, 55 μm and 174 μm. 62
Figure 3-11: (a) Initial micrograph of copper with an average grain size of 55 μm (600°C (1 hr)) (b) Final micrograph with an average grain size of 5.7 μm upon dynamic loading at room temperature. 63
Figure 3-12: (a) Optical micrograph after heat treatment (600°C (1hr)) with a final average grain size of 62 μm (b) Optical micrograph after heat treatment (850°C (1hr)) with a final average grain size of 85 μm. 64
Figure 3-13: Initial mesh of the copper workpiece subjected to dynamic tensile loading at a constant strain rate of 2700 s^{-1} for the 55 μm case. SDV_PHI1 corresponds to the Euler angle (Φ) of the initial orientation and SDV_MISOR corresponds to the calculated grain boundary misorientation. 65

Figure 3-14: (a) Schematic of integrated Kolsky bar apparatus and the 32-ID-B high-speed X-ray beamline at APS [94] (b) Photographs of the setup in the beamline hutch marked (1) High-speed camera used for PCI (2) ICCD camera used to record the diffraction pattern (3) Kolsky tension bar and (c) (4) copper sample setup and (5) Load cell. 68
Figure 3-15: Comparison of the calculated raw energy spectrum and the spectrum with absorption effects with an undulator gap of 11 mm. 69
Figure 3-16: (a) Diffraction geometry of the experimental setup where the area detector is placed at an offset angle from the incident beam direction. The calculated (b) scattering vector q map and (c) azimuthal angle φ map when the detector angle is 15.4° and the X-ray energy is 23.66 keV.. 70
Figure 3-17: (a) Detected raw strain signal where εI is the incident strain and εR is the reflected strain (b) Calculated strain rate signal (Equation (1)) during the dynamic loading of copper showing a constant rate of 1200 s^{-1}..... 72
Figure 3-18: Stress-strain response of copper deformed at a strain rate of 1200 s^{-1}. The curve is demarcated with symbols at points where the phase contrast images and diffraction patterns were recorded. 73
Figure 3-19: Sequence of phase contrast images and diffraction patterns captured during the dynamic deformation of copper..... 73
Figure 3-20: (a) Simulated diffraction peak positions for the first harmonic energy on the cyan bands and second harmonic energy on the yellow bands. Experimental diffraction patterns before and after 200 μs of loading overlaid with (b) first harmonic peak indexing and (c) second harmonic peak indexing. 76
Figure 3-21: (a) One dimensional intensity profiles of the static and fracture diffraction frames (b) Williamson-Hall plots of the series of captured diffraction frames during the high strain rate loading of the specimen at the observed peaks (Frame 4 corresponds to the loading frame further referenced in Figure 3-22). 78

Figure 3-22: One dimensional intensity profiles of the recorded patterns for the chosen diffraction peaks (a) Cu (200) and (b) Cu (111) with respect to the azimuthal angles. It should be noted that a couple of static frames (Frame 1- Frame 3) are taken prior to the loading of the specimen which begins from Frame 4. 79
Figure 3-23: Initial microstructure of the copper sample before loading with an initial average grain size of 36 μm. 80
Figure 3-24: Optical micrographs of the copper sample on fracture with a final average grain size of 6.3 μm. 80
Figure 3-25: Initial and final grain size distribution of a copper sample dynamically loaded at a strain rate of 1200 s^{-1}. 81
Figure 3-26: (a) Time evolution of the normalized peak broadening factor demarcated with the recorded loading strains during the dynamic loading of copper (b) Time evolution of the grain refinement mechanism calculated from the rate of change of the recorded peak broadening during the dynamic loading of copper. 83
Figure 3-27: Grain size evolution during the dynamic loading of copper at a strain rate of 1200 s^{-1}. 83
Figure 3-28: Initial mesh of the copper workpiece subjected to dynamic tensile loading at a constant strain rate of 1200 s^{-1}. SDV_PHI1 corresponds to the Euler angle (Φ) of the assigned orientation of the grain. It has been utilized to depict the microstructure. 84
Figure 3-29: Comparison of the predicted time evolution kinetics of the grain refinement mechanism with the experimental results during the high strain rate loading of copper. 86
Figure 3-30: Predicted simulation contours of the multiscale model of Copper undergoing high strain rate tensile loading. PEEQ corresponds to the strain, SDV_N_REC corresponds to the recrystallization switching variable activated by the cellular automata framework and SDV_PHI corresponds to the grain orientation variable in terms of the Euler angle (Φ)..... 87

Figure 4-1: Experimental Setup of FSSW on Al 60601-T6 plates. 89
Figure 4-2: Mesh and Assembly of the developed FE model for FSSW of Al 6061-T6 plates. 91
Figure 4-3: Axial forces (Experimental and results predicted by the FE model) for the 1500 rpm case. 93
Figure 4-4: Spot chosen in the FE model in front of tool to record temperature for the 1500 rpm case. 94
Figure 4-5: Temperature evolution (Experimental and results predicted by the FE model) for the 1500 rpm case. 94
Figure 4-6: (a) Deformed region predicted by the FE model post plunge in process using the equivalent plastic strain distribution results.(b) Experimental sample after the plunge in process for the 1500 rpm case. 95
Figure 4-7: Initial microstructure of the base metal Al 6061-T6 alloy with an average grain size of 35 μm. 96
Figure 4-8: Microstructure characterization of the stir zone with a final average grain size of (a) 2.7 μm for a rotational speed of 1500 rpm and (b) 3.5 μm for a rotational speed of 2500 rpm. 96
Figure 4-9: Coupled FE-CA mesh of the Al 6061-T6 workpiece with an initial average grain size of 35 μm undergoing FSSW. SDV_PHI corresponds to the orientation of the grain in terms of its Euler angle, Φ. 97
Figure 4-10: Optical micrographs for the grain size characterization of the friction stir weld for the 2500 rpm case. 98
Figure 4-11: Comparison of experimental and predicted average grain sizes of the stir zone for the (a) 1500 rpm rotational speed and (b) 2500 rpm rotational speed. 99

ABSTRACT

Author: Nitin Shah, Pooja. MSME
Institution: Purdue University
Degree Received: December 2017
Title: Multi-Scale Modeling of Dynamic Recrystallization in Metals undergoing Thermo-Mechanical Processing
Major Professor: Yung C. Shin

This study focuses on devising a unified multi-scale numerical framework to predict the grain size evolution by dynamic recrystallization in metals and alloys for an array of severe plastic thermo-mechanical deformation conditions. The model is developed to predict the temporal and spatial grain size evolution of the material subjected to high strain rate and temperature dependent deformation.

Dynamic recrystallization evolves by either a continuous grain refinement mechanism around room temperatures or by a discontinuous grain nucleation and growth mechanism at elevated temperatures. The multi-scale model bridges a dislocation density-based constitutive framework with microscale physics-based recrystallization laws to predict both the types of recrystallization phenomena simultaneously. The simulations are conducted within an integrated probabilistic cellular automata-finite element framework to capture the physics of the recrystallization mechanisms.

High strain rate loading experiments in conjunction with microstructural characterization tests are conducted for pure copper to characterize the dynamic grain size evolution in the material and evaluated against the model predictions. Synchrotron X-rays are integrated with a modified Kolsky tension bar to conduct *in situ* temporal characterization of the grain refinement mechanism operating during the dynamic deformation of copper and evaluated against the developed model kinetics.

Finally, the model is implemented to predict the grain size evolution developed during the friction stir spot welding of Al 6061-T6 for varying tool rotational speeds. The experiments show that the original microstructure is completely replaced by a recrystallized fine-grained microstructure with the final average grain size and morphology dependent on the process parameters. The model accurately predicts the process temperature rise with increasing tool rotational speeds, which results in a higher rate of grain coarsening during the dynamic recrystallization phenomenon.

1. INTRODUCTION

1.1 Rationale

The demand for micro and nano-scale manufacturing processes has aggressively grown due to the increasing need of highly sophisticated devices with complex structures in conjunction with decreasing component sizes [1]. High precision machining and forming processes are now an integral part of industrial manufacturing. These processes involve nonhomogeneous plastic flow along with severely localized stresses and severe plastic deformation, dependent on the internal microstructure of the material [2]. In such manufacturing processes, the correlation between the process parameters and resulting microstructure has become an important issue to the product and process development. Predictive modeling of microstructure evolution in the nano- and micro-scale manufacturing processes would aid the identification of an optimized set of parameters to produce products with desirable properties [3, 4].

A material's properties are not based solely on its chemical composition but also by multitudinous details of its hierarchical three-dimensional internal structure. The structure spans a wide range of length scales each of which plays a pivotal role in the material's performance. Most metals are characterized by a polycrystalline internal structure. At the microscale, the materials microstructure is typically defined by the spatial distribution of its grain structure, grain size and crystalline orientation and by measures of defect densities such as dislocation density, porosity, microcrack density etc. at lower nanometer length scales. The above-mentioned parameters determine the materials strength, ductility and thermo-mechanical behavior [5]. Grain size is regarded as the microstructural parameter affecting nearly all aspects of the physical and mechanical behavior of

polycrystalline metals as well as their chemical and biochemical response [6]. Most of the above-mentioned properties benefit from the grain size reduction process.

The process of controlling material properties and its corresponding microstructure evolution during thermo-mechanical processing has been extensively researched. One of the prevailing methods involved grain recrystallization and refinement due to plastic deformation around room temperatures followed by annealing at elevated temperatures. Another method of producing new grains by the dynamic recrystallization process was by the direct hot working of metals. The recrystallization process is characterized by nucleation of new grains followed by their growth at elevated temperatures [7, 8]. The study of the recrystallization phenomenon in various steady state deformation processes has provided a number of insights into the evolution and strength mechanisms due to grain size evolution in metals and alloys.

Recently, some metal forming and machining processes involving severe plastic deformation (SPD) have gained a lot of popularity as a novel grain formation process. In these processes, large plastic strains are imposed on a bulk solid to bring about grain size reduction and refinement due to dynamic recrystallization [9, 10]. These processes produce ultrafine-grained metals with high strength properties [11, 12]. However, the mechanisms causing grain refinement under large strain and high strain-rate deformation have not been comprehensively evaluated. The limiting factor associated with these methods is that though microstructural data in terms of grain size changes are obtained, the corresponding flow stress behavior of the material is not available at high strain rates. Developing experimental techniques to characterize the recrystallization mechanisms and

modeling techniques to predict the corresponding material behavior under the aforementioned dynamic deformation conditions would further aid their process design.

Significant advances in the fields of optical and electron microscopy have allowed for the quantitative description of the microstructure at various length scales. This in turn has led to an exponential advance in the theoretical and fundamental understanding of the material microstructure evolution. As the quality of data increases, the opportunity to develop useful analysis tools also increases [13]. With the development of the orientation imaging microscopy technique (OIM), the ability to characterize the salient features of a polycrystalline material has steadily increased [14]. The imaging techniques have been manipulated in a wide variety of combinations to characterize different aspects of the microstructures for analysis [15]. The microstructure analysis ranges from simple determination of parameters such as grain size to the full evaluation of failure mechanisms. Furthermore, the imaging techniques have been used as a tool to study the relationship between various microstructure parameters controlling the deformation mechanisms [16]. Advances in this field drive the motivation to accurately model and validate the microstructure evolution process of complex deformation processes.

A number of experimental and modeling studies have been carried out to characterize the relationship between the material behavior and the corresponding manufacturing process parameters. The modelling approaches have predominantly involved finite element methods (FEM) and molecular dynamics (MD) analysis. MD simulations have been successfully applied to study nanometric cutting [17]; however, the method is not suitable for analyzing large scale processes due to prohibitive computational requirements. On the other hand, continuum-based modeling techniques

such as FEM utilize constitutive models that are largely phenomenological in nature at the macroscopic length scale.

The material undergoes several metallurgical transformations at the microscopic length scale due to localized thermo-mechanical processing conditions during machining and cannot be captured by empirical constitutive models [18]. Metal forming and manufacturing processes like hot rolling, forging, friction stir processing, laser-assisted machining etc. are characterized by severe plastic deformation in conjunction with elevated temperature conditions. The microstructure evolution at these conditions typically result in either grain refinement or grain coarsening due to the dynamic recrystallization phenomenon. In order to include predictability at the microscopic length scale and evaluate the resultant microstructures obtained from such machining processes, Ding and Shin implemented micro-scale physics laws within the finite element model [19, 20, 21]. This methodology successfully predicted the microstructure evolution in terms of the grain refinement of various materials undergoing manufacturing processes like orthogonal cutting, laser shock peening and multi-pass cold rolling. These studies drive the motivation to develop a finite element based predictive model of the grain size evolution occurring in dynamic deformation processes involving high operating strain rates and temperature conditions. However, the studies were limited to deformation processes operating around ambient temperatures.

1.2 Literature Review

1.2.1 Microstructure based deformation modeling

Over the years, many efforts have been made to incorporate material characteristics into the predictive simulation of plastic deformation processes. In the early efforts, empirical models developed by Johnson and Cook [22], Zerilli and Armstrong [23] and Follansbee and Kocks [24] were developed for various materials and used to predict the material behavior. Dixit et al. [25] provided a comparison of the various material modeling techniques utilized to model an array of manufacturing processes. The study reviewed the developed material models from simple empirical models to the microstructure-based models. Determination of the model material parameters through experimentation at high strain-rate and temperature conditions is identified as the most challenging aspect of developing a microstructure-based constitutive model.

One of the early approaches towards microstructure-based constitutive modeling for polycrystalline metals was the crystal plasticity theory. The theory correlated the macroscopic continuum material behavior with its microscopic single crystal deformation [26, 27, 28, 29]. The theory accounted for the inherent anisotropic nature of polycrystalline deformation by simulating the individual crystal deformation due to slip. The developed model was rate dependent and did not account for polycrystal interactions. The crystallographic slip theory was advanced to account for rate dependent deformation and texture evolution applicable to large strain deformation [30]. A model that accounted for the deformation rate of each crystal based on its neighboring crystals was developed in [31] to implement the effect of crystal interactions within the crystal plasticity theory. However, these approaches were developed for simple internal and external boundary conditions and not designed to be implemented with a finite element framework. To

simulate complex boundary conditions and deformation simulations, finite element approximations are coupled with the crystal plasticity theory in the crystal plasticity finite-element (CPFE) method [32]. It is based on a multi-scale physics-based internal variable formulation and integrated into commercial FE solvers with user-defined subroutines. The advantage of this method lies in its computational efficiency to simulate engineering problems with complex boundary conditions along with accounting for the micro-scale physics. It has found applications in simulating the anisotropic deformation and texture evolution for an array of mechanical problems like nanoindentation, micro-bending and deep drawing [33, 34, 35]. It was successfully implemented for microscopic scale processes; however, in order to simulate large scale problems like metal forming, tool design and machining processes, homogenization had to be used [36].

Crystal plastic deformation occurs by the motion of defect densities such as dislocations at the nanometer length scale. The movement of dislocations on preferred slip planes results in the previously mentioned crystallographic slip at microscale. Nes [37] proposed an elastic-plastic work hardening theory based on the formation of a dislocation substructure within crystals upon deformation. The evolution of the dislocation substructure is further characterized by the storage and evolution of its constituents namely dislocation cell size, dislocation density and sub-boundary misorientation. The model introduced statistical evolution laws for the storage of dislocations within a dislocation cell network in the form of an internal state variable approach to predict the flow stress behavior of the material. However, the dislocation density evolution laws were based on the empirical Kocks-Mecking formulation [24]. The pioneering work by Estrin et al. [38, 39] advanced the dislocation-density based

strain-hardening formulation to large strain deformation problems. The study presented a unified microphysics-based constitutive model built on the operating dislocation mechanisms that account for microstructural phenomena like dynamic recrystallization and dynamic recovery. The stage IV of the work hardening curve was related to the forming of disorientations and had not been considered in the previous formulations. A model that accounts for the stochastic accumulation of disorientations, its effect on the dislocation density evolution and the flow stress curve of aluminum is shown in [40]. The physics-based nature of the model allows for a straight-forward calibration of material parameters and was implemented within the commercial FE solver to simulate the material hardening behavior for large strain deformations. It was successfully implemented to simulate the dislocation density evolution and misorientation evolution in pure copper under equal channel angular pressing by Enikeev et al. [41].

The review by Grong and Shercliff [42] showed that the internal state variable methodology was a robust framework to predict the microstructural evolution and recrystallization of metals under a range of nonisothermal mechanical processes. Nes and Marthinsen [43] developed a dislocation density-based internal state variable approach which accounted for the microstructural variables of stacking fault energy, grain size, solid solution content and particle size. It was utilized to predict the work hardening of FCC metals and alloys during plastic deformation from ambient to high temperature conditions. Though the internal state variable approach provided a unified computationally robust methodology to predict the microstructure evolution of metals undergoing large strain thermo-mechanical processing, the evolution laws implemented by the Nes and Marthinsen [43] were largely phenomenological with the material

parameters calibrated for steady state deformation. Micro-physics based constitutive laws are more desirable for high strain rate and temperature processes.

Ma et al. [44] introduced a micro-physics based constitutive framework coupling dislocation density dynamics at the nanoscale with a crystal plasticity formulation at the microscale implemented within a finite element framework. The methodology was improved to simulate the interactions between the grain boundaries and dislocations, thereby evaluating the grain boundary geometry effect on deformation [45, 46]. The model was calibrated and simulated for small-scale problems such as simple shear of aluminum single and bi crystals with improved predictions over the crystal plasticity models. Aayogi et al. [47] developed a similar framework of coupling dislocation density and patterning dynamics with the crystal plasticity to successfully simulate the grain refinement mechanism occurring during large-strain compression. The model uniquely combines the finite-element and finite-difference frameworks as a numerical solution solely in FEM would require an extremely fine mesh of submicron size. The physics-based multi-scale approach of coupling dislocation dynamics and the crystal plasticity framework has shown to successfully simulate the microstructural mechanics in terms of the grain boundary and recrystallization kinetics. However, it is limited in application to small-scale problems with simple boundary conditions as modeling large-scale processes with nanometer sized mesh elements is computationally prohibitive.

A number of varied numerical formulations have been developed and evaluated to integrate the microstructural evolution in the predictive modeling of large-scale metal processing involving complex internal and external boundary conditions. Svoboda et al. [48] adopted a dislocation density based plasticity model developed by Lindgren et al.

[49] to simulate the orthogonal cutting of 316L stainless steel alloy. The model is based on dislocation glide mechanism in which the flow stress is based on the resistance to the dislocation motion due to long range (athermal) and short range (thermal) barriers. Sun et al. [50] adopted an internal state variable formulation based on a dislocation density based constitutive model to predict the dynamic recrystallization during the hot isothermal processing of titanium alloy. The dislocation density evolution laws implemented in the studies mentioned above were based on the phenomenological Kocks-Mecking [24] model requiring calibration for varying strain rate and temperature regimes. Experimental calibration to identify microstructure-based material properties is not easily available for high strain rate processes like machining.

An alternative scheme accounting for the microstructure with probabilistic descriptors and implemented in the finite element method using correlation functions has been developed [51, 52]. It accounted for the critical problem faced during microstructure modeling; the finite element approach is deterministic while the microstructure evolution laws are stochastic in nature. It has shown to improve the texture and grain size predictions while reducing computational costs, but requires the development of a variable Lagrangian finite element formulation. Another approach to the crystal plasticity modeling accounting for the stochastic response of the material at small length scales along with the grain size and crystal orientation effects was developed by Askari et al. [53]. It coupled the Monte Carlo method with dislocation dynamics to predict the material properties of polycrystalline copper undergoing nanoindentation. Though the above-mentioned probabilistic formulation is computationally superior, it cannot be

readily implemented within commercial FE solvers, which in turn limits its implementation to small strain deformation problems without severe mesh distortions.

The recent development in the analytical modeling techniques to predict the material behavior in terms of microstructure evolution has allowed for the replacement of the phenomenological models with physics based models for various manufacturing processes. The probabilistic microstructure based multi-scale models are restricted by the domain size, implementation within complex FEM models and computational efficiency. In order to effectively model the microstructural evolution of large scale deformation processes, it is imperative to identify the operating microstructural evolution mechanism affecting the material's physical behavior and correspondingly develop a physics-based predictive model.

1.2.2 Dynamic recrystallization modeling

Severe plastic deformation (SPD) processes such as machining and metal forming involve several microstructural transformations. Among the various microstructural parameters, grain size is considered crucial as it largely impacts the physical and mechanical behavior of polycrystalline metals [54]. The effects of the processing conditions and microstructural evolutions on the flow curve of metals is shown in Figure 1-1. The review conducted by Sakai et al. [6] identified dynamic recrystallization as the metallurgical process that controls the grain size evolution during a thermo-mechanical deformation process. The study detailed the dynamic recrystallization mechanism with experimental and numerical approaches. The dynamic recrystallization phenomenon occurs either by a continuous recovery process evolved by the segregation of grains at relatively low temperatures or by a discontinuous process evolved by the nucleation and

growth of new grains at elevated temperatures. The former continuous recovery process is referred to as either continuous dynamic recrystallization (cDRX) or grain refinement and is a one step process introduced by deformation around room temperature. The latter mentioned discontinuous dynamic recrystallization (dDRX) is a two-step process typically occurring during high temperature plastic deformation. It involves nucleation of recrystallized grains followed by their growth brought about by migration of grain boundaries at elevated temperatures.

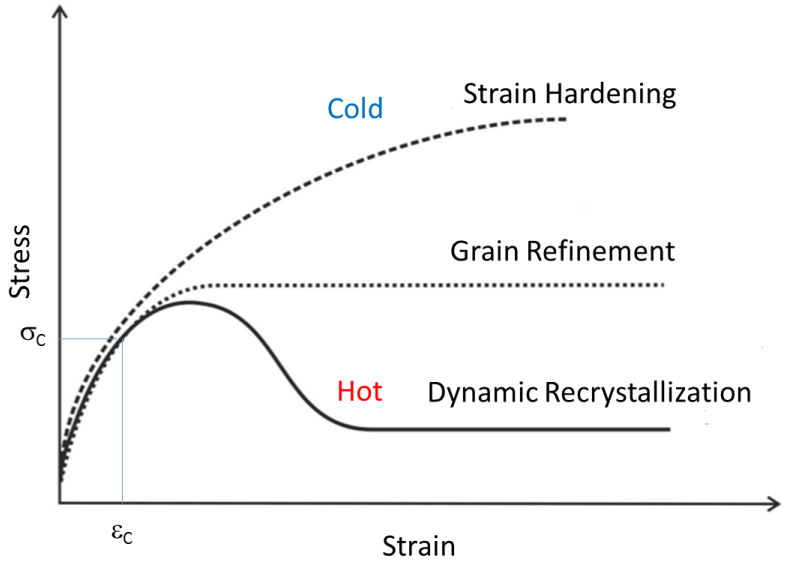

Figure 1-1: Schematic representation of flow curves during deformation with respect to varying temperatures and operating microstructural phenomena [55].

1.2.2.1 Grain refinement mechanism

Grain refinement is a one-step recrystallization process that occurs during plastic working around room temperatures (~T<0.5Tm, where Tm is the melting temperature of the material). The phenomenon produces ultrafine grained microstructures with favorable strength properties. During the plastic straining of metals and alloys, initially, high

dislocation densities are introduced to form low-energy dislocation structures or cells. Upon further straining, dislocation cells form cell blocks by annihilation of dislocations through cross-slip, climb and arrangement in low-angle (2–5º) sub-grain boundaries [56]. These boundary misorientations continue to increase with straining due to variation in the strain state across the boundaries [57]. These strain-induced boundaries are referred to as geometrically-necessary boundaries while the former mentioned low-angle boundaries are formed by statistically stored dislocations. Several studies show that plastic straining results in the transformation of the low-angle boundaries (LAB) into high-angle boundaries (HAB) (Misorientation angle is greater than 15º for HAB) resulting in subdivision of the original grains into recrystallized fine grains characterized by high misorientation boundaries [58, 59]. The refinement mechanism is strain and temperature dependent; the grain size decreases with increasing strain and decreasing temperature with a tendency to saturate at large strains.

The early model to simulate the large strain hardening behavior due to grain refinement along with the dislocation cell size evolution was modeled based on the dislocation density evolution in [60]. Estrin et al. [38] developed a constitutive model that predicts the strain hardening behavior of crystalline materials at large strains. The model simulates the dislocation substructures as composite structures made up of dislocation walls and interiors with corresponding evolution laws for the dislocation densities. It is a two-dimensional formulation based on the physical mechanisms operating at the dislocation scale. Tóth et al. [61] extended it to a general three-dimensional formulation and incorporated it into polycrystalline plasticity models to predict strain-hardening effects. The model was further developed to account for the influence of grain boundaries

and crystallographic orientations and simulate the microstructural parameters of grain size, misorientation and texture evolution during severe plastic deformation [62].

Equal channel angular pressing (ECAP) is a popular metal processing method to produce ultrafine grained materials with enhanced properties [63]. Several studies carried out on severe plastic deformation report that the ultra-fine grains observed at large strains are formed by replacing the dislocation cell networks developed at lower strains [64, 65, 66] as shown in Figure 1-2. The dislocation density progressively increases during deformation which leads to the transformation of the dislocation cells into recrystallized fine grains. This is taken into account by Baik et al. [67, 68] who adopted the dislocation density-based constitutive model by Tóth et al [61] to successfully model the grain refinement mechanism in equal channel angular processing (ECAP) of IF steel and aluminum respectively. Lemiale et al. [69] showed the model's compatibility under high strain rate impact conditions. Ding and Shin [19, 20, 21] adopted the dislocation density material model to successfully predict the grain refinement in metals undergoing complex deformation processes like orthogonal cutting, cold rolling and laser shock peening for a range of metals and alloys. The above-mentioned modeling techniques operate on the assumption that the dislocation cell size at large strains represent the grain size upon refinement. Though this approach successfully predicted the final grain size obtained upon large strain thermo-mechanical processing, it does not capture the previously discussed physics of the mechanism where the initial new grains are predominantly formed in the vicinities of pre-existing grain boundaries and propagate upon further straining. Furthermore, the model is applicable to deformation processes with large strain deformation at room temperature processing conditions and not at elevated temperatures.

It does not account for the physics of the previously mentioned discontinuous dynamic recrystallization mechanism characterized by grain nucleation and growth operating at elevated temperatures.

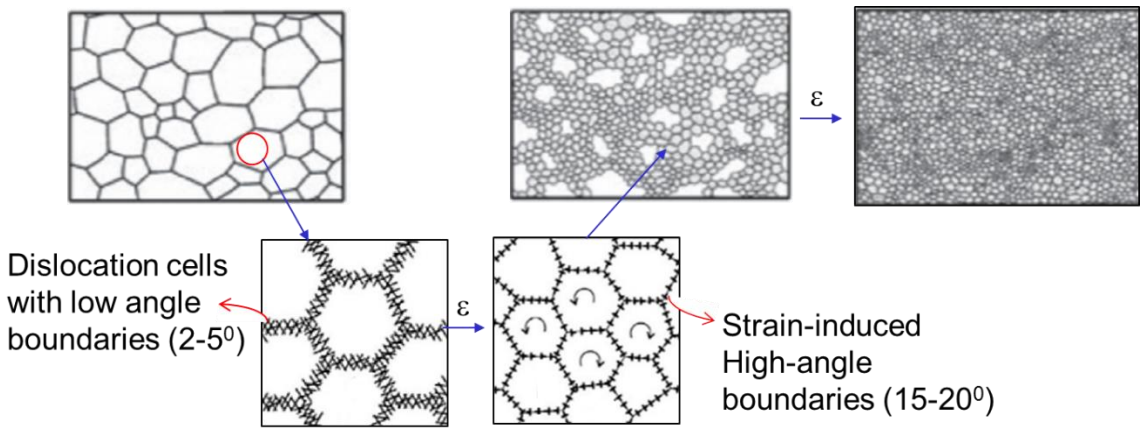

Figure 1-2: Schematic of grain refinement mechanism under severe plastic deformation [6].

1.2.2.2 Discontinuous dynamic recrystallization mechanism

Discontinuous dynamic recrystallization (dDRX) is a two-step process typically occurring during high temperature plastic deformation. It involves nucleation of recrystallized grains followed by their growth brought about by migration of grain boundaries at elevated temperatures. Microstructure-based experimental and modeling studies were conducted to evaluate the relationship between the operating deformation conditions and structural behavior in metals [70]. The flow stress curve due to the dDRX mechanism has a reducing work hardening rate till a maximum flow stress is reached beyond which strain softening is prevalent [71]. The flow curves show changes in shape from multi peak to single peak due to the decreasing rate of recrystallization. The extent of recrystallization is directly affected by operating parameters such as temperature,

strain rate and initial grain size [72]. The changes in shape are dependent on the rate of grain nucleation and coarsening occurring in the material based on the processing conditions.

The mechanism of dDRX is caused by the accumulation of dislocations with competing mechanisms of dislocation generation causing work hardening and annihilation causing work softening. The onset of the phenomenon occurs once a critical dislocation density is accumulated in the deforming metal [73, 74]. The nucleation model for dDRX was developed based on the energy differences and misorientation accumulation [75]. The nucleation mechanism during the dDRX process was experimentally characterized by studying the effect of grain boundary on the deformation of copper bicrystals, and was identified by grain boundary bulging and serrations during straining, which indicate the nucleation sites [76, 77]. During straining of polycrystals, local gradients of dislocation density and orientation develop typically near the pre-existing grain boundaries. This in turn results in nucleation of recrystallized grains which are identified by bulging of the original grain boundaries [78]. Nucleation is followed by subsequent grain growth caused by the migration of boundaries at elevated temperatures [6].

The preliminary models to simulate microstructural evolution during dDRX was developed based on the Monte Carlo method which utilized simplified nucleation rate and energy relations [79, 80]. However, the models did not utilize realistic hot deformation parameters and did not account for grain growth kinetics due to the limitations of the method. The cellular automata (CA) method became a popular tool in material science to model the discontinuous dynamic recrystallization phenomenon. Ding

and Guo [81] coupled the cellular automaton method with recrystallization kinetics to simulate the grain nucleation and growth in pure copper under quasi-static hot working as shown in Figure 1-3. The developed multi-scale framework inherently linked the continuum behavior of the material with its corresponding microstructural properties of dislocation density and grain boundary kinetics. The methodology was extended to predict the dynamic recrystallization in β phase during processing of Ti-6Al-4V alloy [82]. Over the years, similar approaches have been adopted to simulate and investigate the effect of discontinuous dynamic recrystallization in various metals and alloys like rotor steel [83], Ti-6Al-4V alloy [84], near-α titanium alloy [85], and NiTi shape memory alloy [86]. Hallberg et al. [87] developed a probabilistic cellular automata method to simulate the grain size and shape changes during the hot compression of copper. The study was further extended to a three-dimensional formulation to inculcate the effect of particle impurities on the extent of recrystallization [88]. Popova et al. [89] introduced a probabilistic cellular automata method based on a hexagonal neighboring scheme to improve recrystallized grain shape and size simulations for magnesium alloys. However, all the studies mentioned above utilized the phenomenological Kocks-Mecking (KM) model [24] to predict the dislocation density evolution, which was in turn used to predict the grain boundary kinetics during deformation. Consequently, it would require calibration of the material parameters for varying strain conditions ranging from the quasi-static to dynamic regimes.

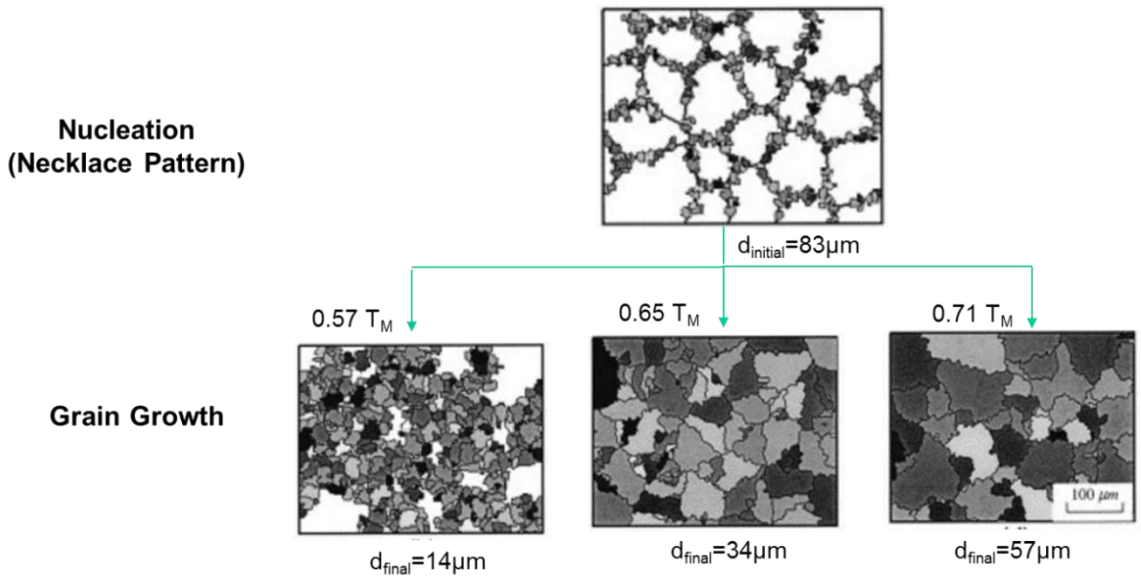

Figure 1-3: Cellular automata based grain size evolution prediction of the discontinuous dynamic recrystallization mechanism in copper undergoing hot deformation [87].

1.2.3 Experimental measurement of dynamic microstructure evolution

One of the major challenges faced during the study of high strain rate severe plastic deformation processes such as equal channel angular pressing (ECAP) [64], high pressure torsion (HPT) [90], and accumulative roll bonding (ARB) [91] is that though experimental data regarding the microstructural changes and recrystallization mechanisms have been widely obtained, there is very limited data available for the flow stress behavior of the materials undergoing these processes. Consequently, the mechanism of dynamic recrystallization with respect to the initiation and rate of evolution is not known for these dynamic deformation processes. The Kolsky bar or Split Hopkinson bar is a commonly used tool to characterize the dynamic flow stress behavior of materials [92]. Recently, the Kolsky bar was integrated with the high-speed X-ray imaging capabilities of Synchrotron radiation to track the damage initiation and evolution of a dynamically deforming specimen. This novel data acquisition technique allowed for

in situ analysis of the damage and failure modes of a number of materials developed during dynamic loading experiments [93]. This experimental technique allows for *in situ* correlation between the flow stress behavior and the corresponding microstructural evolution in terms of the sample texture and phase change for dynamically loaded nitinol and aluminum [94].

1.2.4 Microstructure evolution in friction stir processing

Friction stir welding (FSW) is one of the most widely used welding techniques for joining lightweight materials. This technique was developed by TWI [95] in 1991 and has found applications in similar and dissimilar welding of aluminum, magnesium, titanium and steel alloys. A new variant of this process was developed where only the plunging operation of FSW is performed to weld the plates. This variant is called friction stir spot welding (FSSW) and has shown promise in replacing single-point joining processes like resistance spot welding and riveting. The FSSW process consists of three stages: plunging, stirring and retracting. During the plunging phase, the rotating tool plunges into the workpieces until it reaches the predetermined depth followed by the stirring action. In the stirring stage, the tool keeps rotating in the workpieces. Frictional heat produced during the plunging and stirring stages heats up, softens and mixes the plasticized material adjacent to the tool to form a solid-state joint. After the stirring stage, the tool is retracted from the workpieces.

The deformation occurring during such manufacturing processes involves a combination of varying strains, strain rates and temperatures. Consequently, the corresponding grain size evolution would include both the grain refinement and discontinuous dynamic recrystallization mechanisms depending on the processing

condition. The FSSW process was characterized by the dynamic recrystallization phenomenon at the microstructural scale where the original microstructure was replaced by a recrystallized fine-grained structure [96]. Several reports indicate an increase in average grain size in the stir zone with increasing rotational speed for Al-alloy and Mg-alloy friction stir welds [97, 98, 99]. These studies evaluated the influence of the tool rotational speed, operating temperature and strain rate on the extent of dynamic recrystallization and grain size evolution in the stir zone. Furthermore in the studies, phenomenological models have been developed to correlate the grain size evolution to the processing parameters. The phenomenological nature of the model does not capture the physics of the recrystallization process and requires calibration of material constants at varying operating parameters.

1.3 Research Objectives

The primary objective of this study is to predict the microstructure evolution in metals and alloys undergoing dynamic thermo-mechanical processing in deformation processes like machining and metal forming. The aim is to develop a unified microstructure-based constitutive material model to be implemented within a large scale process simulation for an array of thermo-mechanical deformation processing conditions ranging from quasi-static to dynamic regimes with varying low to high temperatures. A multi-scale approach is considered with micro-physics based evolution laws to predict the material behavior and grain size evolution due to dynamic recrystallization during the deformation. The specific objectives are as follows:

1. Develop a methodology capable of predicting the material microstructure evolution at multiple length scales and their relationship under thermo-mechanical processing.

2. Validation and benchmarking of the model kinetics in the quasi-static regime with experimental reports in literature.
3. Develop an experimental procedure to characterize the dynamic grain refinement with the Kolksy bar and grain coarsening phenomena with heat treatment tests followed by comparison with the model predictions.
4. Develop an experimental procedure to characterize the temporal evolution of the dynamic grain refinement phenomenon with Synchrotron X-rays followed by the evaluation of predicted model kinetics.
5. Evaluate the application of the model to a manufacturing process by predicting the dynamic recrystallization in a friction stir spot welding process for varying process parameters and comparison against experimental results.

1.4 Thesis Outline

In Chapter 2, the novel multi-scale cellular automata based dynamic recrystallization model is proposed. In Chapter 3, the model kinetics are evaluated for copper for an array of thermo-mechanical deformation processes ranging from quasi-static to dynamic in conjunction with low to high temperature conditions. In Chapter 4, the model is applied to predict the dynamic recrystallization of Al 6061-T6 under friction stir spot welding for varying process parameters and compared with the experimental results. In Chapter 5, conclusions and recommendations for future work are given.

2. INTEGRATED DYNAMIC RECRYSTALLIZATION MODEL DEVELOPMENT

In this chapter, the multi-scale numerical framework to predict dynamic recrystallization is proposed. The model operates on a multi-scale framework divided into the microscale (intra-granular) and the mesoscale (inter-granular). At the microscale, dislocation density dynamics is predicted within the grains, and at the mesoscale, recrystallization laws are implemented to predict the dynamic recrystallization and grain boundary kinetics. A cellular automata framework is coupled with the finite element scheme to track the grain size evolution. A flowchart of the overall model is shown in Figure 2-1.

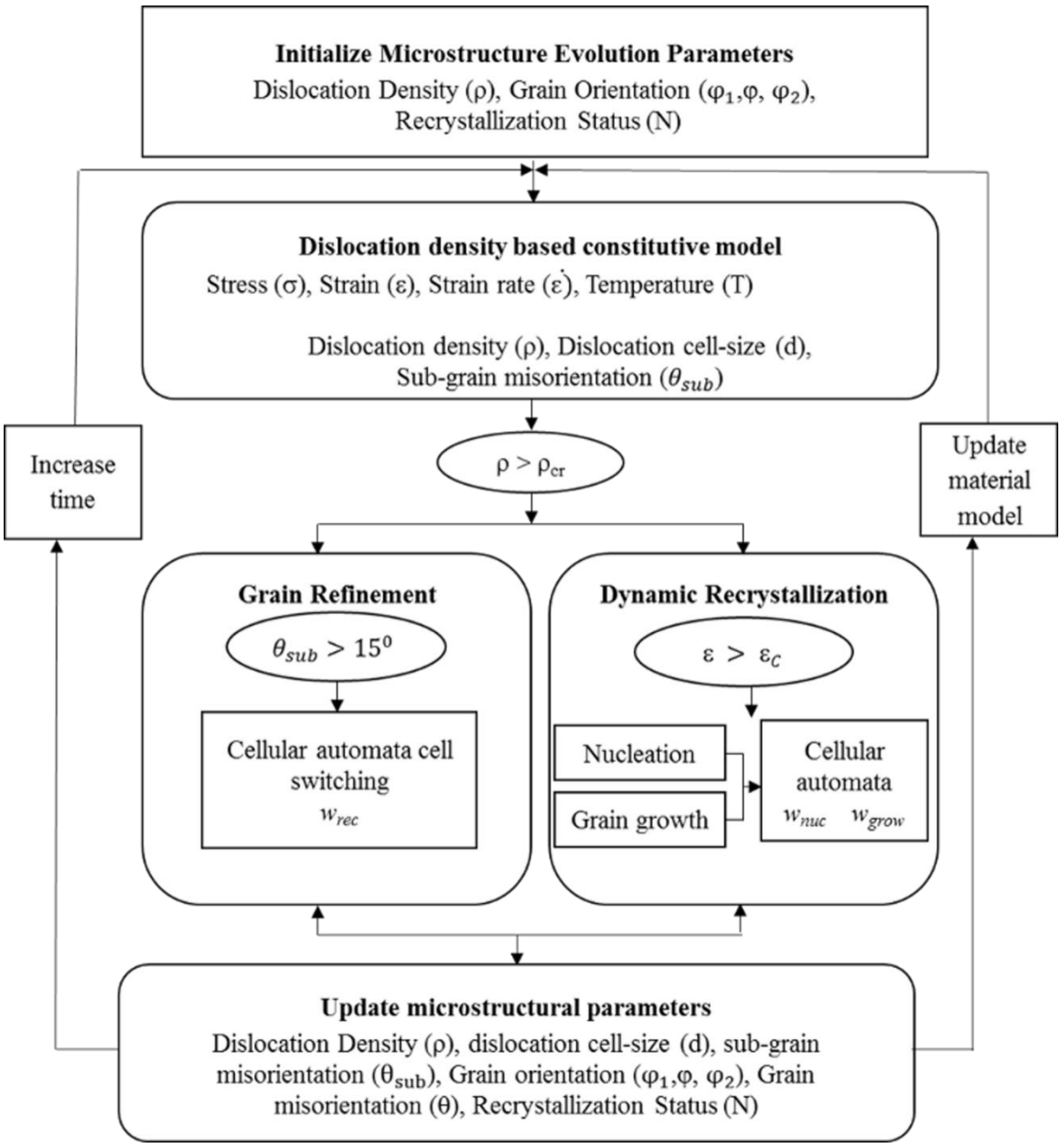

Figure 2-1: Flowchart of the integrated multiscale probabilistic cellular automata based recrystallization model.

2.1 Initial Microstructure

The internal microstructure variables utilized to track the grain size evolution are dislocation density (ρ), dislocation cell size/sub-grain size (d) and (iii) sub-grain misorientation (θ_{sub}) at the intra-granular scale; grain size (r), grain boundary misorientation (θ) and (vi) recrystallization state (N) at the inter-granular scale. The study focuses on the grain size evolution developed due to dynamic recrystallization without texture and reorientation evolution. The grains are represented by the Euler angle formulation based on a random distribution. This orientation variable is solely utilized to track the grain size and grain boundary evolution in the deforming matrix and the corresponding grain boundary misorientation is calculated based on the rotation matrix of the assigned Euler angles.

The initial intra-granular parameters such as dislocation density, cell size, and sub-grain misorientation are assumed to be uniform for all the grains prior to deformation. At the intergranular scale, the initial grain size distribution is obtained from experimental microstructural characterization tests and mapped onto the finite element mesh with a cellular automata framework. The cellular automata cells coincide with the finite elements in this model and hold the microstructural information at each integration point. The initial microstructure mapping and evolution laws of the internal state variables are discussed in the following sections.

2.2 Dislocation Density-Based Constitutive Model

At the intra-granular scale, the dislocation density-based constitutive material model developed by Tóth et al. [61] is implemented to predict the dislocation density evolution within the grains during deformation. In the model, a dislocation cell structure forms during deformation. The cell structure is made up of dislocation cell walls and cell interiors populated with the corresponding dislocation density parameters namely, cell interior dislocation density (ρ_c) and the cell wall dislocation density (ρ_w). The cell wall dislocation density is further divided into statistical dislocation density (ρ_{ws}), and geometrically necessary dislocation density (ρ_{wg}). The evolution laws of the dislocation densities are governed by a set of differential equations as follows:

$$\dot{\rho}_c = \alpha^* \frac{1}{\sqrt{3}b}\sqrt{\rho_w}\dot{\gamma}_w^r - \beta^* \frac{6}{bd(1-f)^{\frac{1}{3}}}\dot{\gamma}_c^r - k_0\left(\frac{\dot{\gamma}_c^r}{\dot{\gamma}_o}\right)^{-1/n}\rho_c\dot{\gamma}_c^r \tag{1}$$

$$\dot{\rho}_{ws} = \alpha^* \frac{\sqrt{3}(1-f)}{fb}\sqrt{\rho_{ws}+\rho_{wg}}\dot{\gamma}_w^r + \beta^* \frac{6(1-f)^{\frac{2}{3}}}{bdf}\dot{\gamma}_c^r - k_0\left(\frac{\dot{\gamma}_w^r}{\dot{\gamma}_o}\right)^{-1/n}\rho_{ws}\dot{\gamma}_w^r \tag{2}$$

$$\dot{\rho}_{wg} = \xi\beta^* \frac{6(1-f)^{\frac{2}{3}}}{bdf}\dot{\gamma}_c^r \tag{3}$$

In Equations (1) and (2), the terms on the right-hand side of the equation correspond to the dislocation density mechanisms. The first term corresponds to the rate of generation of dislocations; the second term corresponds to the rate of transfer of the cell interior dislocations which move into the walls of the cell structure, and the last term corresponds to the annihilation of the dislocations governed by cross-slip. The terms α^*, β^* and k_0 are constant while *n* is the strain rate sensitivity constant of the annihilation process and is inversely proportional to the temperature. In Equation (3), the geometrically necessary

dislocations are given by the fraction (ξ) of the outgoing cell interior dislocations into the cell walls. b is the Burgers vector, γ is the shear strain and $\dot{\gamma}_c^r = \dot{\gamma}_w^r = \dot{\gamma}$ is the strain rate satisfying the strain compatibility condition.

The total dislocation density is given by a rule of mixtures as follows:

$$\rho_{tot} = f(\rho_{ws} + \rho_{wg}) + (1 - f)\rho_c \quad (4)$$

where *f* denotes the volume fraction of the cell walls, the evolution of which has been reported to decrease monotonically with strain. The dislocation cell size *d*, otherwise referred to as the sub-grain size, is directly related to the total dislocation density.

$$d = K/\sqrt{\rho_{tot}} \quad (5)$$

where *K* is a proportionality constant.

During deformation, the dislocation cells are induced with a misorientation across their cell walls. This sub-grain misorientation build-up directly propagates the grain refinement phenomenon. It depends on the geometrically necessary dislocations (ρ_{wg}) (Equation (3)) as follows:

$$\theta_{sub} = \arctan\left(b\sqrt{\rho_{wg}}\right) \cong b\sqrt{\rho_{wg}} \quad (6)$$

The theoretical nature of the model allows for a simple interpretation of the material parameters [19]. They are developed such that it replicates the constitutive behavior of the material under various strains, strain rates and temperatures and the parameters for copper is shown in Table 2-1. The dislocation density model operates at the intra-granular scale to predict the dislocation density, dislocation cell size and sub-grain misorientation evolution within each grain of the initially mapped microstructure. The predicted

dislocation density and sub-grain misorientation are implemented at the inter-granular scale to predict the recrystallization kinetics.

Table 2-1: Dislocation-density model parameters of Copper [19].

Material	**α^***	**β^***	**k_o**	**A(K)**	**B(K)**	**$\dot{\gamma}_o$**	**f_o**	**f_α**	**K**
Copper (Quasi-Static)	0.04	0.01	9.0-10.2	30000	14900	200	0.25	0.077	10
Copper (Dynamic)	0.04	0.01	12.0-16.1	30000	14900	4000	0.25	0.077	10

Material	**M**	**$\widetilde{\gamma^r}$**	**ρ_{wo} (mm^{-2})**	**ρ_{co} (mm^{-2})**	**b (mm)**	**α**
Copper (Quasi-Static)	3.06	3.2	1e7	1e8	2.56e-7	0.25
Copper (Dynamic)	3.06	3.2	1e7	1e8	2.56e-7	0.25

2.3 Critical Dislocation Density

The recrystallization kinetics implemented at the inter-granular scale accounts for both grain refinement and discontinuous dynamic recrystallization mechanisms separately owing to their contrasting physical mechanisms and operating temperatures. A critical dislocation density parameter is utilized to recognize the onset of either phenomena. It is based on energy changes as derived by Roberts and Ahlblom [74]:

$$\rho_{cr} = \left(\frac{20\gamma\dot{\varepsilon_p}}{3blM\tau^2}\right)^{1/3} \tag{7}$$

where γ is the grain boundary energy, $\tau = 0.5\mu b^2$ is the dislocation line energy, M is the grain boundary mobility and l is the dislocation mean free path. The grain boundary energy and mobility parameters are discussed in the upcoming sections. The dislocation mean free path l is based on the predicted dislocation cell size (Equation (5)) as [81]:

$$\frac{\sigma l}{\mu b} = K_1 \quad (8)$$

where σ is the flow stress and K_1 is 10 for most metals.

The onset of discontinuous dynamic recrystallization is assumed to occur when the predicted total dislocation density (Equation (4)) exceeds the critical dislocation density value, while the grain refinement phenomenon is active below the critical threshold. Based on the above formulation, the evolution of critical dislocation density is plotted for pure copper deformed at a constant strain rate of $0.002s^{-1}$ and misorientation angle of 45° for varying temperatures in Figure 2-2. At lower temperatures ($T<0.5T_m$; T_m is the melting temperature) the value of the critical dislocation density is very high; decreasing rapidly with increasing temperature, implying that the discontinuous dynamic recrystallization is active at these high temperatures ($T<0.5T_m$; T_m is the melting temperature) while grain refinement is active at the lower temperatures. It should be noted that 1.0e9 mm^{-2} is the minimum observed dislocation density of copper deforming at $0.002s^{-1}$ as reported by [100]. The upcoming sections show the successful implementation of this relation to predict the onset and evolution of both types of the recrystallization phenomena.

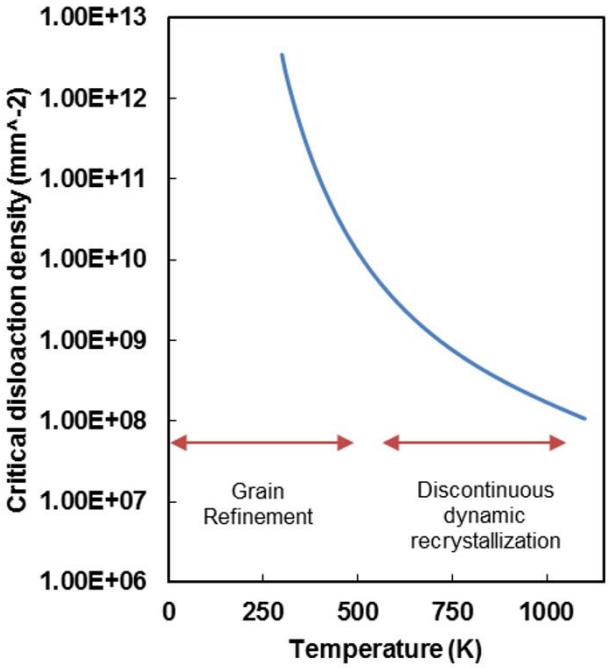

Figure 2-2: Evolution of the critical dislocation density parameter for pure copper at a constant deformation rate of 0.002 s^{-1} and misorientation angle of 45º for varying temperatures.

2.4 Recrystallization Kinetics

At the inter-granular scale, a probabilistic cellular automata framework is coupled with recrystallization kinetics to simulate the grain structure evolution. Depending on the critical dislocation density parameter, either the grain refinement or the discontinuous dynamic recrystallization kinetics are implemented as follows:

2.4.1 Grain refinement kinetics

Grain refinement is a one-step recrystallization process typically developed during large strain deformation around room temperatures. The grain is split internally by the formation of new internal large-angle boundaries due to the accumulation of the sub-grain misorientation (Equation (6)). It is assumed that once the predicted sub-grain misorientation of a dislocation cell exceeds 15º, which is the accepted value for a high

angle boundary (HAB), the dislocation cell or sub-grain is chosen as a possible recrystallization site.

2.4.1.1 Cellular automata formulation

Once the potential recrystallization sites are identified, a probabilistic cell state switching rule is utilized to predict the formation of recrystallized grains. Each identified cell is assigned a random number $\xi \in [0, 1]$ and a switching probability w_{rec}, which is the ratio of the current sub-grain misorientation and the maximum sub-grain misorientation among the recrystallization sites, described by:

$$w_{rec} = \frac{\theta_{sub}}{\theta_{submax}}, \qquad \theta_{sub} < \theta_{submax} \tag{9}$$

If w_{rec} <=ξ , the cell forms a recrystallized grain. The switching variable ***N*** takes the value of 1 from 0 and the cell is assigned a minimum dislocation density value due to recrystallization.

2.4.2 Discontinuous dynamic recrystallization kinetics

Discontinuous dynamic recrystallization is a two-step process developed during deformation at high temperatures. Once the dislocation density of the deforming matrix reaches a critical value (Equation (7)), the kinetics of grain nucleation and subsequent growth are implemented in terms of activation energies and predicted dislocation density evolution as follows:

2.4.2.1 Nucleation

The nucleation rate per unit of grain boundary area is a function of the operating strain rate and temperature based on the model developed by Peczak and Luton [101]:

$$\dot{N}(\dot{\varepsilon}, T) = C\dot{\varepsilon}^{m} exp(-\frac{Q_{act}}{RT}) \quad (10)$$

where *T* is the absolute temperature (K), *R* is the gas constant, Q_{act} is the activation energy for nucleation, *C* is a constant fitting parameter and *m* is set to 1. The constant fitting parameter *C* in this model is calibrated for varying strain rates and temperatures from the Zener Hollomon parameter, $Z = \dot{\varepsilon}\exp(Q_{act}/RT)$ [102]. Once the discontinuous dynamic recrystallization is activated, the change in number of nuclei ΔN is calculated based on the predicted nucleation rate parameter.

2.4.2.2 Grain growth

The driving force for growth of recrystallized grains is based on the local grain boundary mobility *M* and the stored deformation energy *P* reported by Burke and Turnbull [7]:

$$v = MP \quad (11)$$

$$M(T) = \frac{b\delta D_{ob}}{kT} exp\left(\frac{-Q_b}{RT}\right) \quad (12)$$

where δD_{ob} is the coefficient of grain boundary self-diffusion, Q_b is the boundary diffusion activation energy and *k* is the Boltzmann constant. The values of the activation energy (Q_{act}), boundary diffusion activation energy (Q_b) and co-efficient of grain

boundary self-diffusion (δD_{ob}) for copper are available in literature as shown in Table 2-2.

The stored deformation energy (P) is based on the difference between the dislocation densities of the recrystallized cell and matrix as follows:

$$P = \tau\left(\rho_{cell} - \rho_{recrystallized}\right) - \frac{2\gamma}{r} \tag{13}$$

where τ is the dislocation line energy, ρ_{cell} is the dislocation density of the matrix, $\rho_{recrystallized}$ is the dislocation density of the recrystallized cell, γ is the grain boundary energy, and r is the radius of the recrystallized grain. The grain boundary energy γ is dependent on the boundary misorientation as reported by Read and Shockley [103]:

$$\gamma = \begin{cases} \gamma_0 & \theta > 15 \\ \gamma_0 \dfrac{\theta}{\theta_o}\left[1 - ln\dfrac{\theta}{\theta_o}\right] & \theta < 15 \end{cases} \tag{14}$$

where θ is the boundary misorientation. γ_0 is the boundary energy when the boundary becomes a high angle boundary ($\theta_o = 15^0$) shown in Table 2-2.

Table 2-2: Recrystallization parameters for copper [81, 87].

Material	**μ (MN/m^2)**	**Q_{act} (KJ/mol)**	**δD_{ob} (m^3/s)**	**Q_b (KJ/mol)**	**γ_0 (Jm^{-2})**
Copper	4.21e4	261	5.0e-15	104	0.625

2.4.2.3 Cellular automata formulation

Nucleation is not initiated until a critical strain (ε_c) is attained in the grains [81], which is determined from experimental flow stress curves of the material. Once the potential nucleation sites are identified based on the critical dislocation density (ρ_{cr}) and critical strain (ε_c) criteria, the previously mentioned cellular automata cell switching probability rule is applied. The switching parameter w_{nuc} is calculated as follows:

$$w_{nuc} = \frac{\rho_{local}}{\rho_{max}}\ , \qquad \rho_{cr} < \rho_{local} < \rho_{max} \tag{15}$$

where ρ_{cr} is the critical dislocation density, ρ_{local} is the dislocation density of the cell and ρ_{max} is the maximum predicted dislocation density. If w_{nuc} <=ξ , the cell is chosen as a nucleus, variable *N* takes the value of 1 and a minimum dislocation density value.

Growth occurs by consumption of the current cell by a neighboring recrystallized cell. The cells that can undergo growth must not be previously recrystallized and must possess at least one recrystallized neighbor. The neighboring schemes for growth usually considered in CA models are the 4-point von Neumann and 8-point Moore neighbors as shown by Raabe [104]. However, in the current model, a modified von Neumann neighborhood rule is implemented. The modified neighborhood rule represents a hexagonal scheme where among the 8-nearest neighbors considered the corner elements are assigned a 0.48 switching proportionality [89] as shown in Figure 2-3. Hexagonal cellular automata cells allow for better predictions of the recrystallized grain size and shape as the root mean square distance mismatch is smaller than in a square grid. The switching parameter w_{grow} is calculated as the ratio of the local grain boundary velocity to the fastest moving grain boundary in the domain as follows:

$$w_{grow} = \frac{v_{local}}{v_{max}}\ , \qquad v_{local} < v_{max} \tag{16}$$

If w_{grow} <=ξ , the cell is recrystallized, the variable *N* is switched from 0 to 1 and the recrystallized cell assumes the state of the impinging cell. The probabilistic step is considered to avoid situations when two or more elements can potentially consume the same element and the element is consumed by the neighbor with whom it has the highest grain boundary velocity.

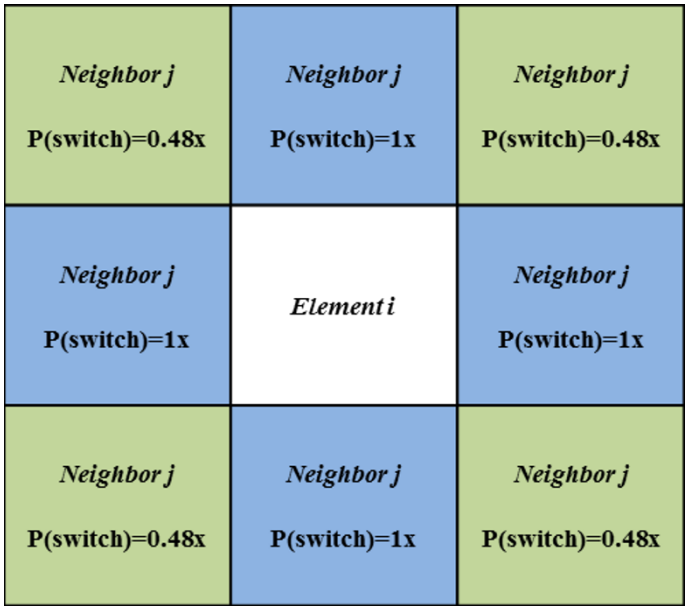

Figure 2-3: Modified Von Neumann neighborhood rule representing a hexagonal scheme.

2.5 Model Implementation

The commercial software Abaqus 6.14 is utilized to simulate quasi-static (Section 3.1) and dynamic deformation (Section 3.2) processes for pure copper at varying temperature conditions. A user-defined subroutine is developed using FORTRAN to implement the recrystallization model kinetics (Figure 2-1). The CA method is implemented with state-dependent variables (SDV's) to allow for a simple one-to-one mapping of the microstructural variables in terms of the grain boundaries, misorientation and size on the FE mesh. The microstructure-based internal variables tracked by the cellular automata cells are stored in state-dependent variables (SDVs) at every integration point of the finite element mesh and updated with every time step.

The physics-based dislocation density constitutive model allows for a simple interpretation of the material parameters valid for an array of deformation conditions

ranging from quasi-static to dynamic as well as low to high temperature deformation conditions. Since a phenomenological model is not implemented, the integration of the constitutive model along with energy based recrystallization kinetics implicitly account for temperature conditions and do not require calibration at varying temperatures. The material parameters for pure copper are shown in Tables 2-1, 2-2 and 2-3.

Table 2-3: Material properties of OFHC Copper [105].

Material	**E (GPa)**	**ν**	**ρ (kg/m^3)**	**T_m (K)**	**Thermal Expansion ($10^{-6}/^0C$)**	**Thermal Conductivity (W/mK)**	**Specific Heat (J/KgK)**
Copper	116	0.34	8960	1356	16.6	400	985

3. DYNAMIC RECRYSTALLIZATION STUDY OF PURE COPPER

In this chapter, the model is implemented to predict thermo-mechanical deformation and microstructure evolution of copper in the quasi-static regime and benchmarked against experimental reports available in literature. To evaluate the model kinetics in the dynamic regime, a set of high strain rate experiments were designed to characterize the dynamic grain size evolution of copper at multiple length scales and simulated with the model to evaluate its kinetics in the dynamic regime. Finally, Synchrotron measurements revealed the temporal evolution of the dynamic grain refinement mechanism in copper.

3.1 Grain Evolution in the Quasi-Static Regime

3.1.1 Multi-pass compression test

Multi-pass compression tests conducted at room temperature is chosen as the benchmark to predict the extent of grain refinement occurring under large strain deformation at room temperature in pure copper. In the study by Belyakov et al. [100], copper samples with an initial average grain size of 60 μm were compressed at a strain rate of 10^{-3} s^{-1} in multiple steps resulting in a fine-grained microstructure of size 0.2 μm. Microstructural characterization was conducted after each step to correlate the extent of grain refinement with the corresponding dislocation density evolution.

The dislocation density constitutive model for copper is implemented to simulate the multi-pass compression test in the 2D coupled temperature-displacement regime with the size of the finite element chosen based on the smallest observed grain size (0.2 μm). Force boundary conditions for compression are enforced with the loading direction changed by 90° between each loading pass and a strain of 0.4 applied at each pass. A

comparison of the experimental and predicted flow curve over 14 compressions is shown in Figure 3-1. The dislocation density constitutive model accurately predicts the dynamic recovery process with strain hardening occurring at low strains below 2 followed by almost zero strain hardening at higher cumulative strains up to 5.6.

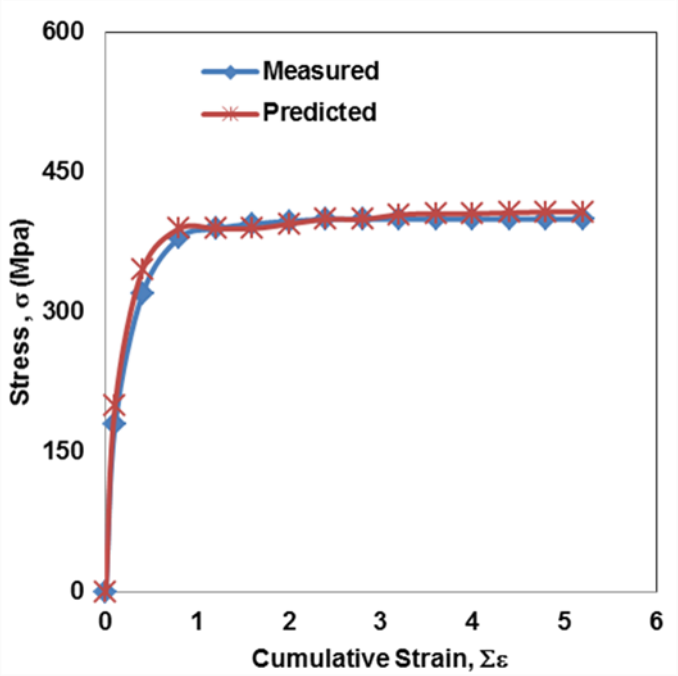

Figure 3-1: Comparison of the experimental [100] stress-cumulative strain curves and the predicted curve for copper undergoing multi-pass compression.

The initial microstructure with an average grain diameter of 60 μm is reconstructed using the open source software Dream 3D [106] and mapped onto the finite element mesh with the state dependent variables as shown in Figure 3-2. As mentioned in Section 2.1, the grains are assigned a random orientation via the Euler angle formulation solely to track the grain size and boundary evolution throughout the deformation process. Based on the critical dislocation density criterion, the grain refinement kinetics are active during this process.

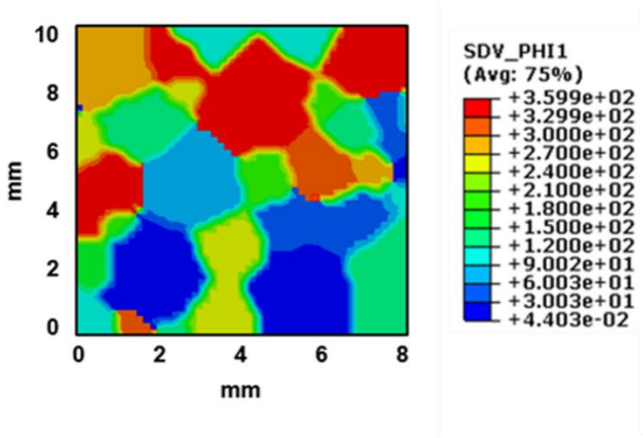

Figure 3-2: Initial microstructure shown with the orientation variable (Euler angle, Φ1) of the grains mapped onto the cellular automata-finite element mesh with an initial average grain size of 60 μm.

At the intra-granular scale, the predicted dislocation density kinetics in terms of the dislocation cell size (Equation (5)) and sub-grain misorientation (Equation (6)) evolution is compared with experimental results reported in the study by Belyakov et al. [100]. In Figure 3-3, the initial stages of straining introduce high dislocation densities due to which the dislocation cell size decreases rapidly to a stable value of 0.2μm, beyond which it remains almost constant. The sub-grain misorientation increases with increasing strain throughout the deformation process. Based on the model, the grain refinement process is activated when the sub-grain misorientation value exceeds 15° corresponding to the plastic strain of 1.6.

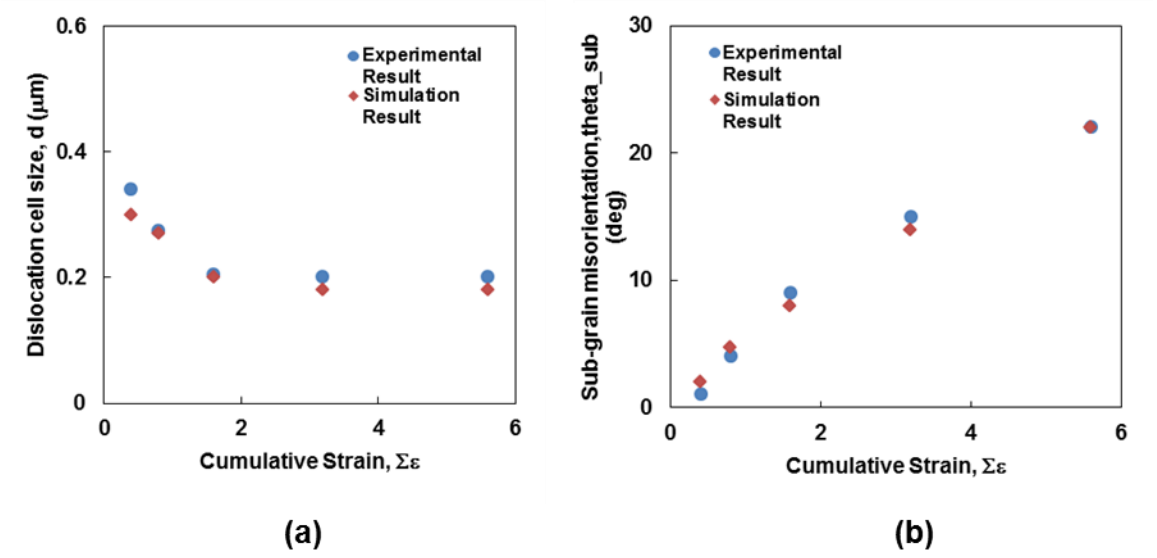

Figure 3-3: Comparison of the predicted dislocation density kinetics with the experimental reports [100] for copper undergoing multi-pass compression at room temperature in terms of the (a) dislocation cell size, d and (b) average sub-grain misorientation, θsub at intermediate strains.

Once the sub-grain misorientation exceeds 15º, which is the accepted value for a high angle boundary (HAB), the corresponding cellular automata cells at the inter-granular scale are chosen as potential recrystallization sites, followed by the implementation of the probability cell state switching rule for refinement (Equation (9)). Figure 3-4 compares the the grain boundary distortion and grain structure evolution developed in the FE-CA framework with the experimental reports. The grain size evolution is driven by the corresponding large strain deformation shown by the stress-strain curve in Figure 3-1.

In Figure 3-4, the first row shows the experimental TEM images at intermediate strains of 0.8, 1.6 and 5.6 where the numbers indicate the boundary misorientation in degrees. The second row shows the orientation angles to track the grain boundary distortion and the third row shows the predicted misorientation angles. At ε=0.8 (Figure

3-4 (a)), it is seen that relatively high misorientations corresponding to high angle boundaries are formed near the pre-existing grain boundaries. Some parts of the initial grain boundaries are bulged and distorted due to development of fine recrystallized grains. The recrystallization sites are characterized by medium to large angle boundaries with high misorientation values ($\theta>15°$). At $\varepsilon=1.6$ (Figure 3-4 (b)), the misorientation buildup continues to increase (Figure 3-3) due to which there is a rapid development of new fine grains near the vicinities of the initial grain boundaries leading into the initial grain interiors. Upon further deformation at $\varepsilon=5.6$ (Figure 3-4(c)), the continued increase in misorientation results in a fine-grained structure with medium to large-angle boundaries with high misorientation values in the TEM images and simulations (SDV_THETA).

The recrystallization model accurately predicts that the copper workpiece with an initial average grain size of 60 μm is refined down to an ultra-fined grain structure with a final average grain size of 0.2 μm when subjected to large strain deformation at room temperature. From the Figures 3-2, 3-2 and 3-4, the probabilistic multi-scale numerical framework successfully predicts the onset and evolution of grain refinement in copper undergoing large strain deformation at room temperature in the quasi-static regime.

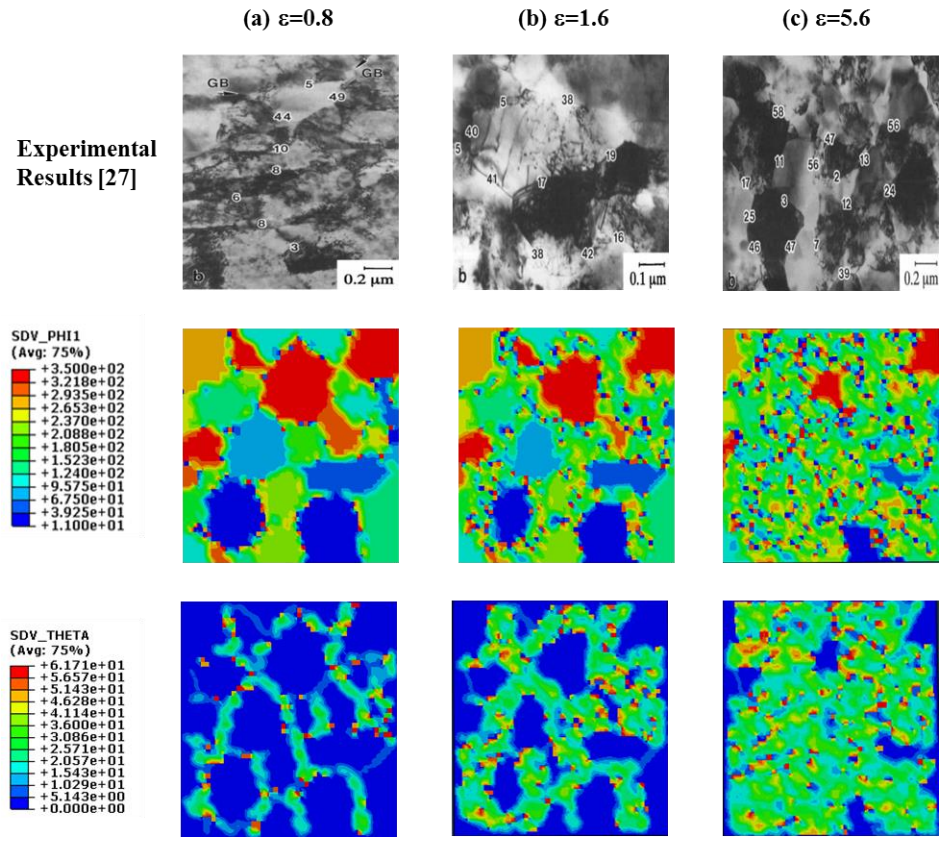

Figure 3-4: Comparison of the grain boundary distortion and grain structure evolution developed in the FE-CA framework with the experimental reports [100] of copper under large strain deformation at room temperature.

3.1.2 Hot compression

Blaz et al. [107] conducted hot compression tests on copper to study the effects of varying temperatures and initial microstructures on the extent of the discontinuous dynamic recrystallization phenomenon. This experiment is simulated to evaluate the implemented discontinuous dynamic recrystallization kinetics. An initial microstructure with an average grain size of 78 μm which conforms with the experiments is mapped to the finite element mesh as done previously.

3.1.2.1 Temperature dependent recrystallization

Blaz et al. [107] conducted hot compression tests of pure copper at 0.002 s^{-1} and varying temperatures. Microstructural characterization tests showed that copper samples with an initial average grain size of 78 µm when compressed at 725K, 775K, 875K, 975K and 1075K resulted in recrystallized structures of grain sizes 9.8 µm, 14 µm, 34 µm, 57 µm and 90 µm respectively. The extent of discontinuous dynamic recrystallization with respect to grain growth is directly dependent on the operating temperature. Figure 3-5 shows a comparison of the experimental and predicted final grain sizes. It is seen that the model kinetics accurately predicts the observed grain nucleation and coarsening phenomenon with a maximum discrepancy of 12%.

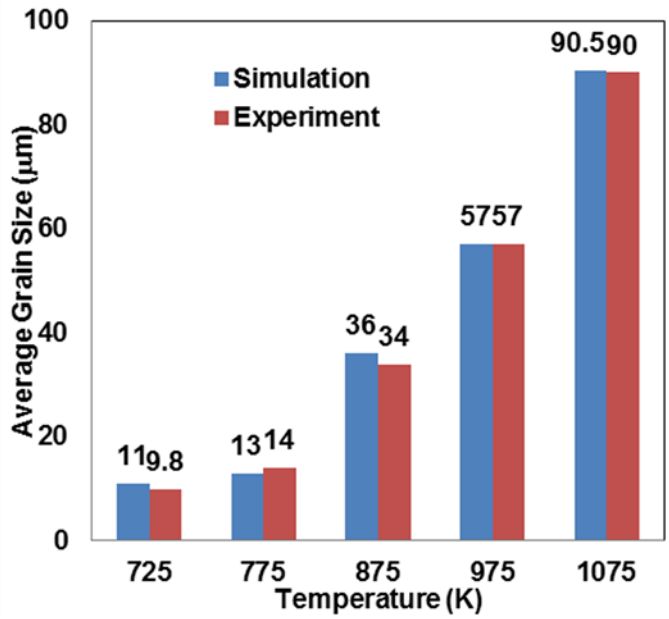

Figure 3-5: Comparison of the experimental [107] and predicted final grain structure of copper samples undergoing hot compression at 0.002 s^{-1} and varying operating temperatures.

The experimental study further evaluated the grain structure of the copper samples for the 775 K case at intermediate strains of 0.24, 0.44 and 0.6. At the initial

strain of ε=0.24, nucleated grains were observed at the grain boundaries of the initial microstructure. Furthermore, at ε=0.44 continued recrystallization is observed principally near the pre-existing boundaries and at ε=0.6, most of the material is recrystallized leaving a few initial grains untouched. The above kinetics are successfully compared with the predicted recrystallization kinetics in Figure 3-6. In Figure 3-6, SDV_N_REC is the recrystallization variable of the FE-CA framework showing the grain nucleation (N=1) and subsequent growth (N=2) for the 775 K case. SDV_PHI is the corresponding orientation variable to visualize the grain distortion due to recrystallization.

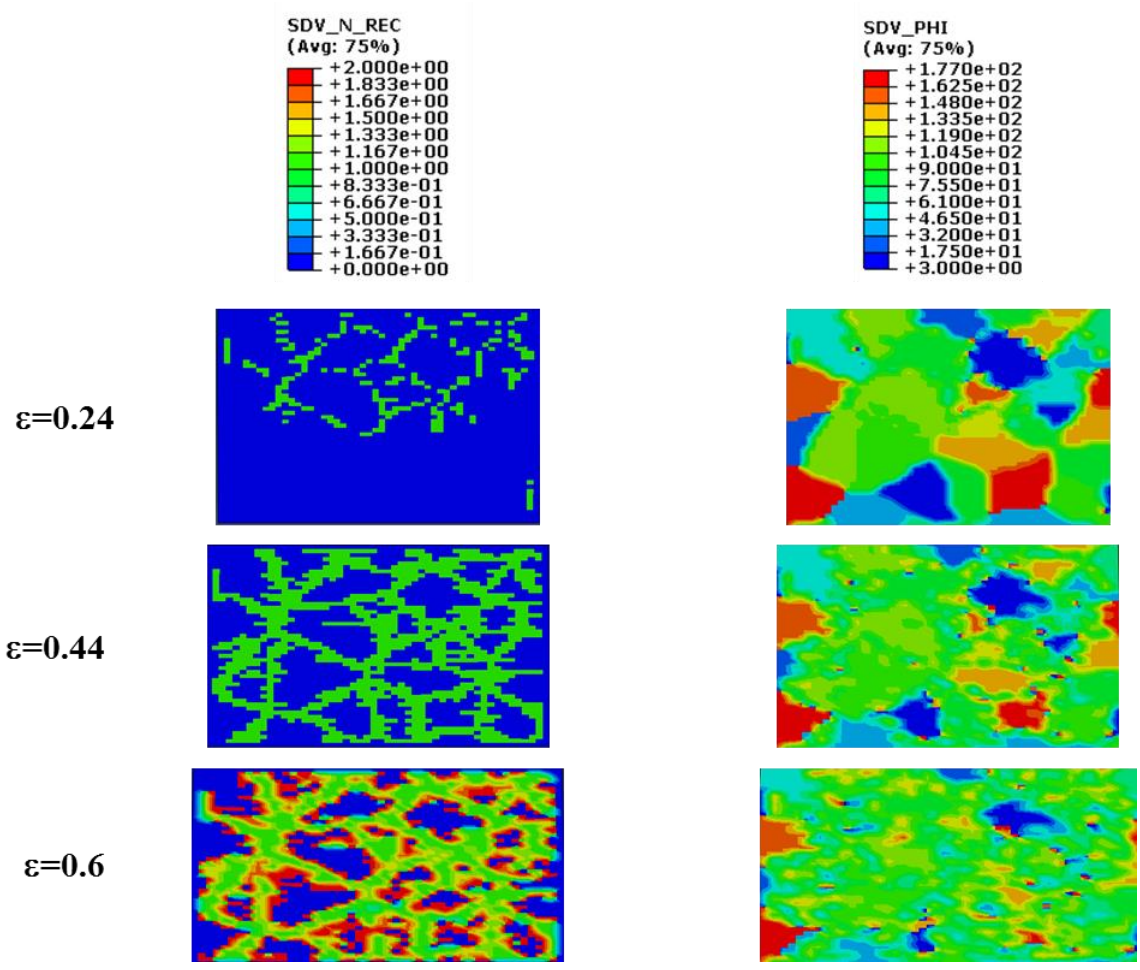

Figure 3-6: Evolution of the recrystallization kinetics for the 775 K case. SDV_N_REC is the recrystallization variable and SDV_PHI is the orientation variable.

3.1.2.2 Initial microstructure dependent recrystallization

The extent of recrystallization in a fine grained material of 11 μm compressed at $0.002s^{-1}$ and 775K is reported to undergo a small amount of coarsening to give a final grain size of 14 μm similar to the 78 μm initial microstructure case in Blaz et al. [107]. It is observed that the final grain size due to discontinuous dynamic recrystallization is independent of the initial grain size. An artificial microstructure with an initial average grain size of 11 μm is reconstructed using Dream 3D [106] to simulate the above-mentioned test as shown in Figure 3-7(a). The model accurately predicts a final average grain size of 13 μm with the distribution shown in Figure 3-7(b). The recrystallization kinetics based on energy relations successfully predicts the discontinuous dynamic recrystallization process with respect to varying temperatures and initial microstructure conditions.

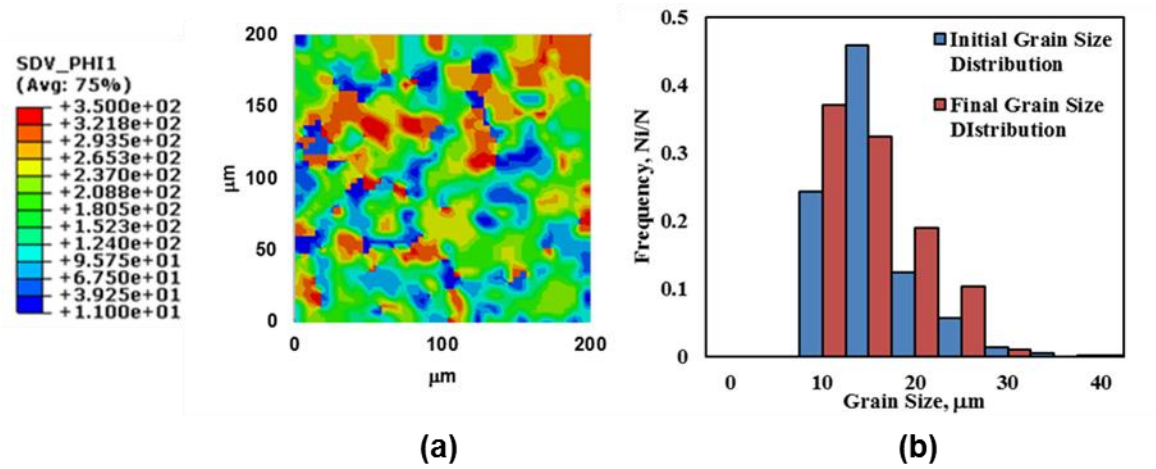

Figure 3-7: (a) Initial microstructure of grain size 11 μm mapped onto the FE-CA mesh in terms of the orientation variable (b) Initial and final grain size distribution of copper workpiece undergoing hot compression at 0.002 s^{-1} and 775 K.

3.2 Grain Evolution in the High Strain Rate Regime

To evaluate the model kinetics in the dynamic regime, a set of high strain rate experiments were designed to characterize the dynamic behavior of copper at multiple scales. The Kolsky bar or Split Hopkinson bar is a common tool used to characterize the flow stress behavior of materials deformed dynamically at high strain rates. Copper samples were subjected to constant high strain rate loading at room temperature in conjunction with microstructural characterization tests before and after loading to evaluate the extent of dynamic grain refinement. Furthermore, the fractured samples were subjected to varying heat treatment tests to track the corresponding recrystallization in terms of the discontinuous dynamic recrystallization phenomenon.

3.2.1 Experimental procedure

A Kolsky tension bar is utilized to characterize the dynamic response of copper loaded at a constant high strain rate of 2700 s^{-1} at room temperature, which occurs in the realm of 400 μs. To study the effect of initial grain size on the extent of dynamic grain size evolution, copper samples are subject to heat treatment tests of 450°C (30min), 600°C (1hr) and 900°C(35min) to obtain initial grain sizes of 30μm, 55μm and 174μm respectively.

The Kolsky bar setup can be referred to [92] with a schematic of a typical testing section seen in Figure 3-8. For the current experimental setup, the transmission bar is replaced with a load cell allowing for the direct detection of the force signal.

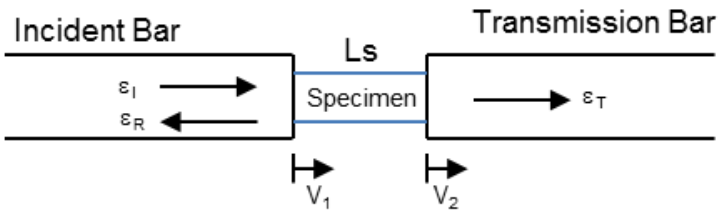

Figure 3-8: Testing section of Kolsky bar [92].

The incurred strain rate and strain from the sample are calculated based on the Kolsky bar relations [92] as follows:

$$\dot{\varepsilon} = \frac{c_b}{l_s}(\varepsilon_I - \varepsilon_R) \tag{17}$$

$$\varepsilon = \int_0^t \dot{\varepsilon} d\tau = \int_0^t \frac{c_b}{l_s}(\varepsilon_I - \varepsilon_R) d\tau \tag{18}$$

where c_b is the incident bar acoustic speed, l_s is the sample gauge length, ε_I is the incident bar strain and ε_R is the reflected bar strain. The axial force (F) is detected directly from the load cell and the corresponding engineering stress is given by $\sigma = \frac{F}{A_0}$, where A_0 is the initial cross-sectional area of the sample.

Copper samples of dimension 10 mm in length, 1 mm in width and 0.4 mm in thickness are loaded at a constant high strain rate of 2700 s^{-1} at room temperature. Figure 3-9(a) shows the recorded set of incident and reflected wave forms for the 30 μm case. Figure 3-9(b) shows the calculated (Equation (17)) strain rate history which is constant 2700 s^{-1}. The accuracy of the recorded dynamic response is validated by obtaining a constant strain rate signal.

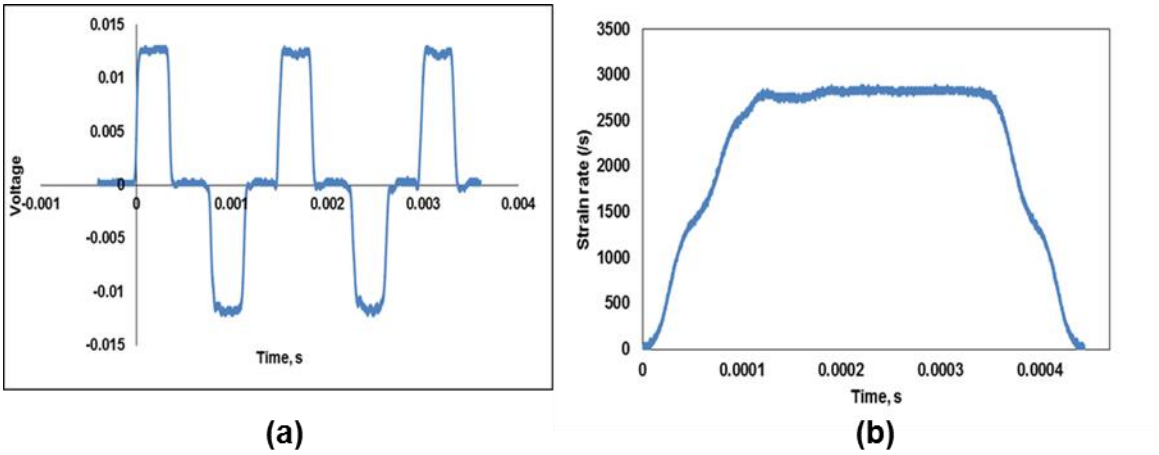

Figure 3-9: (a) Measured raw strain signal (b) Calculated strain rate signal (Equation (17)) during the dynamic loading of copper at a constant rate of 2700 s^{-1}.

3.2.2 Experimental results

3.2.2.1 Dynamic grain refinement

The average true stress-true strain responses for the three initial grain size cases are shown in Figure 3-10. There is approximately a 150 MPa difference of the ultimate tensile strengths between the smallest and largest initial grain size cases with the material getting weaker with increasing initial average grain size as shown in Table 3-1. Microstructural characterization performed before and after the loading tests found copper samples with initial average grain sizes of 30 μm, 55 μm and 174 μm get refined down to final average grain sizes of 7.2 μm, 5.7 μm and 4.3 μm respectively upon high strain rate loading at a constant 2700 s^{-1} as shown in Table 3-1. The optical micrograph for the 55 μm case is shown in Figure 3-11. By comparing the constitutive behavior and microstructural characterization of the three cases, it can be seen that as the initial average grain size of the microstructure increases, the material becomes weaker which impacts the extent of grain refinement during the dynamic loading tests. In addition, intergranular fracture modes were observed on the characterized surfaces of the samples.

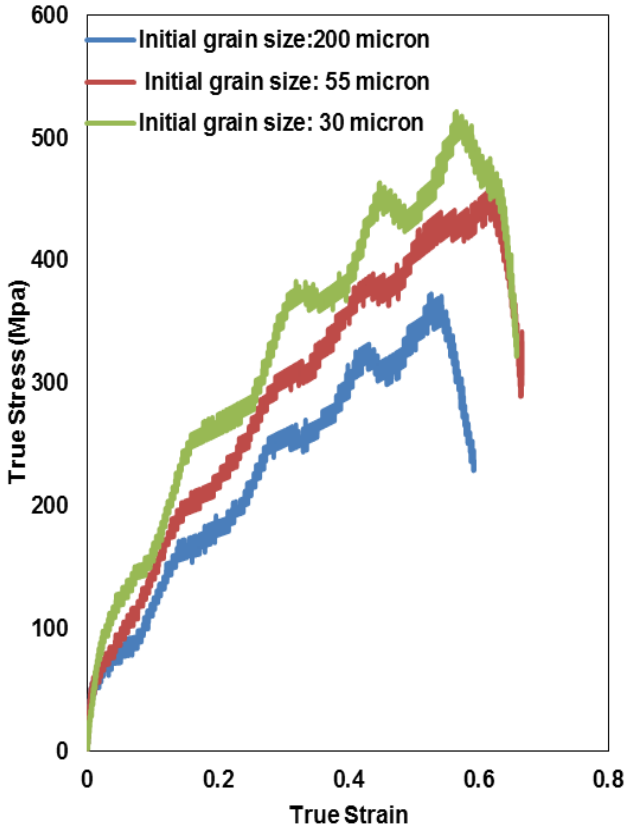

Figure 3-10: Stress-strain response of Copper deformed at a strain rate of 2700 s^{-1} with varying initial grain sizes of 30 μm, 55 μm and 174 μm.

Table 3-1: Dynamic response and microstructure evolution of copper with three initial grain sizes.

Sample	**Initial Grain size**	**Ultimate tensile stress (2700 s^{-1})**	**Final Grain size (Kolsky test)**
450°C (30min)	30μm	513 MPa	7.2 μm
600°C (1hr)	55μm	452 MPa	5.7 μm
900°C(35min)	174μm	363 MPa	4.3 μm

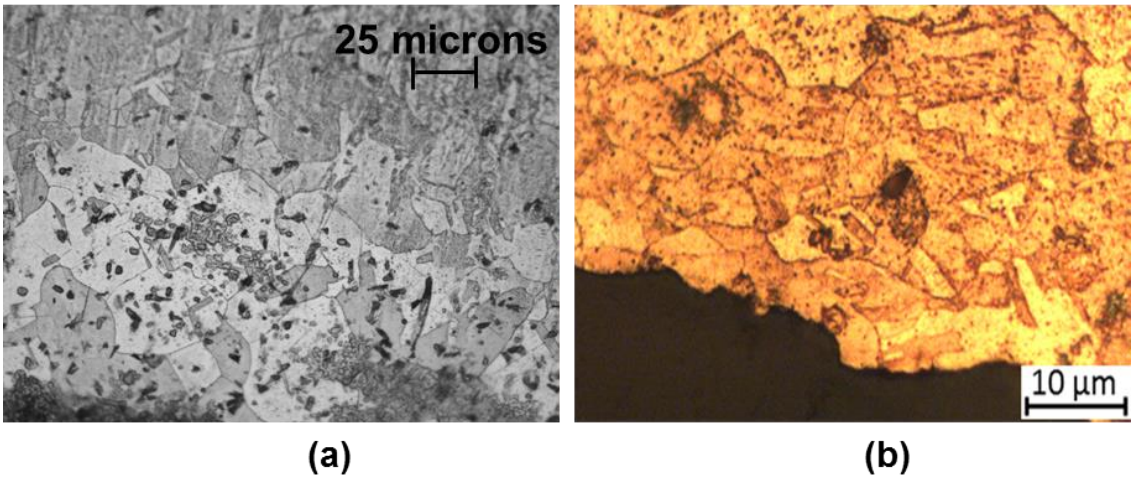

Figure 3-11: (a) Initial micrograph of copper with an average grain size of 55 µm (600°C (1 hr)) (b) Final micrograph with an average grain size of 5.7 µm upon dynamic loading at room temperature.

3.2.2.2 Dynamic grain coarsening

The fractured samples obtained from the loading experiments are heat treated to study the grain coarsening phenomenon on the dynamically loaded sample. The samples are subjected to two heat treatment tests at 600 ºC and 850 ºC for one hour each. Microstructural characterization of the heat treated samples show that the samples treated at 600 ºC (1hour) resulted in a final average grain size of 62 µm while the samples treated at 850 ºC (1 hour) resulted in a final average grain size of 85 µm as shown in Table 3-2. Unlike the dynamic grain refinement phenomenon, grain coarsening is independent of the initial average grain size of the microstructure. The optical micrographs of the two tests are shown in Figure 3-12**.**

Table 3-2: Dynamic microstructural evolution results following the heat treatment tests.

Sample	Initial Grain size	Final Grain size (Kolsky bar sample)
600°C (1hr)	7.2 μm, 5.7 μm, 4.3 μm	62 μm
850°C (1 hr)	7.2 μm, 5.7 μm, 4.3 μm	85 μm

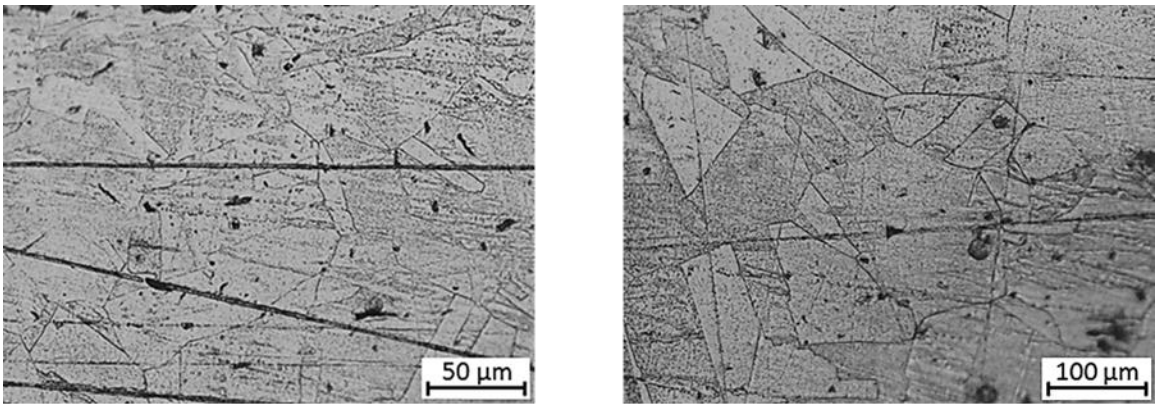

Figure 3-12: (a) Optical micrograph after heat treatment (600°C (1hr)) with a final average grain size of 62 μm (b) Optical micrograph after heat treatment (850°C (1hr)) with a final average grain size of 85 μm.

3.2.3 Modeling results

The above experiment is simulated with the developed multiscale model to predict the observed dynamic grain size evolution in terms of the grain refinement and coarsening. The Kolsky bar tests are simulated in the coupled temperature-displacement explicit regime. The initial microstructures are reconstructed as done previously and mapped onto the finite element mesh. It should be noted that a microstructure of length 1.5 mm and width 1mm is repeatedly mapped over the workpiece of length 10 mm and width 1 mm in accordance with the principle of ergodicity.

Copper samples with initial average grain sizes of 30 μm, 55 μm and 174 μm when loaded at a constant high strain rate of 2700 s^{-1} refine down to predicted final average grain sizes of 4.07 μm, 3.62 μm and 3.36 μm as shown in Table 3-3. The initial microstructure mapped to the mesh for the 55 μm case is shown in Figure 3-13.

Table 3-3: Comparison of the experimental and predicted dynamic grain refinement for copper loaded at 2700 s^{-1}.

Simulation case	**Initial Grain size**	**Predicted Final Grain size (Kolsky test)**	**Experimental Final Grain size (Kolsky test)**
450°C (30min)	30μm	4.07 μm	7.2 μm
600°C (1hr)	55μm	3.62 μm	5.7 μm
900°C(35min)	174μm	3.36 μm	4.3 μm

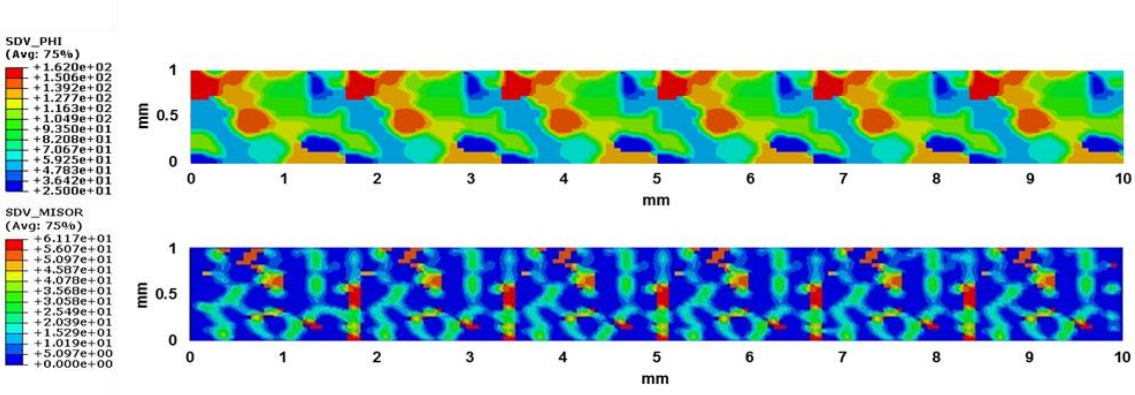

Figure 3-13: Initial mesh of the copper workpiece subjected to dynamic tensile loading at a constant strain rate of 2700 s^{-1} for the 55 μm case. SDV_PHI1 corresponds to the Euler angle (Φ) of the initial orientation and SDV_MISOR corresponds to the calculated grain boundary misorientation.

The post heat treatment experiments are simulated by importing the mesh from the Kolksy bar simulation as the initial state. Temperature boundary conditions are chosen in accordance with the testing parameters, which activate the grain growth

kinetics of the model. The model successfully predicts the fractured Kolksy samples when heat treated to a temperature of 600 ºC and 850 ºC for an hour yield a final average grain size of 64.4 μm and 90.4 μm respectively as shown in Table 3-4. The model successfully tracks the dynamic grains size evolution with respect to the varying initial microstructure conditions.

Table 3-4: Comparison of the experimental and predicted grain coarsening phenomenon of the dynamically loaded copper samples.

Simulation case	Predicted Final Grain size (Heat treatment sample)	Experimental Final Grain size (Heat treatment sample)
600°C (1hr)	64.4 μm	62 μm
850°C (1 hr)	90.5 μm	85 μm

3.3 Temporal Evolution of Dynamic Grain Refinement

The continuous X-rays generated by synchrotron radiation at the Advanced Photon Source (APS) at Argonne National Laboratory have been utilized to track and analyze the *in situ* damage and grain size evolution during the high strain rate loading of copper samples. The experimental results are compared with the developed model predictions to gain an insight into the grain refinement mechanism evolved during dynamic deformation processes.

3.3.1 Experimental setup

A Kolsky tension bar is utilized to characterize the dynamic response of copper loaded at a constant strain rate of 1200 s^{-1} which occurs in the realm of 200-300 μs. A modified Kolsky bar has been integrated with the high-energy X-rays at the 32-ID-B beamline of the APS at Argonne National Laboratory to conduct microstructure evolution

monitoring via simultaneous high-speed phase contrast imaging (PCI) and X-ray diffraction. The details of the experimental setup in terms of the design of the modified Kolsky bar with the integration of the synchrotron X-rays are reported in [93, 94]. A schematic of the setup is shown in Figure 3-14. The setup allows for in-line phase contrast imaging and *in situ* diffraction detection simultaneously. The phase-contrast images are collected using a scintillator-coupled high-speed camera (FastCam SA-Z, Photron USA Inc). The diffraction detection system consists of a scintillator, an image intensifier (Quantum Leap, Stanford Computer Optics Inc), and a high-speed camera (FastCam SA-Z, Photron USA Inc).

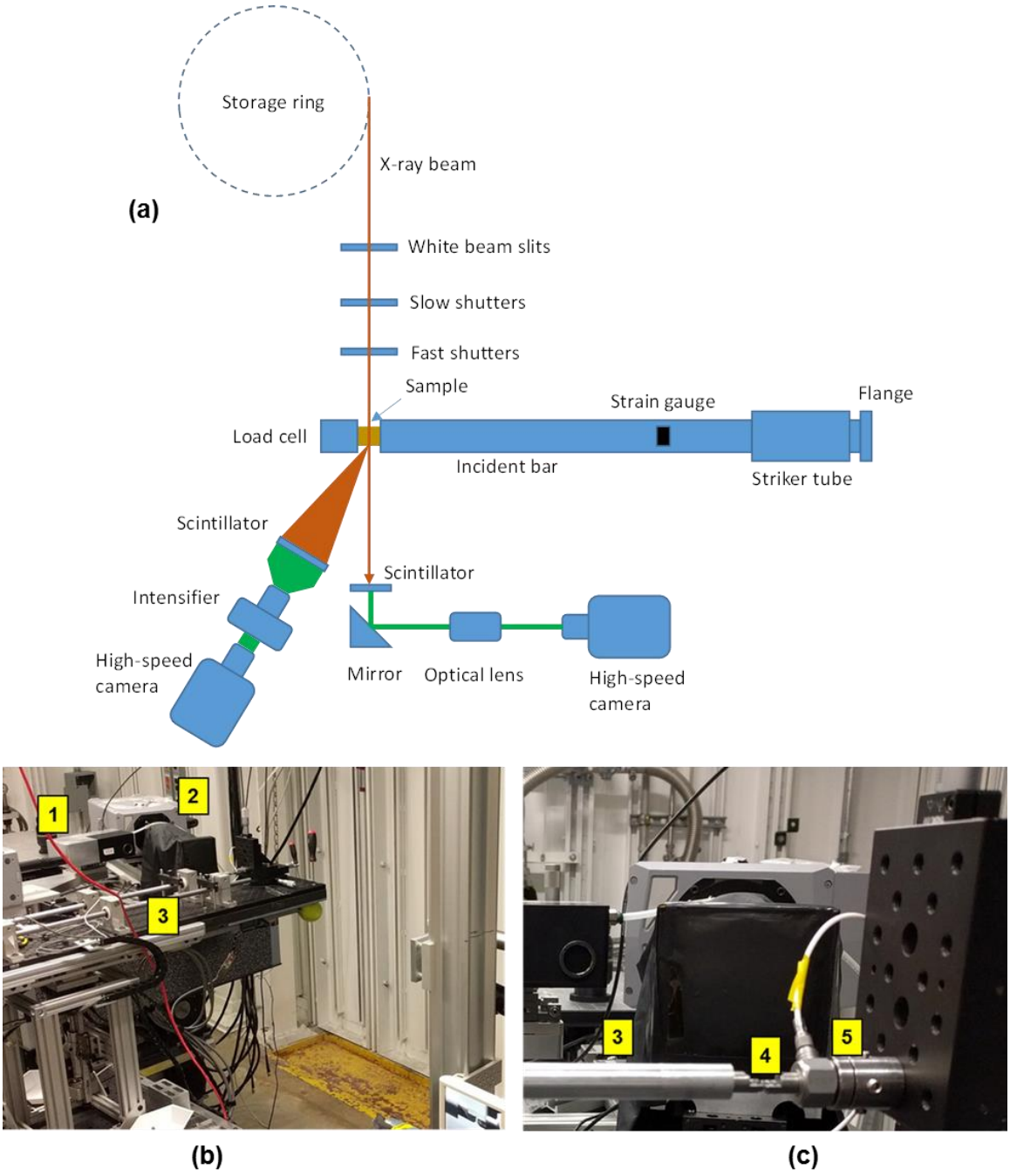

Figure 3-14: (a) Schematic of integrated Kolsky bar apparatus and the 32-ID-B high-speed X-ray beamline at APS [94] (b) Photographs of the setup in the beamline hutch marked (1) High-speed camera used for PCI (2) ICCD camera used to record the diffraction pattern (3) Kolsky tension bar and (c) (4) copper sample setup and (5) Load cell.

The X-ray beamline utilized is equipped with an undulator of period 1.8 cm and length 2.4 m. [94]. The undulator gap determines the flux and energy spectrum of the incident X-ray photons. In this study, an undulator gap of 11 mm is chosen for which the first harmonic energy is 23.66 (keV). The calculated raw energy spectrum and the spectrum with absorption effects are shown in Figure 3-15.

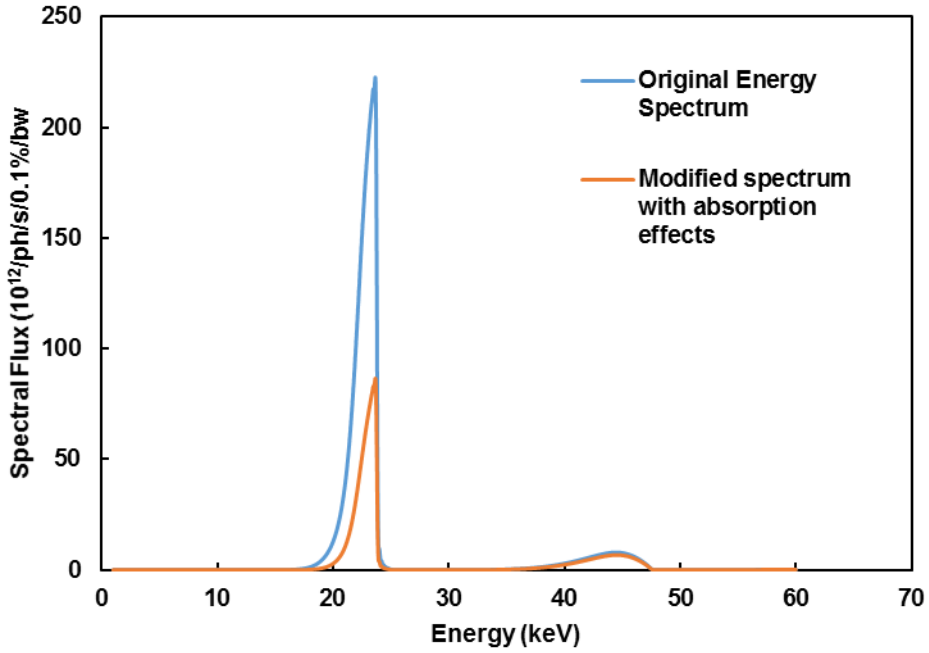

Figure 3-15: Comparison of the calculated raw energy spectrum and the spectrum with absorption effects with an undulator gap of 11 mm.

The collected X-ray diffraction patterns were analyzed using the in-house program *HiSPoD* [108]. The program simulates and analyzes diffraction patterns obtained from polycrystalline samples. For conducting simultaneous imaging and diffraction, the diffraction detector has to be positioned at some offset angle from the incident direction without blocking the transmitted beam. In this experiment, the area detector is placed at an offset angle of 15.4° from the incident beam direction to obtain the strongest

diffraction peaks from the sample. A schematic of the diffraction geometry pertaining to the experimental setup is shown in Figure 3-16 where *O* is the point where the X-ray beam and sample interacts; *O'* is the transmitted beam position on the detector plane; *A* is the scattered beam position on the detector; *q* is the scattering wavevector and *2θ* is the diffraction angle [108]. For the given detector location and X-ray energy (1st harmonic, 23.66keV), the scattering vector q and azimuthal angle φ at each pixel position on the detector is calculated using the software *HiSPoD* and shown in Figure 3-16.

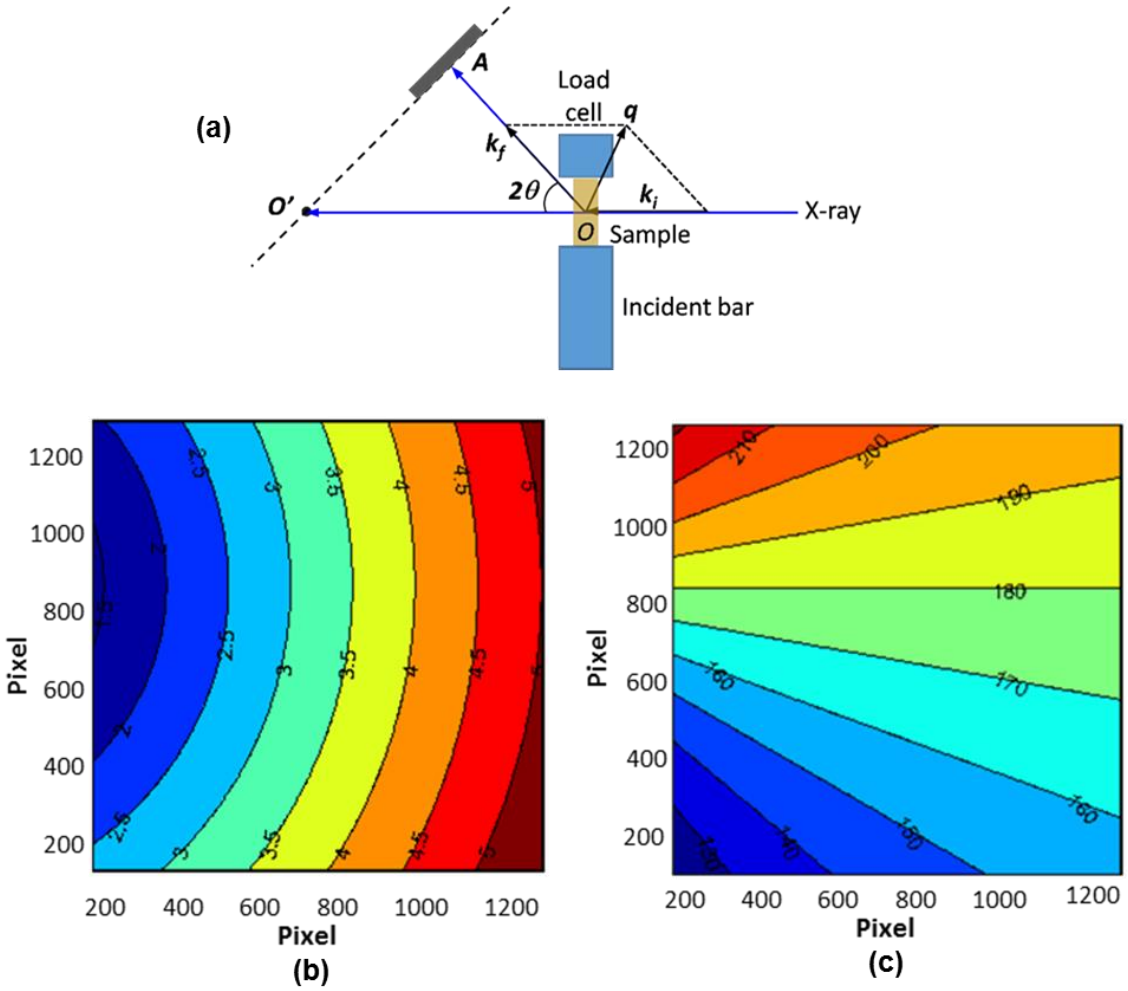

Figure 3-16: (a) Diffraction geometry of the experimental setup where the area detector is placed at an offset angle from the incident beam direction. The calculated (b) scattering vector q map and (c) azimuthal angle φ map when the detector angle is 15.4° and the X-ray energy is 23.66 keV.

3.3.2 Experimental results

The Kolsky bar is utilized to perform high strain rate tensile tests on copper samples of length 10 mm, width 1 mm and thickness 0.07 mm at a constant strain rate of 1200 s^{-1} repeated ten times. The details of the bar setup and properties are reported in [94]. The incurred strain rate and strain from the sample have been calculated based on the Kolsky bar relations from Equations (17) and (18). The incident bar acoustic speed is 5051.86 m/s for the current set up and the sample gauge length is 1mm for the conducted experiments.

Figure 3-17(a) shows the recorded set of incident and reflected wave forms from the strain gauge during a single loading experiment. Figure 3-17(a) shows the calculated (Equation (1)) strain rate history which is a constant 1200 s^{-1}. The accuracy of the recorded stress-strain response is validated by obtaining a constant strain rate signal. Furthermore, the average true stress-true strain response is shown in Figure 3-18 with demarcated points at which the diffraction patterns and images were recorded. Error bars marked on the curve show that the observed uncertainty in measurements is negligible. Five phase-contrast images and diffraction patterns are captured during the loading test at a frequency of 20 kHz with exposure times of 250 ns and 20 μs respectively. Concurrently, for the approximate 200 μs loading regime, images and diffraction patterns were captured every 50 μs. The dynamic range of the imaging and diffraction detectors is 10-bit. The field of view includes a pixel resolution of 2 μm and the volume being probed is 0.00672 mm^3. The sequence of phase-contrast images and the corresponding diffraction patterns are shown in Figure 3-19**.** The images indicate the fracture point of

the sample during the dynamic loading experiment and the diffraction patterns are analyzed to study the *in situ* temporal grain size evolution in the samples.

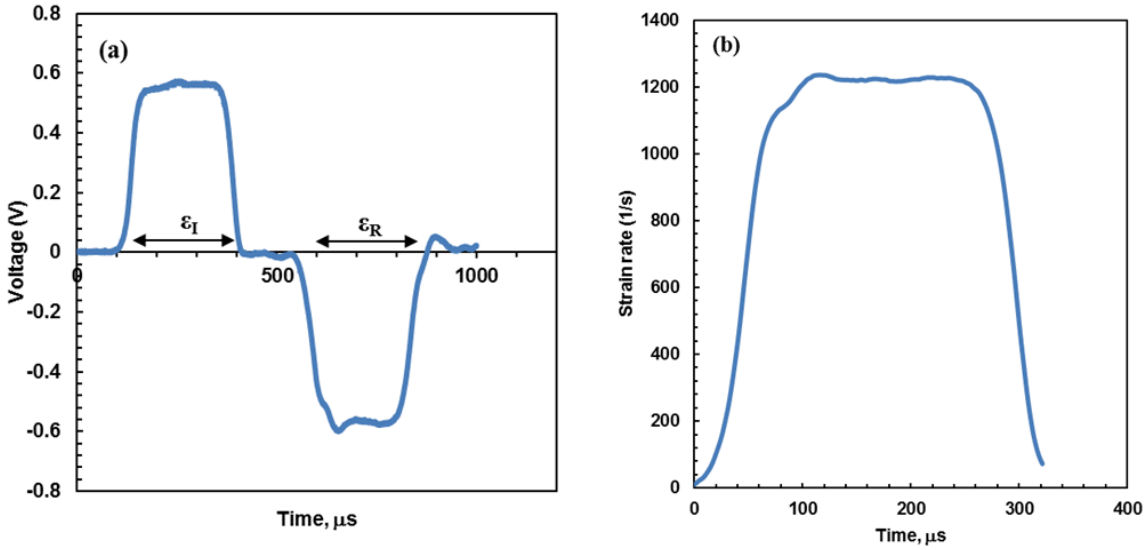

Figure 3-17: (a) Detected raw strain signal where ε_I is the incident strain and ε_R is the reflected strain (b) Calculated strain rate signal (Equation (1)) during the dynamic loading of copper showing a constant rate of 1200 s^{-1}.

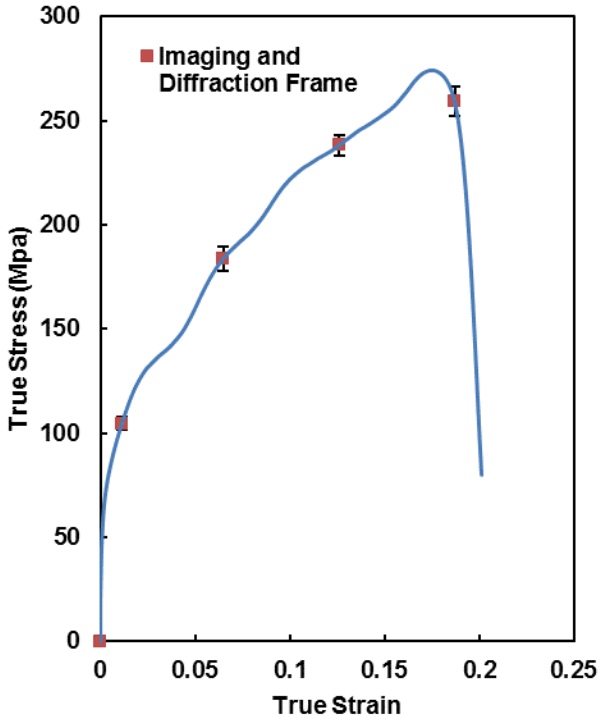

Figure 3-18: Stress-strain response of copper deformed at a strain rate of 1200 s^{-1}. The curve is demarcated with symbols at points where the phase contrast images and diffraction patterns were recorded.

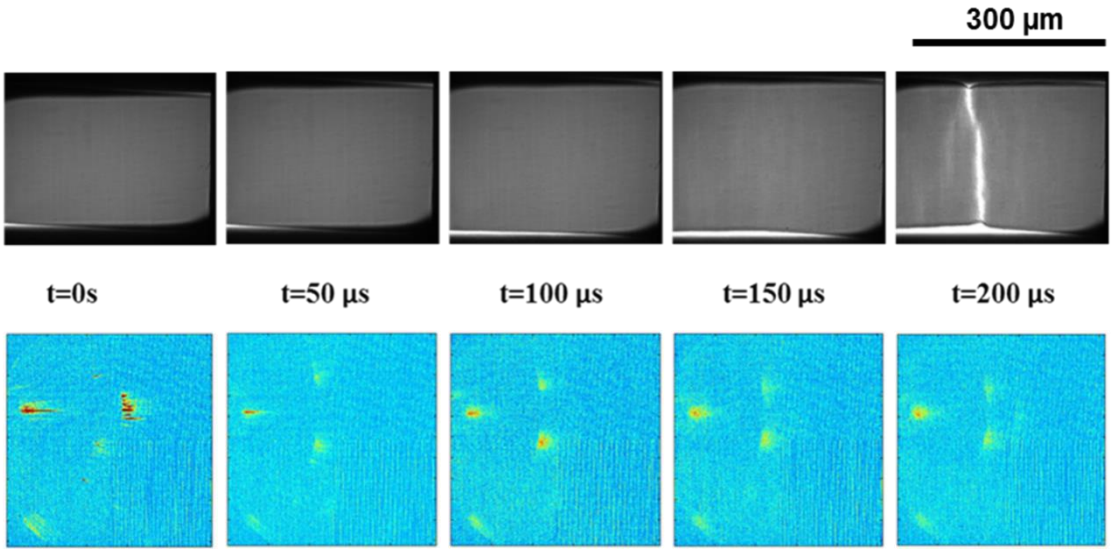

Figure 3-19: Sequence of phase contrast images and diffraction patterns captured during the dynamic deformation of copper.

3.3.2.1 X-ray diffraction analysis

The microstructure evolution analysis of the copper sample is conducted on the fracture domain because of the limitations of the maximum sample volume that can be probed by the Synchrotron X-rays. The grain structure characterization and analysis is conducted around the probed fracture domain before and after the loading experiment. It is found that the copper samples with an initial measured average grain size of 36 μm, refines down to a uniform fine-grained structure of size 6.3 μm upon dynamic loading as shown in Figure 3-25. The microstructure characterization results are further detailed in the upcoming section. The recorded diffraction patterns are further analyzed using the previously mentioned software *HiSPoD.*

Figure 3-20(b) and Figure 3-20(c) show the recorded diffraction patterns before and after 200μs of tensile pulling overlaid with the simulated first and second selected harmonic peak indexing respectively. For reference purposes, a simulated diffraction pattern demarked with the peak positions for first and second selected harmonic energies based on the experimental parameters is shown in Figure 3-20(a). The peak positions for the first harmonic energies are marked with cyan bands while the second harmonic energy is marked with yellow bands. They correspond to the X-rays with the energy spectrum shown in Figure 3-15. The diffraction signals indicate the detection of a few grains which is expected based on the small sample size and initial coarse grain size. The several closely spaced streaks correspond to the same grain. The sample containing coarse grains with strain gradient generates streak-like diffraction patterns as observed in Figure 3-20(b). The mosaic structure observed in Figure 3-20(c) indicates the azimuthal broadening of the detected diffraction peaks. The high rate loading induces defects (mosaic structure) generation involved in the plastic deformation process. Furthermore,

the observed refined grain structure (Figure 3-24) in the fractured samples indicates that the dislocations and other defects break the coarse grains into mosaics, manage to connect into a network and become the boundaries of smaller grains.

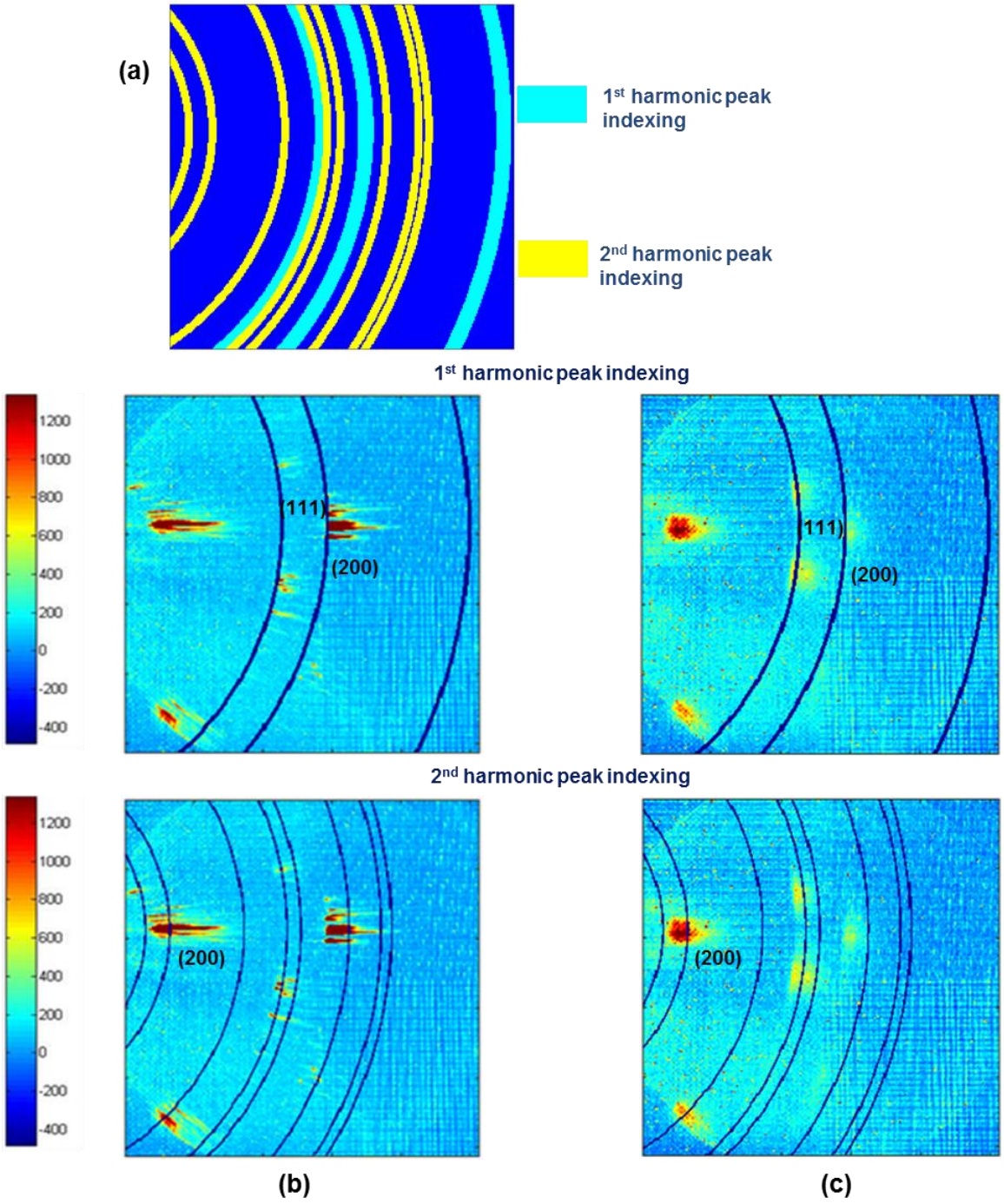

Figure 3-20: (a) Simulated diffraction peak positions for the first harmonic energy on the cyan bands and second harmonic energy on the yellow bands. Experimental diffraction patterns before and after 200 μs of loading overlaid with (b) first harmonic peak indexing and (c) second harmonic peak indexing.

The efficiency of the diffraction detector utilized is not high enough to capture the diffraction from weakly scattering atomic planes without compromise to the time resolution, and hence the analysis has been conducted on the strongest diffraction peaks. By radially averaging the two dimensional diffraction patterns (Figure 3-20), the integrated one dimensional intensity profiles of the static frame and the fracture frame are shown in Figure 3-21(a). Furthermore, the integrated one dimensional profiles of the diffraction patterns at all the captured frames (20 kHz) against all the azimuthal angles corresponding to the Cu (111) at the 1st harmonic energy and Cu (200) at the 2nd harmonic energy peaks are plotted in Figure 3-22(a) and Figure 3-22(b) respectively. It should be noted that in the figure the loading begins from the demarcated Frame 4, with three static frames captured prior to the loading. It is observed that there is a significant drop in the intensity between the frames, thereby indicating peak broadening of the diffraction profiles brought about by the defect density increase. The one dimensional intensity profiles for the observed diffraction peaks at all the recorded frames are quantified by plotting the full width at half maximum (FWHMs) of the observed peaks shown in the conventional Williamson-Hall plots as a function of K [21] shown in Figure 3-21(b)**.** The Williamson-Hall plot illustrates the temporal evolution of the peak broadening (FWHM) throughout the loading experiment which corroborates the prevalance of the grain refinement phenomenon. Here $K = 2sin\theta/\lambda$, FWHM = $\Delta\lambda = 2cos\theta(\Delta\theta)/\lambda$, θ and λ are the Bragg angle and the wavelength, respectively. The grain structure observations, quantitative Williamson-Hall analysis indicating peak broadening as well as the observed diffraction patterns characterized by the mosaic structure corroborates the prevalence of the grain refinement phenomenon during the high rate loading regime.

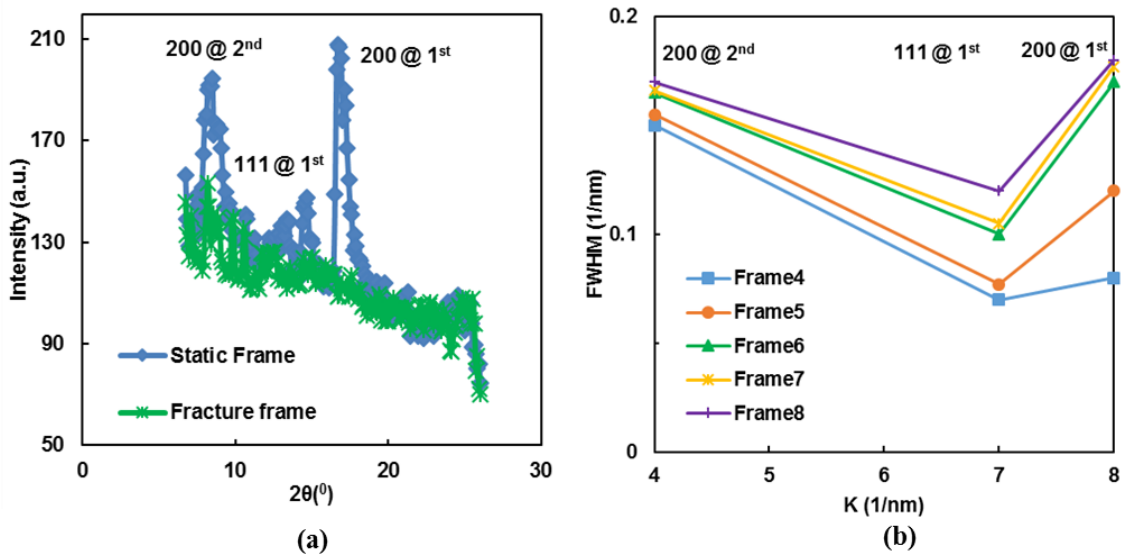

Figure 3-21: (a) One dimensional intensity profiles of the static and fracture diffraction frames (b) Williamson-Hall plots of the series of captured diffraction frames during the high strain rate loading of the specimen at the observed peaks (Frame 4 corresponds to the loading frame further referenced in Figure 3-22).

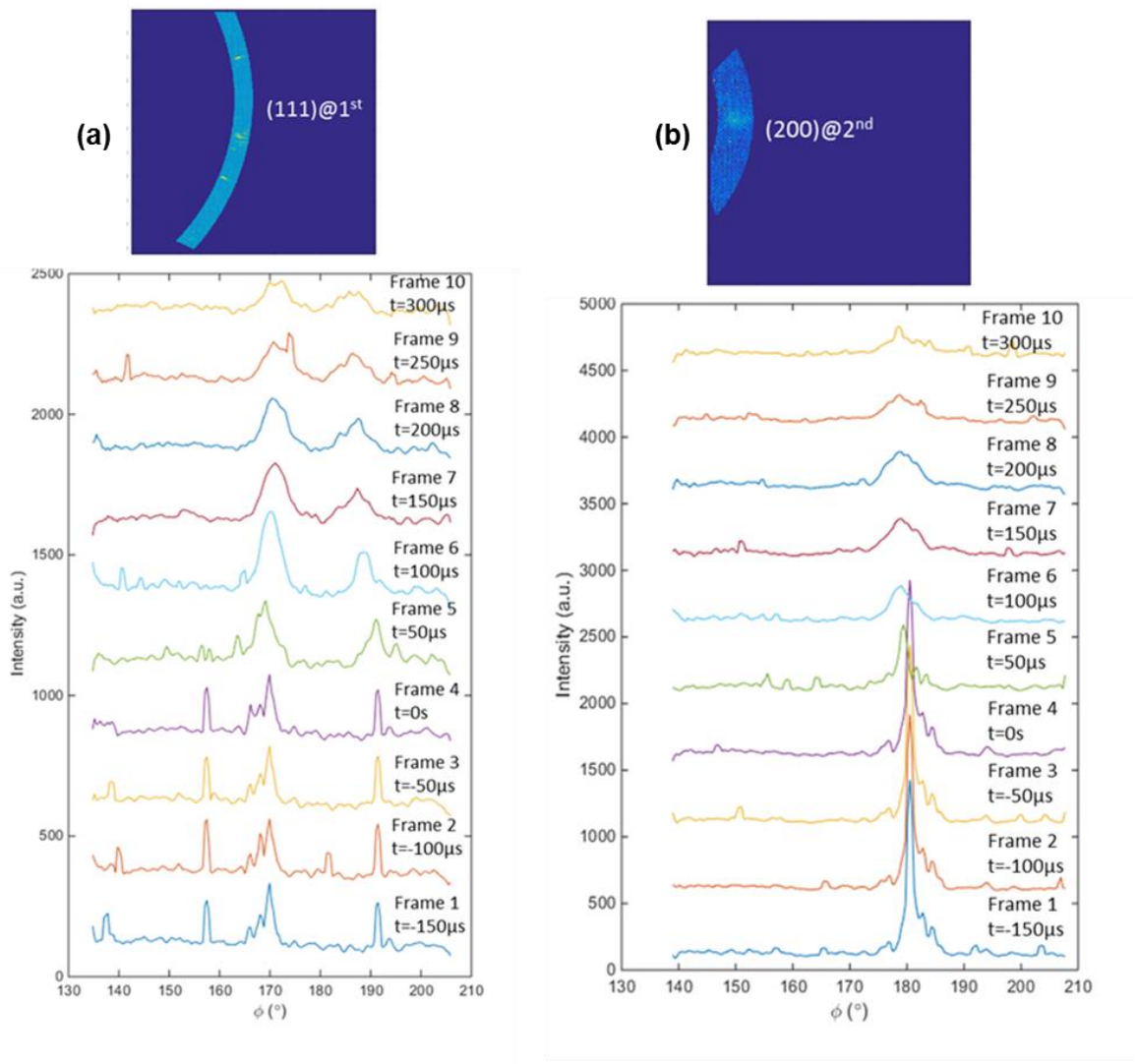

Figure 3-22: One dimensional intensity profiles of the recorded patterns for the chosen diffraction peaks (a) Cu (200) and (b) Cu (111) with respect to the azimuthal angles. It should be noted that a couple of static frames (Frame 1- Frame 3) are taken prior to the loading of the specimen which begins from Frame 4.

3.3.2.2 Grain size evolution

Microstructural characterization is conducted on the samples before loading and upon fracture to assess the extent of grain refinement in terms of its grain structure and average grain size. The characterization is conducted in the fracture domain as it is the chosen volume probed by the Synchrotron X-rays. The samples are mechanically polished and

chemically etched to reveal the grain structure. The copper samples undergoing dynamic loading have an initial average grain size of 36 µm as shown in Figure 3-23. The final average grain size obtained on fracture is 6.3 µm as shown in Figure 3-24. The initial and final grain size distributions of the fracture domain are are further shown in Figure 3-25.

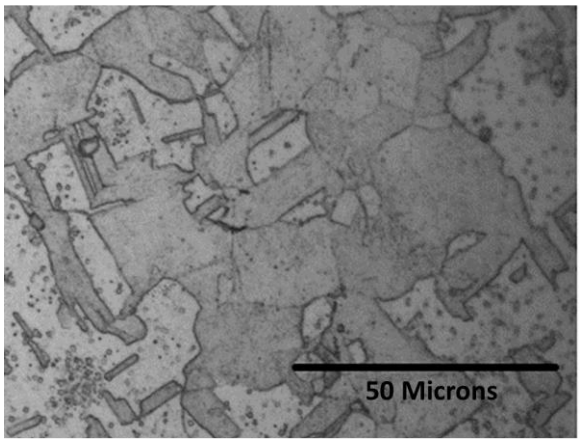

Figure 3-23: Initial microstructure of the copper sample before loading with an initial average grain size of 36 µm.

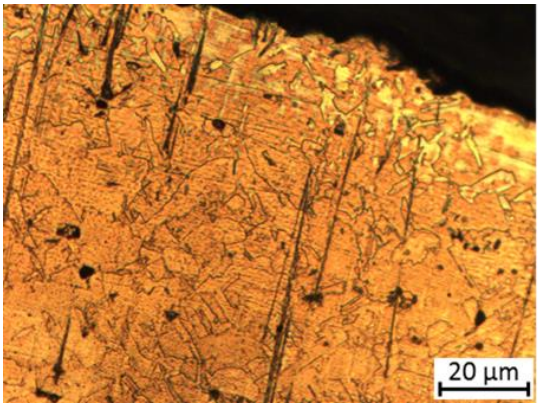

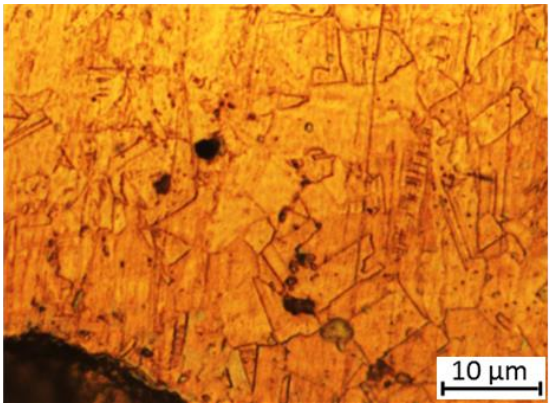

Figure 3-24: Optical micrographs of the copper sample on fracture with a final average grain size of 6.3 µm.

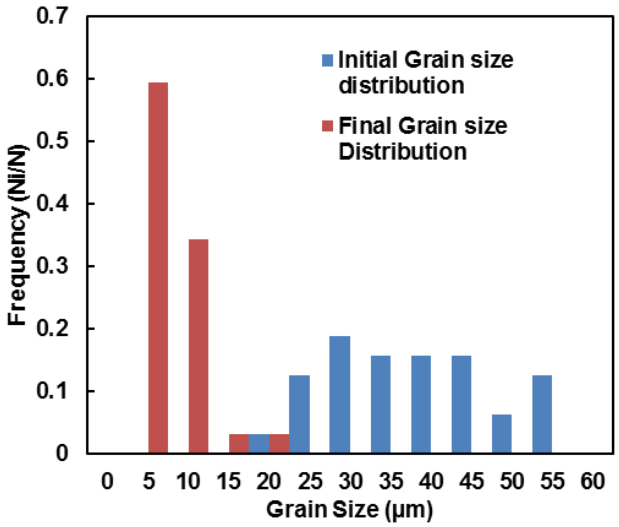

Figure 3-25: Initial and final grain size distribution of a copper sample dynamically loaded at a strain rate of 1200 s^{-1}.

The normalized rate of change of the peak broadening factor (FWHM) is calculated from the Williamson-Hall plot between each recorded diffraction frame which is the rate of grain refinement occurring throughout the loading process shown in Figure 3-26(a). The average rate of change is computed based on the rate of change formulation for a function between two points as $\frac{f(b)-f(a)}{b-a}$. The plot shows that there is a significant jump in the broadening rate (>0.25) from the demarcated Frame 5 (Refer Figure 3-22) beyond which the rate of broadening increases at a relatively constant rate. This frame (Frame 5) corresponds to the point beyond t=50 μs of the experiment with each frame taken at a frequency of 20 kHz as mentioned previously. By obtaining the function for the rate of refinement throughout the loading and the initial and final grain sizes, the grain sizes are calculated for the entire loading process as a function of time in Figure 3-26(b). The experiment records strain with respect to the loading time shown in Figure 3-17 and Figure 3-18. This is in turn utilized to illustrate the grain evolution with respect to the strain in Figure 3-26 and Figure 3-27. On comparing the time with the calculated flow

stress behavior (Figure 3-18), it is found that the initiation of grain refinement for copper loaded at a strain rate of 1200 s^{-1} develops between the second and third recorded frame corresponding to between the strains of 0.011 and 0.064. At this point, the initial fine grains are formed around the pre-existing grain boundaries. On further analysis of the peaks beyond the initiation point, it is found that the extent of peak broadening increases at an equivalent rate as shown in Figure 3-26, corroborating the continuous nature of the grain refinement mechanism. Beyond the initiation point, the pre-existing grains continue to disintegrate at a continuous rate, resulting in a fine grained microstructure on fracture **(**Figure 3-24 and 3-25).

By comparing Figure 3-26 and Figure 3-27, the slope of the plots is maximum between the strains of ε=0.011 and ε=0.064 (t=50 µs – t=100 µs) which is the yielding regime of the flow stress curve (Refer Figure 3-18). It is hypothesized that the initiation of the grain refinement mechanism occurs at this point of loading. Furthermore, it can be seen that the grain size is refined by 65% (36 µm to 16.7 µm) during the first 100 µs of loading and by 35% (16.7 µm to 6.3 µm) during the next 100 µs of loading. This indicates that the majority of the fine grains are formed immediately after the initiation of the grain refinement mechanism, beyond which the fine grains continue to develop at a lower constant rate due to strain hardening (Refer Figure 3-27). Hence, this experimental method successfully allows for the *in situ* detection of the initiation and temporal evolution of the grain refinement phenomenon during the dynamic loading of copper.

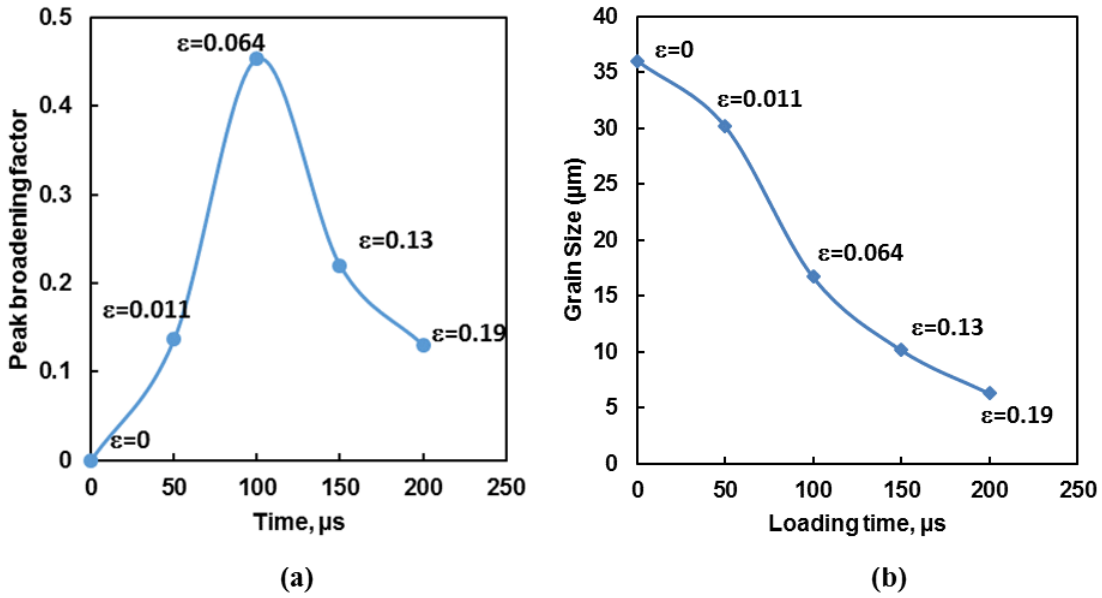

Figure 3-26: (a) Time evolution of the normalized peak broadening factor demarcated with the recorded loading strains during the dynamic loading of copper (b) Time evolution of the grain refinement mechanism calculated from the rate of change of the recorded peak broadening during the dynamic loading of copper.

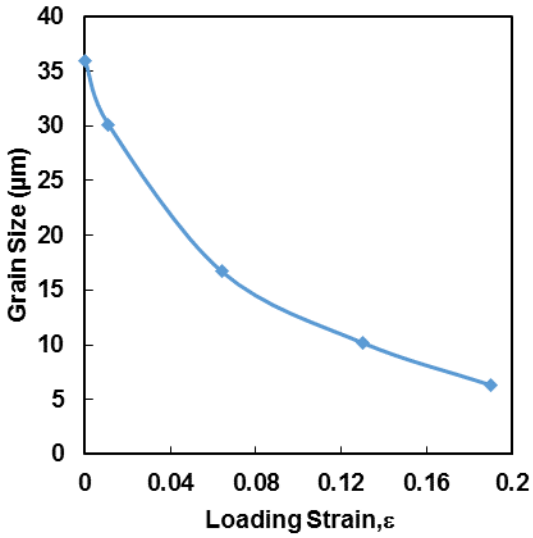

Figure 3-27: Grain size evolution during the dynamic loading of copper at a strain rate of 1200 s^{-1}.

3.3.3 Modeling results

The initial microstructure with an average grain size of 36 µm is mapped onto the workpiece mesh of Copper via state dependent variables (SDVs) as shown in Figure 3-28. It should be noted that texture and grain orientation evolution has not been taken into account in this model. The grains and grain boundaries are identified and tracked throughout the loading process via the Euler angle formulation. The Euler angles are assigned to the grains based on a random orientation distribution. A microstructure of size 2 mm by 1mm is repeatedly mapped over the workpiece of size 10mm by 1mm in accordance with the principle of ergodicity. Furthermore, a uniform initial dislocation density is assumed for all the grains as the effects of the crystal orientations and reorientations is not taken into account. The assumption is reasonable as the primary focus of the study is the grain size and structure evolution of the whole workpiece/domain rather than individual grains. The initial dislocation density parameters have been assigned as shown in Table 2-1. The time step for the simulation has been chosen as 20ns.The size of the finite element is chosen to be 0.8 µm, which is approximately 8 times smaller than the average observed grain size and allows for computationally efficient simulations.

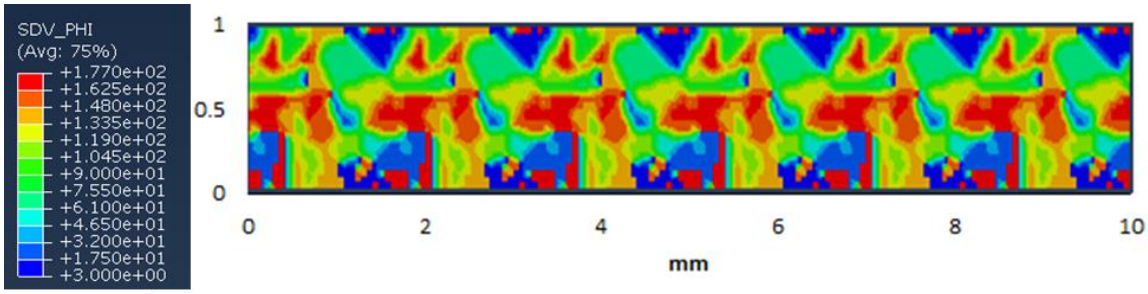

Figure 3-28: Initial mesh of the copper workpiece subjected to dynamic tensile loading at a constant strain rate of 1200 s^{-1}. SDV_PHI1 corresponds to the Euler angle (Φ) of the assigned orientation of the grain. It has been utilized to depict the microstructure.

The developed model kinetics accurately predicts the temporal evolution of the grain refinement mechanism recorded by the dynamic loading experiment. During the dynamic tensile loading of copper at a constant strain rate of 1200 s^{-1}, the model predicts that copper with an initial average grain size of 36 μm is refined to a final average grain size of 2.4 μm. By further analyzing the time kinetics of the regime, it is seen that the sub-grain misorientation value exceeds 15° at a strain of 0.04 which is close to the detected initiation value of 0.011. Once the θ_{sub} value exceeds the 15°, the probabilistic cellular automata scheme is activated to predict the recrystallization sites. The results are further post-processed to calculate the extent of grain refinement based on the predicted recrystallization sites. The predicted time evolution kinetics of the grain refinement mechanism is compared with the experimental results in Figure 3-29. The model results agree well with the experimental findings in terms of the initiation as well as the rate of grain refinement throughout the process. However, there is a slight deviation in the predicted value of the refined grain sizes where the model overestimates the final average grain size value throughout the process. This can be attributed to the predicted sub-grain misorientation values, which result in the recrystallization and disintegration of the original grains. The predicted sub-grain misorientation (Equation (8)) is overestimated at the dynamic conditions. Figure 3-30 shows the simulation contours of the multiscale model in terms of the strain, recrystallization switching variable (N) and the grain orientation in terms of the Euler angle (Φ) respectively on fracture at 200 μs of loading. The recrystallization switching variable and grain orientation variable contours have been depicted primarily for visualization of the predicted recrystallization sites and change in

microstructure. Furthermore, they are postprocessed to calculate the final average grain size and distribution.

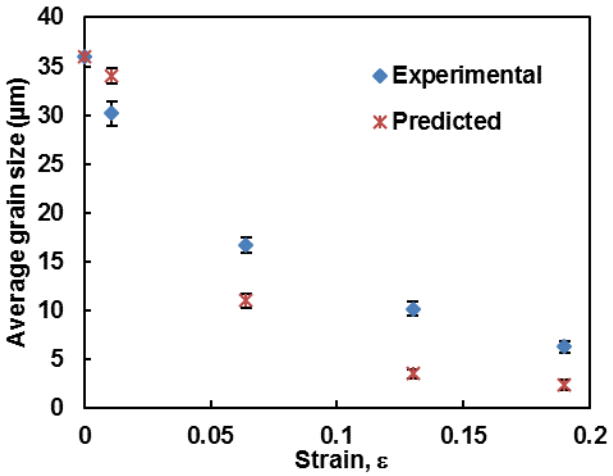

Figure 3-29: Comparison of the predicted time evolution kinetics of the grain refinement mechanism with the experimental results during the high strain rate loading of copper.

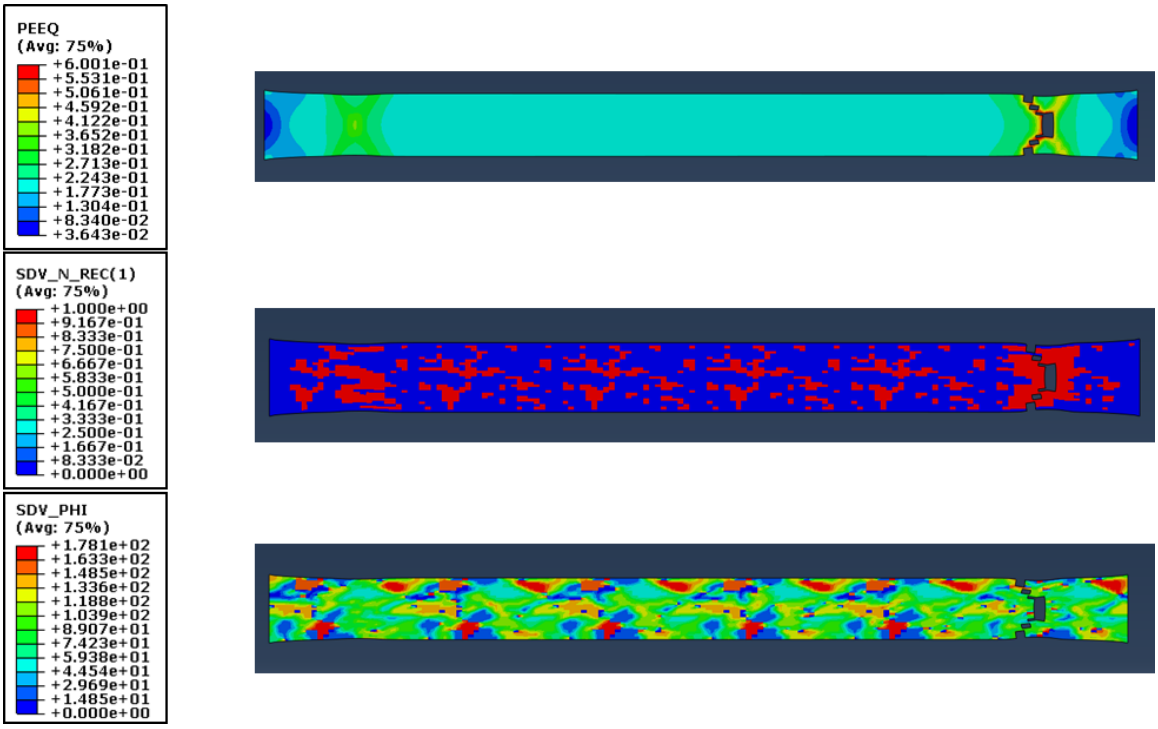

Figure 3-30: Predicted simulation contours of the multiscale model of Copper undergoing high strain rate tensile loading. PEEQ corresponds to the strain, SDV_N_REC corresponds to the recrystallization switching variable activated by the cellular automata framework and SDV_PHI corresponds to the grain orientation variable in terms of the Euler angle (Φ).

4. DYNAMIC RECRYSTALLIZATION IN AL 6061-T6 ALLOY DURING FRICTION STIR SPOT WELDING

In this chapter, the developed dynamic recrystallization model is implemented to predict the extent of dynamic recrystallization developed during the friction stir spot welding of Al 6061-T6 with varying tool rotational speeds. The experiments show that the original microstructure of the stir zone is completely replaced by a recrystallized fine grained microstructure with the final average grain size and morphology dependent on the process parameters. The model accurately predicts the process temperature rise with increasing tool rotational speeds which results in higher rate of grain coarsening during the dynamic recrystallization phenomenon.

4.1 Experimental Procedure

Friction stir spot welding was performed on Al 6061-T6 plates using a Mazak VQC-15/40 vertical machining, which were 6.35 mm thick. The AISI H13 grade steel FSW tool was used in this experiment, which is same as the one used by Davis et al. [110]. A three axis Kistler 9257B dynamometer, which is connected to a Kistler 5004 amplifier, is used to measure the welding forces. A pyrometer (Micro epsilon CTVM-3H2SF-C3) is used to measure temperature in front of the tool. The experimental setup is shown in Figure 4-1.

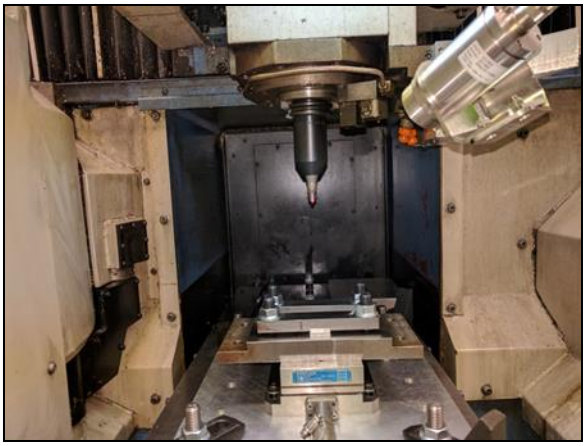

Figure 4-1: Experimental Setup of FSSW on Al 60601-T6 plates.

The chosen plunging speed was 20 mm/min and the plunge depth was 0.11 mm. Two rotational speeds of 1500 and 2500 rpm were chosen for this experiment. The emissivity of the pyrometer was determined using thermocouples to measure reference temperatures. The workpiece was heated up to 500 °C using a heating pad and then allowed to cool. This heating-cooling cycle was recorded by the thermocouples and was later compared with the data captured by the pyrometer. Emissivity value of 0.29 showed the best fit with the experimental results and utilized for the temperature measurements during the experiments.

To track the grain size evolution throughout the process, microstructure characterization tests are performed on the Al 6061-T6 plates before and after the experiment. The plates are sectioned across the stir zone, mechanically polished and chemically etched to reveal the grain structure. The experiment is repeated three times and the macroscopic and microscopic results are discussed in the upcoming section.

4.2 Results and Discussion

The model results are compared at both the macroscopic and microscopic scales. At the macroscopic scale, the recorded forces and temperatures are compared with the predicted finite element model results. At the microscopic scale, the predicted grain size evolution due to recrystallization is compared with the optical micrographs.

4.2.1 Macroscopic results

As deformation during the friction stir welding process is localized, the domain size (20 mm x 20 mm) considered for the FE model is chosen to be four times the size of the shoulder diameter. The thickness is modeled based on the thickness of the plates used in the experiment, which is 6.35 mm. The FE model assembly and mesh is shown in Figure 4-2. The FSW tool (red) and backing plate (grey) are modeled as a rigid isothermal Lagrangian body, whereas ALE (Arbitrary Lagrangian Eulerian) formulation is used for the deformable workpiece (green) to prevent distortion of elements during the analysis. The entire assembly is meshed with C3D8RT elements (hexahedral elements with 8-nodes, with trilinear displacement and temperature degrees of freedom) and biased meshing is used where the tool is in direct contact with the workpiece. A similar model has been previously used by Darko et al. [111].

The material properties of Al 6061-T6 and interaction at the tool-workpiece interface are same as the one proposed in the paper by Fadi et al. [112]. Heat loss due to conduction at both the tool-workpiece and workpiece-heat sink is modeled using the following equation:

$$q = k_p(\theta_c - \theta_d) \tag{19}$$

where q is the heat flux per unit area flowing from the workpiece to the heat sink, k_p is the contact pressure-dependent contact conductance, θ_c and θ_d are the surface temperatures of the bodies in contact with each other. The value of k_p is set as linearly varying from 3000-4000 W/m^{2}K, based on Soundararajan et al. [113].

The commercial software Abaqus 6.14 is utilized to simulate the friction stir spot welding experiment. A user-defined subroutine is developed using FORTRAN to implement the recrystallization model kinetics. The CA method is implemented with state-dependent variables (SDV's) to allow for a simple one-to-one mapping of the microstructural variables in terms of the grain boundaries, misorientation and size on the FE mesh. The microstructure-based internal variables tracked by the cellular automata cells are stored in state-dependent variables (SDVs) at every integration point of the finite element mesh and updated with every time step. The material parameters for Al 6061-T6 are shown in Tables 4-1, 4-2 and 4-3.

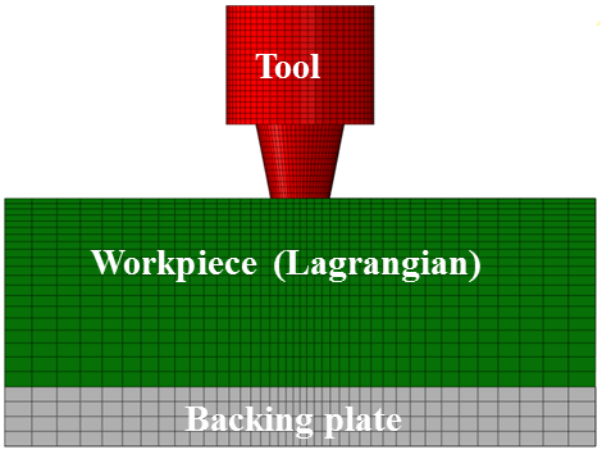

Figure 4-2: Mesh and Assembly of the developed FE model for FSSW of Al 6061-T6 plates.

Table 4-1: Material properties of Al 6061-T6 [19].

Material	**E (GPa)**	**ν**	**ρ (kg/m^3)**	**Tm (°C)**	**Thermal Expansion (10-6/°C)**	**Thermal Conductivity (W/mK)**	**Specific Heat (J/KgK)**
Al 6061-T6	68.9	0.33	2700	582	23.6	167	896

Table 4-2: Recrystallization parameters for Al 6061-T6 [124].

Material	**μ (MN/m^2)**	**Qact (KJ/mol)**	**M_0 (m4/Js)**	**Q_b (KJ/mol)**	**γ_0 (Jm^{-2})**
Al 6061-T6	2.6e4	156	1.78e8	147	0.324

Table 4-3: Dislocation-density model parameters of Al 6061-T6 [19].

Material	**α***	**β***	**ko**	**A(K)**	**B(K)**	$\dot{\gamma_o}$	**fo**	**fα**	**K**
Al 6061-T6	0.06	0.01	5.2-7.6	50000	14900	150	0.25	0.06	30

Material	**M**	$\widetilde{\gamma^r}$	ρ_{wo} **(mm-2)**	ρ_{co} **(mm-2)**	**b (mm)**	**α**
Al 6061-T6	3.06	3.2	1e7	1e8	2.86e-7	0.25

The FE model was validated by comparing the results predicted by the FE model with the experimental results for the 1500 rpm case. As shown in Figure 4-3, the axial forces showed good agreement with the experimental results. The estimated forces showed fluctuations that are a result of stick-slip phenomena. Also, a constant coefficient of friction is considered throughout the plunge in stage which has led to the discrepancy. A spot was chosen in the FE model as shown in Figure 4-4 to record the temperature

evolution results. This spot has the same size of the pyrometer measurement spot used in the experiment. The temperature results were then compared with the ones recorded by the pyrometer, and both the results showed a similar pattern as shown in Figure 4-5. The temperature predicted by the FE model is slightly higher than that of the measured values since heat loss due to convection is neglected in the FE model. It must be noted that temperatures below 200°C could not be recorded experimentally since the pyrometer can record values only higher than 200°C. The deformation predicted by the FE model exhibited a same pattern as the experimental result as shown in Figure 4-6.

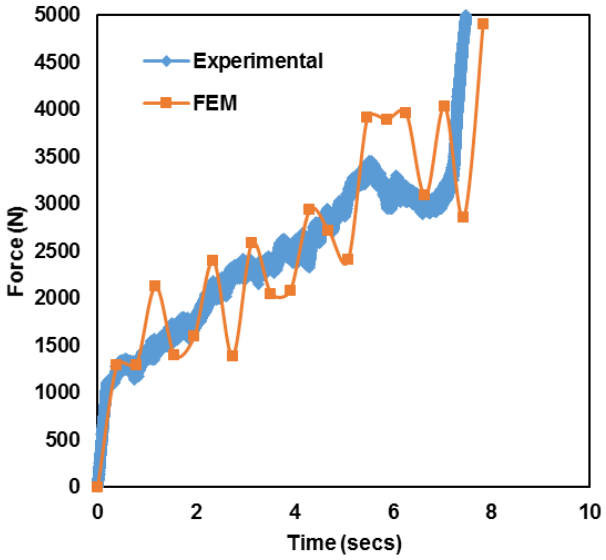

Figure 4-3: Axial forces (Experimental and results predicted by the FE model) for the 1500 rpm case.

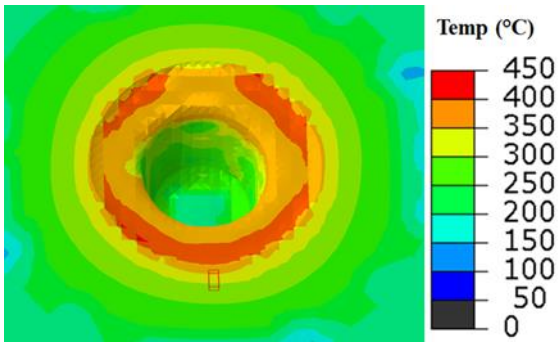

Figure 4-4: Spot chosen in the FE model in front of tool to record temperature for the 1500 rpm case.

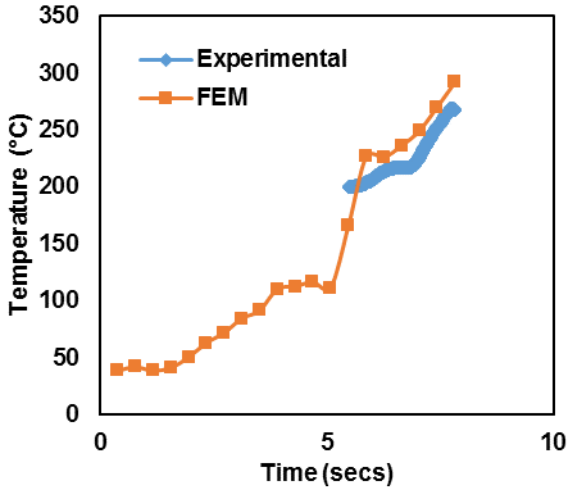

Figure 4-5: Temperature evolution (Experimental and results predicted by the FE model) for the 1500 rpm case.

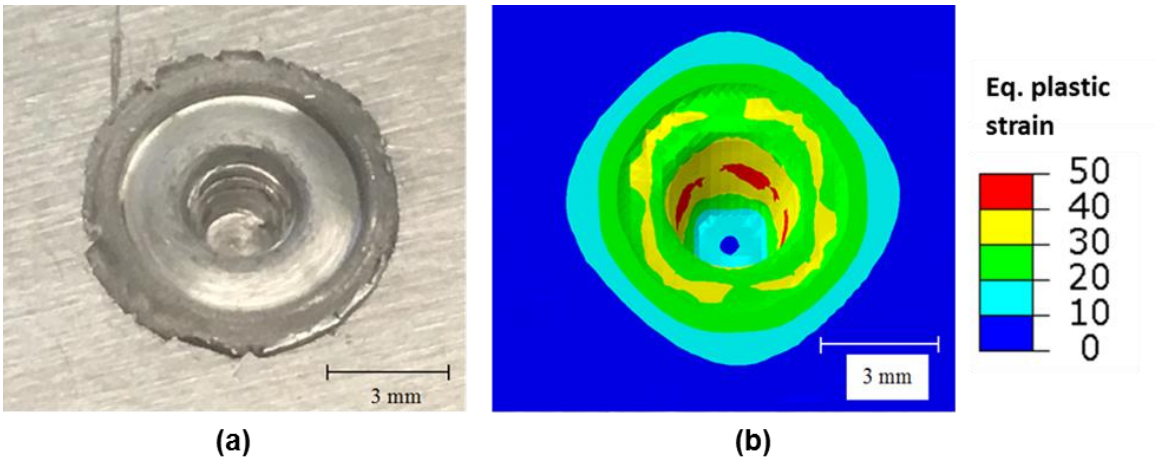

Figure 4-6: (a) Deformed region predicted by the FE model post plunge in process using the equivalent plastic strain distribution results.(b) Experimental sample after the plunge in process for the 1500 rpm case.

4.2.2 Microstructure evolution results

The initial microstructure of the Al 6061-T6 samples were characterized to obtain the grain structure and initial average grain size of 35 μm as shown in Figure 4-7. After the friction stir spot welding, the samples were sectioned across the stir zone and etched to obtain the grain structure. It was found that the original microstructure was completely replaced by a recrystallized structure in the stir zone with a final average grain size of 2.7 μm for the tool rotational speed of 1500 rpm and a final average grain size of 3.6 μm for the tool rotational speed of 2500 rpm in the stir zone. It is observed that grain refinement was the predominant phenomenon for the 1500 rpm case resulting in a fine equiaxed grain structure as shown in Figure 4-8(a). This is attributed to the lower observed process temperatures (Figure 4-5) and high forces (Figure 4-3). However, for the higher tool rotational speed (2500 rpm) case, the observed temperature was 100 ºC higher than the 1500 rpm case with lower corresponding forces. It allowed for the activation of the discontinuous dynamic recrystallization phenomenon, characterized by a hybrid

microstructure of fine and elongated grains due to the corresponding grain growth process as shown in Figure 4-8(b).

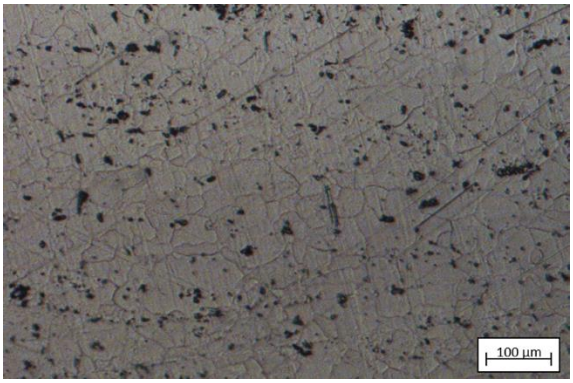

Figure 4-7: Initial microstructure of the base metal Al 6061-T6 alloy with an average grain size of 35 µm.

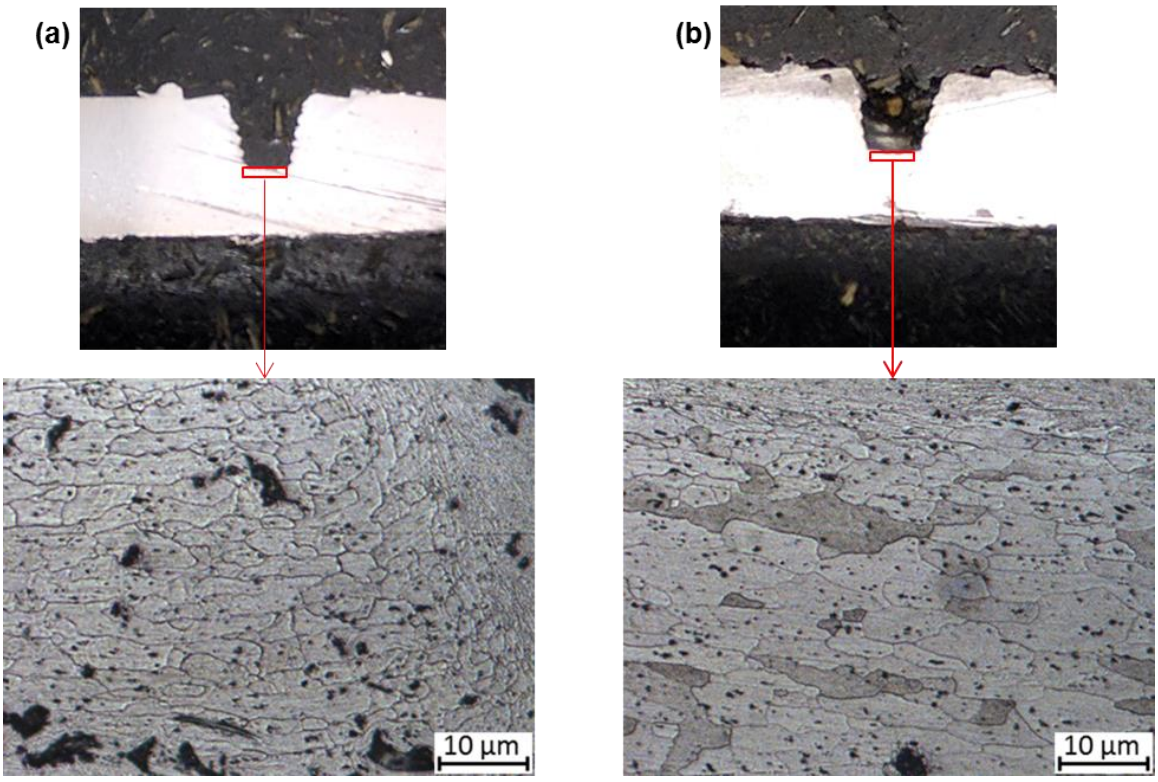

Figure 4-8: Microstructure characterization of the stir zone with a final average grain size of (a) 2.7 µm for a rotational speed of 1500 rpm and (b) 3.5 µm for a rotational speed of 2500 rpm.

The observed microstructure evolution is simulated with the developed FE-CA based dynamic recrystallization model. The initial 3D microstructure with an average grain size of 35 μm is reconstructed using the commercial software Dream 3D [106] and mapped onto the finite element mesh as shown in Figure 4-9. The grains are represented by the Euler angle formulation based on a random distribution. This orientation variable (SDV_PHI) is solely utilized to track the grain size and grain boundary evolution in the deforming matrix.

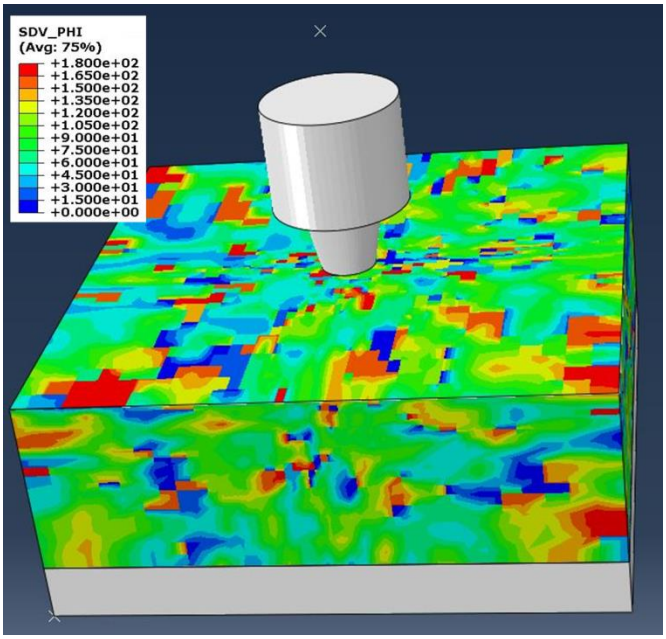

Figure 4-9: Coupled FE-CA mesh of the Al 6061-T6 workpiece with an initial average grain size of 35 μm undergoing FSSW. SDV_PHI corresponds to the orientation of the grain in terms of its Euler angle, Φ.

The recrystallization model predicts a final average grain size of 1.3 μm for the 1500 rpm case and a final average grain size of 1.8 μm for the 2500 rpm case in comparison to the observed experimental results of 2.7 μm and 3.6 μm (Figure 4-8) in the stir zone respectively. Grain size measurements are taken at varying depths of the weld

profile as well as on either side of the welding line as shown in Figure 4-10. The observed grain sizes are compared with the model predictions is shown in Figure 4-11. For the 1500 rpm case, the predicted temperatures (highest at ~300 ºC) resulted primarily in the activation of the grain refinement phenomenon resulting in a fine-grained recrystallized microstructure. Furthermore, for the 2500 rpm case, the predicted elevated temperatures result in the activation of the discontinuous dynamic recrystallization phenomenon resulting in a predicted larger final grain size and elongated grains due to the corresponding grain growth process.

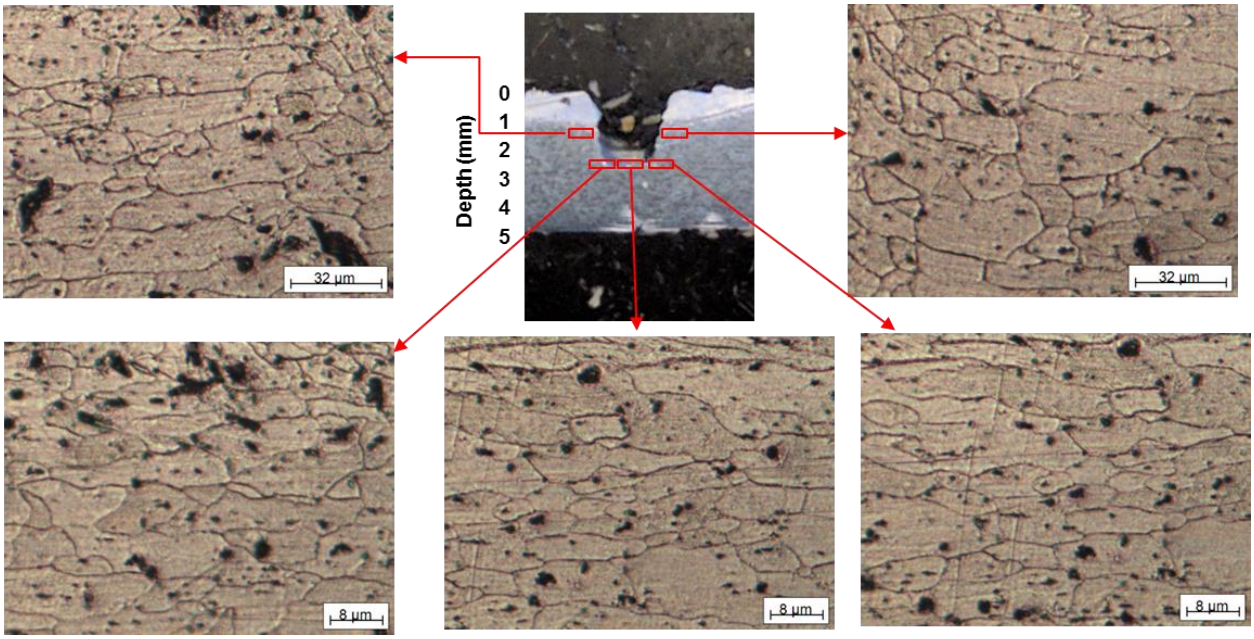

Figure 4-10: Optical micrographs for the grain size characterization of the friction stir weld for the 2500 rpm case.

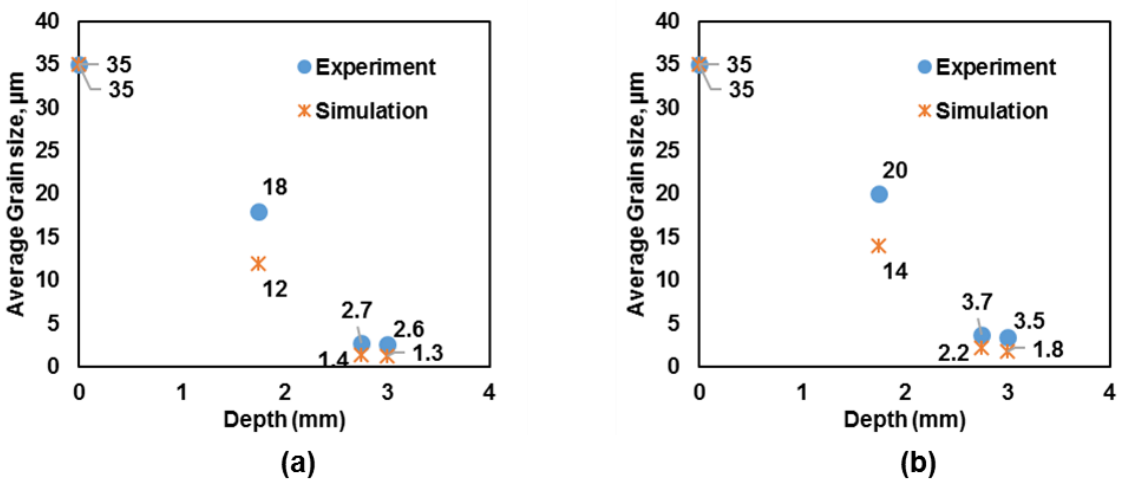

Figure 4-11: Comparison of experimental and predicted average grain sizes of the stir zone for the (a) 1500 rpm rotational speed and (b) 2500 rpm rotational speed.

The recrystallization kinetics of the model predicted a more refined grain structure compared to the experimental observations. This is attributed to the dislocation density evolution predictions. The dynamic nature of the deformation characterized by high strain rate and temperature process conditions results in an over prediction of the sub-grain misorientation and total dislocation density parameters. The temperatures and strains predicted by the model have been validated with experimental measurements at the surface of the weld (Figure 4-5). However, the temperature and strain predictions in the stir zone might have been over predicted, thereby affecting the grain size predictions. The model also does not account for a threaded tool utilized for the experiments, which is likely to affect the temperature and strain predictions in the weld zone. These discrepancies are considered acceptable as the force predictions for the process are accurate. Nonetheless, it accurately captured the physics of the process in terms of the onset and extent of the grain refinement and discontinuous dynamic recrystallization mechanisms reflected in the profile shown in Figure 4-11. For the 1500 rpm case, the

observed recrystallized structure is a fine-grained equiaxed grain structure indicating the prevalence of the grain refinement mechanism. The model predicted the observed temperature and the onset of grain refinement with an extent upto 1.3 μm compared to the observed 2.7 μm. For the 2500 rpm case, the higher observed process temperatures resulted in a hybrid microstructure of fine and equiaxed grains due to the grain growth process activated at these temperatures. The model predicted a rise in temperature by 100 ˚C at the surface and the onset of discontinuous dynamic recrystallization and the growth process, thus resulting in a larger average grain size at this condition. From the experiments and modeling efforts, it is observed that with increasing temperatures and decreasing forces, the extent of the discontinuous dynamic recrystallization phenomenon increases, resulting in the formation of larger grains developed by the migration of grain boundaries at elevated temperatures. For both the mechanisms, a fine-grained recrystallized microstructure completely replaced the original microstructure.

5. CONCLUSIONS AND RECOMMENDATIONS

5.1 Conclusions

In this work, a novel multi-scale numerical framework capable of predicting the dynamic grain size evolution under varying conditions of strain rate, temperature and initial microstructure for pure copper. The unique implementation of the dislocation density constitutive model along with the critical dislocation density parameter allowed for the prediction of the onset of both grain refinement and discontinuous dynamic recrystallization phenomena for quasi-static and dynamic deformation processes ranging from low to high temperature conditions. Additionally, integration of the probabilistic cellular automata framework along with the recrystallization kinetics accurately captured the physics of the grain refinement and discontinuous dynamic recrystallization phenomena throughout the deformation processes.

During the multi-pass compression of copper at room temperature, the simulations predicted the microstructure of the copper samples with an initial average grain size of 60 μm refined down to the uniform fine grained microstructure of size 0.2 μm. The modeling captured the grain boundary distortion due to recrystallization during each compression pass, which showed good agreement with experimental TEM measurements. Hot compression experiments simulated to evaluate the grain nucleation and growth kinetics with an initial grain size of 78 μm for varying deformation temperatures predicted average grain sizes of 9.8 μm, 14 μm, 34 μm, 57 μm and 90 μm at 725K, 775K, 875K, 975K and 1075K respectively, which were in good agreement with the experimental results. High strain rate experiments conducted with a Kolsky bar were also simulated. Copper samples of initial grain sizes 30 μm, 55 μm and 174 μm when

subjected to tensile tests at strain rate of 2700 s^{-1} showed the grain refinement down to 7.2 µm, 5.7 µm and 4.3µm respectively. Furthermore, simulations on grain coarsening of the fractured samples upon heat treatment revealed grain coarsening is independent of the initial microstructure and primarily dependent on the temperature conditions. The physics-based nature of the model allowed for grain evolution over a wide range of deformation conditions.

The study shows the integration of the Kolsky bar with the synchrotron X-rays allows for the *in situ* detection of the temporal evolution of the grain size refinement mechanism developed during the high strain rate loading of pure copper. Copper samples are dynamically loaded at a constant strain rate of $1200s^{-1}$ with the Kolsky bar. The microstructural characterization tests conducted on the samples before loading and upon fracture of the samples show that the initial coarse grains in the sample with an average grain size of 36 µm refine down to a uniform microstructure of final average grain size 6.3 µm. This novel experimental technique allows for the correlation of the recorded flow stress behavior with the recorded the ultra-fast X-ray diffraction patterns to identify the initiation as well as temporal evolution rate of the grain refinement phenomenon. It is found that the initiation of the mechanism occurs beyond a critical strain of 0.011 where the initial fine grains are formed on the pre-existing grain boundaries. This is followed by a constant rate of grain size refinement on further loading resulting in a uniform fine grained microstructure upon fracture. The experiment validated the kinetics of the developed dynamic recrystallization model and accurately predicted the initiation at a strain of 0.04 followed by a continuous rate of refinement to give a predicted final

average grain size of 2.4 μm. This method of microstructure evolution and tracking provides an insight into the dynamic response of the material at multiple scales.

Finally, the study implemented the model to predict the *in situ* grain size evolution and extent of dynamic recrystallization during the friction stir spot welding process. Al 6061-T6 plates with an initial grain size of 35 μm undergoing FSSW with varying tool rotational speeds of 1500 rpm and 2500 rpm resulted in a fine-grained recrystallized structure of size 2.7 μm and 3.6 μm respectively. The model predicted the recrystallized grain size and morphology evolution of the FSSW process for these process parameters. It is found that elevated process temperatures are characterized by the migration of grain boundaries resulting in a mixed microstructure of both fine and elongated grains due to dynamic recrystallization phenomenon. This model will allow for the design of process parameters with respect to desired final microstructure as well as prediction of auxiliary parameters like microhardness and strength.

5.2 Recommendations

Some ideas for future research on the modeling and experimental aspects are summarized as follows:

- The material model can be extended to account for metal alloys undergoing phase change and incorporate the microstructure evolution parameters for the different phases.
- The numerical model can be extended to predict grain size dependent material properties such as microhardness and strength.

- The model can be extended to identify the relationship between the process parameters and predicted microstructure evolution, allowing for an optimized design of the machining process.

LIST OF REFERENCES

[1] Aronson, R. B. (2003). The new world of micromanufacturing. Manufacturing Engineering, 130(4), 81-81.

[2] Halley, J. E., Helvey, A. M., Winfough, K. S. W. (1999). The impact of high-speed machining technology on the design and fabrication of aerospace components. In Proceedings of the ASME.

[3] Komanduri, R., Chandrasekaran, N., Raff, L. M. (1998). Effect of tool geometry in nanometric cutting: a molecular dynamics simulation approach. Wear, 219(1), 84-97.

[4] Kim, K. W., Lee, W. Y., Sin, H. C. (1999). A finite element analysis for the characteristics of temperature and stress in micro-machining considering the size effect. International Journal of Machine Tools and Manufacture, 39(9), 1507-1524.

[5] Kalidindi, S. R. (2013), Microstructure informatics. Informatics for materials science and engineering: data-driven discovery for accelerated experimentation and application. 443-466.

[6] Sakai, T., Belyakov, A., Kaibyshev, R., Miura, H., Jonas, J. J. (2014). Dynamic and post-dynamic recrystallization under hot, cold and severe plastic deformation conditions. Progress in Materials Science, 60, 130-207.

[7] Burke, J. E., Turnbull, D. (1952). Recrystallization and grain growth. Progress in Metal Physics, 3, 220-292.

[8] Humphreys, F. J., Hatherly, M. (2012). Recrystallization and related annealing phenomena. Elsevier.

[9] Doherty, R. D., Hughes, D. A., Humphreys, F. J., Jonas, J. J., Juul Jensen, D., Kassner, M. E., King, W. E., McNelley, T. R., McQueen, H. J., Rollett, A. D. (1997). Current issues in recrystallization: a review. Materials Science and Engineering: A, 238(2), 219-274.

[10] Toth, L. S., Gu, C. (2014). Ultrafine-grain metals by severe plastic deformation. Materials Characterization, 92, 1-14.

[11] Stolyarov, V. V., Zhu, Y. T., Alexandrov, I. V., Lowe, T. C., Valiev, R. Z. (2003). Grain refinement and properties of pure Ti processed by warm ECAP and cold rolling. Materials Science and Engineering: A, 343(1), 43-50.

[12] Azushima, A., Kopp, R., Korhonen, A., Yang, D. Y., Micari, F., Lahoti, G. D., Groche, P., Yanagimoto, J., Tsuji, N., Rosochowski, A., Yanagida, A. (2008). Severe plastic deformation (SPD) processes for metals. CIRP Annals-Manufacturing Technology, 57(2), 716-735.

[13] King, W.E., Campbell, G.H., Frank, A., Reed, B., Schmerge, J.F., Siwick, B.J., Stuart, B.C., Weber, P.M. (2005). Ultrafast electron microscopy in materials science, biology, and chemistry. Journal of Applied Physics, 97(11), 8.

[14] Adams, B. L., Wright, S. I., Kunze, K. (1993). Orientation imaging: the emergence of a new microscopy. Metallurgical Transactions A, 24(4), 819-831.

[15] Wright, S. I., Nowell, M. M., de Kloe, R., Camus, P., Rampton, T. (2015). Electron imaging with an EBSD detector. Ultramicroscopy, 148, 132-145.

[16] Xie, H. R., Lin, D. L., Chai, Y. T., Hu, J. (2015). EBSD investigation on the evolution of microstructure and grain boundaries in coarse-grained Ni–48Al upon large deformation at elevated temperature. Intermetallics, 58, 98-102.

[17] Komanduri, R. Chandrasekaran, N., Raff, L. M. (1998). Effect of tool geometry in nanometric cutting: a molecular dynamics simulation approach. Wear, 219(1), 84-97.

[18] Shi, B., Attia, H. (2010). Current status and future direction in the numerical modeling and simulation of machining processes: a critical literature review. Machining Science and Technology, 14(2), 149-188.

[19] Ding, H., Shen, N., Shin, Y. C. (2011). Modeling of grain refinement in aluminum and copper subjected to cutting. Computational Materials Science, 50(10), 3016-3025.

[20] Ding, H., Shen, N., Shin, Y. C. (2012). Predictive modeling of grain refinement during multi-pass cold rolling. Journal of Materials Processing Technology, 212(5), 1003-1013.

[21] Ding, H., Shin, Y. C. (2012). Dislocation density-based modeling of subsurface grain refinement with laser-induced shock compression. Computational Materials Science, 53(1), 79-88.

[22] Johnson, G. R., Cook, W. H. (1983). A constitutive model and data for metals subjected to large strains, high strain rates and high temperatures. In Proceedings of the 7th International Symposium on Ballistics.

[23] Zerilli, F. J., Armstrong, R. W. (1987). Dislocation-mechanics-based constitutive relations for material dynamics calculations. Journal of Applied Physics, 61(5), 1816-1825.

[24] Mecking, H., Kocks, U. F. (1981). Kinetics of flow and strain-hardening. Acta Metallurgica, 29(11), 1865-1875.

[25] Dixit, U. S., Joshi, S. N., Davim, J. P. (2011). Incorporation of material behavior in modeling of metal forming and machining processes: A review. Materials & Design, 32(7), 3655-3670.

[26] Taylor, G. I. (1938). Plastic strain in metals. Journal of Institute of Metals, 62, 307-324.

[27] Bishop, J. F. W., Hill, R. (1951). A theory of the plastic distortion of a polycrystalline aggregate under combined stresses. Philosophical Magazine, 42, 414-427.

[28] Bishop, J. F. W., Hill, R. A theoretical derivation of the plastic properties of a polycrystalline face centered metal. (1951). Philosophical Magazine, 42, 1298-1307.

[29] Kroner, E. (1961). On the plastic deformation of polycrystals. Acta Metallurgica, 9(2), 155-161.

[30] Asaro, R. J., Needleman, A. (1985). Overview no. 42 Texture development and strain hardening in rate dependent polycrystals. Acta metallurgica, 33(6), 923-953.

[31] Sarma, G. B., Dawson, P. R. (1996). Texture predictions using a polycrystal plasticity model incorporating neighbor interactions. International Journal of Plasticity, 12(8), 1023-1054.

[32] Zhao, Z. S., Mao, W. M., Roters, F., Raabe, D. (2004). A texture optimization study for minimum earing in aluminium by use of a texture component crystal plasticity finite element method. Acta Materialia, 52(4), 1003-1012.

[33] Zaafarani, N., Raabe, D., Singh, R. N., Roters, F., Zaefferer, S. (2006). Three-dimensional investigation of the texture and microstructure below a nanoindent in a Cu single crystal using 3D EBSD and crystal plasticity finite element simulations. Acta Materialia, 54(7), 1863-1876.

[34] Weber, F., Schestakow, I., Roters, F., Raabe, D. (2008). Texture evolution during bending of a single crystal copper nanowire studied by EBSD and crystal plasticity finite element simulations. Advanced Engineering Materials, 10(8), 737-741.

[35] Zhao, Z. S., Mao, W. M., Roters, F., Raabe, D. (2004). A texture optimization study for minimum earing in aluminium by use of a texture component crystal plasticity finite element method. Acta Materialia, 52(4), 1003-1012.

[36] Okumura, D., Higashi, Y., Sumida, K., Ohno, N. (2007). A homogenization theory of strain gradient single crystal plasticity and its finite element discretization. International Journal of Plasticity, 23(7), 1148-1166.

[37] Nes, E. (1997). Modelling of work hardening and stress saturation in FCC metals. Progress in Materials Science, 41(3), 129-193.

[38] Estrin, Y., Toth, L. S., Molinari, A., Bréchet, Y. (1998). A dislocation-based model for all hardening stages in large strain deformation. Acta Materialia, 46(15), 5509-5522.

[39] Estrin, Y. (1998). Dislocation theory based constitutive modelling: foundations and applications. Journal of Materials Processing Technology, 80, 33-39.

[40] Pantleon, W. (2004). Stage IV work-hardening related to disorientations in dislocation structures. Materials Science and Engineering: A, 387, 257-261.

[41] Enikeev, N. A., Kim, H. S., Alexandrov, I. V. (2007). Kinetic dislocation model of microstructure evolution during severe plastic deformation. Materials Science and Engineering: A, 460, 619-623.

[42] Grong, Ø., Shercliff, H. R. (2002). Microstructural modelling in metals processing. Progress in Materials Science, 47(2), 163-282.

[43] Nes, E., Marthinsen, K. (2002). Modeling the evolution in microstructure and properties during plastic deformation of fcc-metals and alloys–an approach towards a unified model. Materials Science and Engineering: A, 322(1), 176-193.

[44] Ma, A., Roters, F., Raabe, D. (2006). A dislocation density based constitutive model for crystal plasticity FEM including geometrically necessary dislocations. Acta Materialia, 54(8), 2169-2179.

[45] Ma, A., Roters, F., Raabe, D. (2006). On the consideration of interactions between dislocations and grain boundaries in crystal plasticity finite element modeling–theory, experiments, and simulations. Acta Materialia, 54(8), 2181-2194.

[46] Ma, A., Roters, F., Raabe, D. (2006). Studying the effect of grain boundaries in dislocation density based crystal-plasticity finite element simulations. International Journal of Solids and Structures, 43(24), 7287-7303.

[47] Aoyagi, Y., Kobayashi, R., Kaji, Y., Shizawa, K. (2013). Modeling and simulation on ultrafine-graining based on multiscale crystal plasticity considering dislocation patterning. International Journal of Plasticity, 47, 13-28.

[48] Svoboda, A., Wedberg, D., Lindgren, L. E. (2010). Simulation of metal cutting using a physically based plasticity model. Modelling and Simulation in Materials Science and Engineering, 18(7), 075005.

[49] Lindgren, L. E., Domkin, K., Hansson, S. (2008). Dislocations, vacancies and solute diffusion in physical based plasticity model for AISI 316L. Mechanics of Materials, 40(11), 907-919.

[50] Sun, Z. C., Yang, H., Han, G. J., Fan, X. G. (2010). A numerical model based on internal-state-variable method for the microstructure evolution during hot-working process of TA15 titanium alloy. Materials Science and Engineering: A, 527(15), 3464-3471

[51] Sundararaghavan, V., Kumar, A. (2012). Probabilistic modeling of microstructure evolution using finite element representation of statistical correlation functions. International Journal of Plasticity, 30, 62-80.

[52] Sun, S., Sundararaghavan, V. (2012). A probabilistic crystal plasticity model for modeling grain shape effects based on slip geometry. Acta Materialia, 60(13), 5233-5244.

[53] Askari, H., Maughan, M. R., Abdolrahim, N., Sagapuram, D., Bahr, D. F., Zbib, H. M. (2015). A stochastic crystal plasticity framework for deformation of micro-scale polycrystalline materials. International Journal of Plasticity, 68, 21-33.

[54] Estrin, Y., Vinogradov, A. (2013). Extreme grain refinement by severe plastic deformation: a wealth of challenging science. Acta Materialia, 61(3), 782-817.

[55] Wilson, P. W. (2013). Recent developments in the study of recrystallization. E-Publishing, InTech., 102-104.

[56] Bay, B., Hansen, N., Hughes, D.A., Kuhlmann-Wilsdorf, D. (1992). Evolution of f.c.c. deformation structures in polyslip. Acta Metallurgica et Materialia, 40, 205-219.

[57] Kuhlmann-Wilsdorf, D., Hansen, N. (1991). Geometrically necessary, incidental and subgrain boundaries. Scripta Metallurgica et Materialia, 25(7), 1557-1562.

[58] Liu, Q., Jensen, D. J., Hansen, N. (1998). Effect of grain orientation on deformation structure in cold-rolled polycrystalline aluminium. Acta Materialia, 46(16), 5819-5838.

[59] Belyakov, A., Kaibyshev, R. (1995). Structural changes of ferritic stainless steel during severe plastic deformation. Nanostructured Materials, 6(5-8), 893-896.

[60] Les, P., Zehetbauer, M. J. (1994). Evolution of microstructural parameters in large strain deformation: Description by Zehetbauer's model. In Key Engineering Materials, 97, 335-340.

[61] Tóth, L. S., Molinari, A., Estrin, Y. (2002). Strain hardening at large strains as predicted by dislocation based polycrystal plasticity model. Journal of Engineering Materials and Technology, 124(1), 71-77.

[62] Tóth, L. S., Estrin, Y., Lapovok, R., Gu, C. (2010). A model of grain fragmentation based on lattice curvature. Acta Materialia, 58(5), 1782-1794.

[63] Valiev, R. Z., Langdon, T. G. (2010). The art and science of tailoring materials by nanostructuring for advanced properties using SPD techniques. Advanced Engineering Materials, 12(8), 677-691.

[64] Valiev, R. Z., Islamgaliev, R. K., Alexandrov, I. V. (2000). Bulk nanostructured materials from severe plastic deformation. Progress in Materials Science, 45(2), 103-189.

[65] Zhilyaev, A. P., Langdon, T. G. (2008). Using high-pressure torsion for metal processing: Fundamentals and applications. Progress in Materials Science, 53(6), 893-979.

[66] Valiev, R. Z., Ivanisenko, Y. V., Rauch, E. F., Baudelet, B. (1996). Structure and deformaton behaviour of Armco iron subjected to severe plastic deformation. Acta Materialia, 44(12), 4705-4712.

[67] Baik, S. C., Estrin, Y., Kim, H. S., Jeong, H. T., Hellmig, R. J. (2002). Calculation of deformation behavior and texture evolution during equal channel angular pressing of IF steel using dislocation based modeling of strain hardening. Materials Science Forum, 408, 697-702.

[68] Baik, S. C., Estrin, Y., Kim, H. S., Hellmig, R. J. (2003). Dislocation density-based modeling of deformation behavior of aluminium under equal channel angular pressing. Materials Science and Engineering: A, 351(1), 86-97.

[69] Lemiale, V., Estrin, Y., Kim, H. S., O'Donnell, R. (2010). Grain refinement under high strain rate impact: A numerical approach. Computational Materials Science, 48(1), 124-132.

[70] Hardwick, D., Tegart, W. M. (1961). Structural changes during the deformation of copper, aluminium and nickel at high temperatures and high strain rates. Journal of Institute of Metals, 90, 17-21.

[71] Sakai, T., Jonas, J. J. (1984). Overview no. 35 dynamic recrystallization: mechanical and microstructural considerations. Acta Metallurgica, 32(2), 189-209.

[72] Sakai, T. (1995). Dynamic recrystallization microstructures under hot working conditions. Journal of Materials Processing Technology, 53(1-2), 349-361.

[73] Sandström, R., Lagneborg, R. (1975). A model for hot working occurring by recrystallization. Acta Metallurgica, 23(3), 387-398.

[74] Roberts, W., Ahlblom, B. (1978). A nucleation criterion for dynamic recrystallization during hot working. Acta Metallurgica, 26(5), 801-813.

[75] Miura, H., Aoyama, H., Sakai, T. (1994). Effect of Grain-Boundary Misorientation on Dynamic Recrystallization of Cu--Si Bicrystals. Journal of the Japan Institute of Metals(Japan), 58(3), 267-275.

[76] Wusatowska-Sarnek, A. M., Miura, H., Sakai, T. (2002). Nucleation and microtexture development under dynamic recrystallization of copper. Materials Science and Engineering: A, 323(1), 177-186.

[77] Belyakov, A., Miura, H., Sakai, T. (1998). Dynamic recrystallization under warm deformation of a 304 type austenitic stainless steel. Materials Science and Engineering: A, 255(1), 139-147.

[78] Wusatowska-Sarnek, A. M., Miura, H., Sakai, T. (2002). Nucleation and microtexture development under dynamic recrystallization of copper. Materials Science and Engineering: A, 323(1), 177-186.

[79] Rollett, A. D., Luton, M. J., Srolovitz, D. J. (1992). Microstructural simulation of dynamic recrystallization. Acta Metallurgica et Materialia, 40(1), 43-55.

[80] Peczak, P. (1995). A Monte Carlo study of influence of deformation temperature on dynamic recrystallization. Acta Metallurgica et Materialia, 43(3), 1279-1291.

[81] Ding, R., Guo, Z. X. (2001). Coupled quantitative simulation of microstructural evolution and plastic flow during dynamic recrystallization. Acta Materialia, 49(16), 3163-3175.

[82] Ding, R., & Guo, Z. X. (2004). Microstructural evolution of a Ti–6Al–4V alloy during β-phase processing: experimental and simulative investigations. Materials Science and Engineering: A, 365(1), 172-179.

[83] Chen, F., Cui, Z., Liu, J., Chen, W., Chen, S. (2010). Mesoscale simulation of the high-temperature austenitizing and dynamic recrystallization by coupling a cellular automaton with a topology deformation technique. Materials Science and Engineering: A, 527(21), 5539-5549.

[84] Zhao, J. W., Ding, H., Zhao, W. J., Cao, F. R., Hou, H. L., Li, Z. Q. (2008). Modeling of dynamic recrystallization of Ti6Al4V alloy using a cellular automaton approach. Acta Metallurgica, 21(4), 260-268.

[85] Wu, C., Yang, H., Li, H. W. (2013). Modeling of discontinuous dynamic recrystallization of a near-a titanium alloy IMI834 during isothermal hot compression by combining a cellular automaton model with a crystal plasticity finite element method. Computational Materials Science, 79, 944-959.

[86] Zhang, Y., Jiang, S., Liang, Y., Hu, L. (2013). Simulation of dynamic recrystallization of NiTi shape memory alloy during hot compression deformation based on cellular automaton. Computational Materials Science, 71, 124-134.

[87] Hallberg, H., Wallin, M., Ristinmaa, M. (2010). Simulation of discontinuous dynamic recrystallization in pure Cu using a probabilistic cellular automaton. Computational Materials Science, 49(1), 25-34.

[88] Hallberg, H., Svendsen, B., Kayser, T., Ristinmaa, M. (2014). Microstructure evolution during dynamic discontinuous recrystallization in particle-containing Cu. Computational Materials Science, 84, 327-338.

[89] Popova, E., Staraselski, Y., Brahme, A., Mishra, R. K., Inal, K. (2015). Coupled crystal plasticity–probabilistic cellular automata approach to model dynamic recrystallization in magnesium alloys. International Journal of Plasticity, 66, 85-102.

[90] Zhilyaev, A. P., Langdon, T. G. (2008). Using high-pressure torsion for metal processing: Fundamentals and applications. Progress in Materials Science, 53(6), 893-979.

[91] Tsuji, N., Saito, Y., Lee, S. H., Minamino, Y. (2003). ARB (accumulative roll-bonding) and other new techniques to produce bulk ultrafine grained materials. Advanced Engineering Materials, 5(5), 338-344.

[92] Chen W. W., Song, B. (2010). Split Hopkinson (Kolsky) bar: design, testing and applications. Springer Science & Business Media, Berlin, Germany.

[93] Chen, W. W., Hudspeth, M. C., Claus, B., Parab, N. D., Black, J. T., Fezzaa, K., Luo, S. N. (2014). In situ damage assessment using synchrotron X-rays in materials loaded by a Hopkinson bar. Philosophical Transactions of the Royal Society of London A, 372(2015), 20130191.

[94] Hudspeth, M., Sun, T., Parab, N., Guo, Z., Fezzaa, K., Luo, S., Chen, W. (2015). Simultaneous X-ray diffraction and phase-contrast imaging for investigating material deformation mechanisms during high-rate loading. Journal of Synchrotron Radiation, 22(1), 49-58.

[95] Thomas, W. M., Nicholas, E. D., NeedHam, J. C., Murch, M. G., Templesmith, P., Dawes, C. J. (1991). Friction stir welding. International Patent Appli. No. PCT/GB92102203 and GB Patent Appli. No. 9125978.8. December US Patent, (5460), 317.

[96] Gerlich, A., Avramovic-Cingara, G., North, T. H. (2006). Stir zone microstructure and strain rate during Al 7075-T6 friction stir spot welding. Metallurgical and Materials Transactions A, 37(9), 2773-2786.

[97] Gerlich, A., Yamamoto, M., North, T. H. (2007). Strain rates and grain growth in Al 5754 and Al 6061 friction stir spot welds. Metallurgical and Materials Transactions A, 38(6), 1291-1302.

[98] Sato, Y. S., Urata, M., Kokawa, H. (2002). Parameters controlling microstructure and hardness during friction-stir welding of precipitation-hardenable aluminum alloy 6063. Metallurgical and Materials Transactions A, 33(3), 625-635.

[99] Chang, C. I., Lee, C. J., Huang, J. C. (2004). Relationship between grain size and Zener–Holloman parameter during friction stir processing in AZ31 Mg alloys. Scripta Materialia, 51(6), 509-514.

[100] Belyakov, A., Sakai, T., Miura, H., Tsuzaki, K. (2001). Grain refinement in copper under large strain deformation. Philosophical Magazine A, 81(11), 2629-2643.

[101] Peczak, P., Luton, M. J. (1993). The effect of nucleation models on dynamic recrystallization I. Homogeneous stored energy distribution. Philosophical Magazine B, 68(1), 115-144.

[102] Zener, C., Hollomon, J. H. (1944). Effect of strain rate upon plastic flow of steel. Journal of Applied Physics, 15(1), 22-32.

[103] Read, W. T., Shockley, W. (1950). Dislocation models of crystal grain boundaries. Physical Review, 78(3), 275.

[104] Raabe, D. (2002). Cellular automata in materials science with particular reference to recrystallization simulation. Annual Review of Materials Research, 32(1), 53-76.

[105] ASM Handbook Program Corporate Author. (1990). ASM Handbook, Volume 1: Properties and Selection: Irons, Steels, and High-Performance Alloys. Vol. 1.

[106] Groeber, M. A., Jackson, M. A. (2014). DREAM. 3D: a digital representation environment for the analysis of microstructure in 3D. Integrating Materials and Manufacturing Innovation, 3(1), 5.

[107] Blaz, L., Sakai, T., Jonas, J. J. (1983). Effect of initial grain size on dynamic recrystallization of copper. Metal Science, 17(12), 609-616.

[108] Sun, T., Fezzaa, K. (2016). HiSPoD: a program for high-speed polychromatic X-ray diffraction experiments and data analysis on polycrystalline samples. Journal of Synchrotron Radiation, 23(4), 1046-1053.

[109] Williamson, G. K., Hall, W. H. (1953). X-ray line broadening from filed aluminium and wolfram. Acta Metallurgica, 1(1), 22-31.

[110] Davis, T. A., Shin, Y. C., Yao, B. (2011). Observer-based adaptive robust control of friction stir welding axial force. IEEE/ASME Transactions on Mechatronics, 16(6), 1032-1039.

[111] Veljić, D., Međo, B., Rakin, M., Radosavljević, Z., Bajić, N. (2016). Analysis of the tool plunge in friction stir welding-comparison of aluminium alloys 2024 T3 and 2024 T351. Thermal Science, 20(1), 247-254.

[112] Al-Badour, F., Merah, N., Shuaib, A., Bazoune, A. (2013). Coupled Eulerian Lagrangian finite element modeling of friction stir welding processes. Journal of Materials Processing Technology, 213(8), 1433-1439.

[113] Soundararajan, V., Zekovic, S., Kovacevic, R. (2005). Thermo-mechanical model with adaptive boundary conditions for friction stir welding of Al 6061. International Journal of Machine Tools and Manufacture, 45(14), 1577-1587.

[114] Huang, Y., Humphreys, F. J. (1999). Measurements of grain boundary mobility during recrystallization of a single-phase aluminium alloy. Acta Materialia, 47(7), 2259-2268.

VITA

Pooja Nitin Shah was born in Coimbatore, India. She graduated from Birla Institute of Technology and Science, Pilani – Dubai Campus with a Bachelor of Engineering (Hons) in Mechanical Engineering in 2014. She began her Master of Science in Mechanical Engineering at Purdue University in August 2014. Her research under the guidance of Dr. Yung C. Shin is in the field of computational mechanics and material testing.